In Vitro Simulation of Modular Neck Fracture, Wear, Corrosion, and Distraction in Total Hip Replacements

by

Fahad Aljenaei

A thesis submitted to the Faculty of Graduate and Postdoctoral studies in partial fulfillment of the requirements for the degree of

Master of Applied Science

in

Mechanical Engineering

Ottawa-Carleton Institute for Mechanical and Aerospace Engineering

Faculty of Engineering

University of Ottawa

Abstract

Total hip replacements are being used to relieve pain and restore the hip function of unhealthy hip joints. The various sizes and geometries of the modular femoral neck implants allow the surgeon to optimize the range of motion and patient's leg length. However, some *in vivo* modular femoral neck retrievals have shown early fatigue and advanced wear-corrosion at the neck-stem taper interface, which can lead to adverse tissue reactions and failure of the implant.

The overall objective of this study was to simulate *in vivo* fatigue fracture, wear, and corrosion of modular necks at the neck-stem taper interface in a laboratory setting (*in vitro*) to better predict the failure mechanisms and implant limitations. More specifically, after optimizing the laboratory setup and the testing conditions, this study aimed to compare the effects of the modular neck material (Ti6Al4V and CoCrMo) and the implant assembly technique (hand and impact assembly) on fatigue life, wear-corrosion resistance, and distraction force. The PROFEMUR® Modular Neck System with CoCrMo femoral heads and Ti6Al4V stems was used in this study. The *in vitro* simulation was divided into two types of tests: fatigue tests (high compression load for a short cyclic loading duration) and corrosion tests (low compression load for a long cyclic loading duration). The neck-stem interface was submersed in a phosphate buffered saline solution, which was maintained at a temperature of 80 ºC to accelerate the corrosion reaction.

The simulation results showed that the Ti6Al4V necks were more vulnerable to fatigue fracture than CoCrMo necks. In addition, impact assembly of the components resulted in an increased implant fatigue life compared to hand assembly, but also increased the distraction force. The observed wear-corrosion damage was higher in fatigue tests than corrosion tests,

suggesting that the level of mechanical load was a major factor influencing implant surface damage and fatigue fracture. On the other hand, corrosion tests showed that longer exposure resulted in more fluid accumulation in the stem pocket. This may lead to the formation of a corrosion cell with strongly acidic conditions in the stem pocket, as well as the potential for larger metal ion release. Overall, the *in vitro* simulation was successful in reproducing femoral modular neck fracture and wear-corrosion damage similar to retrieved *in vivo* specimens. Results may play a major role in the future development of total hip replacements and international standards for implant testing.

Acknowledgments

I would like to express my gratitude to my supervisors Dr. Michel Nganbe and Dr. Isabelle Catelas for the opportunity they have given me to work on this research, for the knowledge they have shared with me, and for all the guidance they have provided throughout this work.

Very special thanks to Mr. Hakim Louati, Research Engineer at the Orthopaedics Biomechanics Laboratory (Division of Orthopaedic Surgery), for his assistance, generous contribution, and support from the beginning until the end of this work.

I want to express my thanks to Dr. Eric Lehoux, and my colleagues at the Orthopaedic Bioengineering Laboratory (Dr. Catelas' lab) for their assistance. I want to extend my thanks to the staff of the machine shop at the University of Ottawa for their help with designing and machining the experiment fixtures.

I would like to thank Dr. Paul Beaulé, Chair of the Division of Orthopaedic Surgery at The Ottawa Hospital, for his contribution in this research. I would also like to thank Microport Orthopedics Inc. for providing the research specimens and for their financial support, as well as Mitacs Canada for their financial contribution in this research.

Finally, my deepest thanks and appreciation to my beloved parents, family, and friends for their encouragements and all the support they have provided.

Contents

List of Figures

List of Tables

List of Acronyms

α	Offset angle of tested implants
β	Offset angle of tested implants
θ	Inclination angle of the femoral neck
Al_2O_3	Alumina
CoCrMo	Cobalt chromium molybdenum
CT	Distance from the centre of the femoral head to the distal tip of the stem
D_a	Embedding depth of the femoral stem
HXLPE	Highly cross-linked polyethylene
kN	Kilo Newton
LDPE	Low-density polyethylene
PBS	Phosphate buffered saline
PMMA	Polymethylmethacrylate
PTFE	polytetrafluoroethylene
PVDF	Polyvinylidene fluoride
THR	Total hip replacement
Ti6Al4V	Titanium aluminum vanadium
UHMWPE	Ultrahigh molecular weight polyethylene
ZTA	Zirconia toughened-alumina

1 Introduction and Objectives

1.1 Introduction

The hip joint carries the body weight and counters the ground forces of our daily physical activities, thus, the hip sustains a great amount of load bearings through a wide range of motion. However, medical conditions such as arthritis can limit its functionality, resulting in pain and joint stiffness. Therefore, the hip replacement surgical treatment, which is considered to be one of the most successful orthopedic procedures [1], has proved to be highly effective at restoring the hip function while eliminating pain. With a growing world population, hip-related diseases and injuries that require a hip replacement are on the rise. According to the Canadian Joint Replacement Registry, 32,307 hip replacement surgeries were carried out in Canada between 2012-2013 [2].

Since the first attempt of hip replacement over 100 years ago [1], there have been many innovations in the concept and design of the hip implants. Different design iterations, material selection, and techniques have been developed to provide satisfactory hip replacements. One type of total hip replacements is the modular neck system. The design of the modular neck consists of attaching two components (i.e., femoral neck and femoral stem) by a Morse taper. The modular femoral neck is manufactured with different offset, length, and design configurations to allow surgeons to optimize the range of motion and the leg length of the patient and to allow for easy component replacement in case of revision.

The current modular femoral necks are made of titanium (Ti6Al4V) or cobalt chromium molybdenum (CoCrMo) alloys that are widely used in orthopedic applications due to their biocompatibility and recognized mechanical properties. However, the presence of the neck-

stem taper interface makes the taper junction vulnerable to fatigue fracture and wear-corrosion damage. Some *in vivo* modular neck retrievals have shown signs of early fatigue and advanced wear and corrosion at the neck-stem taper interface [3,4], which can lead to adverse tissue reactions [5], and prevent distraction during revision surgeries [4]. It is believed that the type of the modular neck material and the implant assembly procedure, for example applying a sufficient force to assemble the modular neck-stem taper interface, have an impact on the survivorship of the reconstructed hip.

Therefore, in the present study, test specimens consisting of CoCrMo femoral heads, Ti6Al4V modular stems, and Ti6Al4V and CoCrMo modular necks were tested and analyzed in terms of fatigue life, wear, corrosion, and distraction force of the modular neck. The tested specimens were the PROFEMUR® Total Hip Modular Neck System from MicroPort Orthopedics Inc.

1.2 Research Objectives

Material selection and assembly technique are critical for a reconstructed hip to ensure a sufficient performance and to avoid premature implant failure. From a material selection perspective, the Ti6Al4V modular neck, which has been employed longer than the CoCrMo modular neck, has shown signs of premature fatigue fracture. As a result, some manufacturers have considered CoCrMo as an alternative modular neck material due to the higher strength of the CoCrMo alloy over the Ti6Al4V alloy. Moreover, it is believed that the implant assembly procedure has an impact on the survivorship of the reconstructed hip, and some manufacturers recommend assembling the modular femoral components by applying blows with the surgical hammer in order to provide a robust interlock between the modular components.

The overall objective of this study was to simulate *in vivo* fatigue fracture, wear, and corrosion of modular necks at the neck-stem taper interface in a laboratory setting (*in vitro*) to better predict failure mechanisms and implant limitations.

The specific objectives were:

- To optimize the laboratory setup and testing conditions;
- To compare the effects of the modular neck material (Ti6Al4V vs. CoCrMo) and assembly technique (hand vs. impact assembly) on fatigue life, wear-corrosion resistance and distraction force of the necks using the developed laboratory setup.

2 Literature Review

2.1 Hip Joint

The hip joint (Figure 2.1) is a highly stable synovial ball-and-socket joint with a wide range of motions by the articulation of the femoral head with the acetabulum. The hip joint is a load-bearing joint where the internal (body weight and muscles forces) and external (reaction forces from the ground from daily activities, such as walking and ascending/descending stairs) forces are balanced.

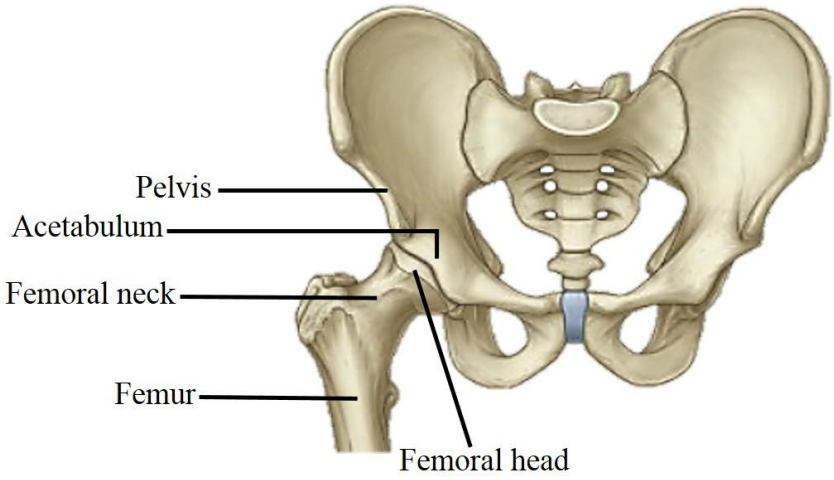

Figure 2.1: Bone configuration of the hip Joint (picture adapted from Drake et al., 2014 [6]).

The ball-and-socket structure allows the joint to produce motion by pivoting around three axes: the sagittal axis to produce adduction and abduction; the transverse axis to produce flexion and extension; and the longitudinal axis to produce internal and external rotations, as illustrated in Figure 2.2.

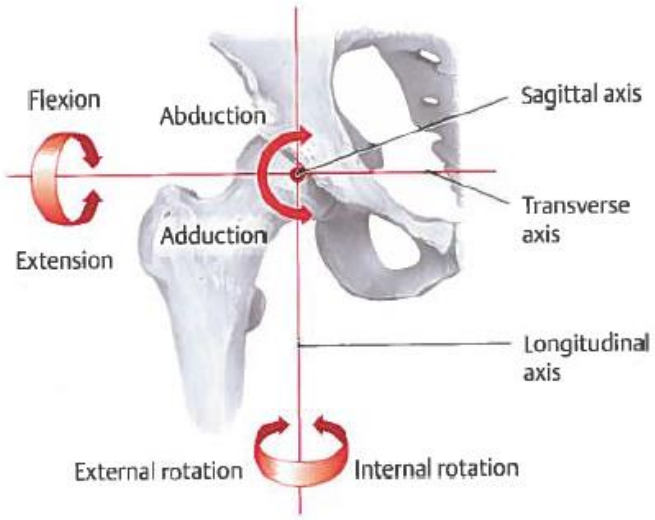

Figure 2.2: A diagram showing the axes of motion of the hip joint [7].

2.2 Hip Anatomy

The hip joint is a complex assembly of bones, ligaments, and muscles that produce motion and maintain the hip ability to function adequately. To describe the function of each element, the hip joint anatomy is divided as described in the following subsections.

2.2.1 Bone Structure

The two main bones of the hip joint are the femur (thigh bone) and the pelvis bone. The femur extends from the hip joint to the knee joint. At the top of the femur is the femoral head (a ball-shaped bone). The femoral head has a smooth surface except for a dent known as the fovea, from which a ligament called the ligamentum teres, shown in Figure 2.3, connects the femoral head to the acetabulum. The femoral head is connected to the femur by the femoral neck, a prismatic bone that offsets the head from the long axis of the femur. In adults, this offset, or neck inclination angle ranges between $125 \pm 5°$ (angle θ in Figure 2.3) [8].

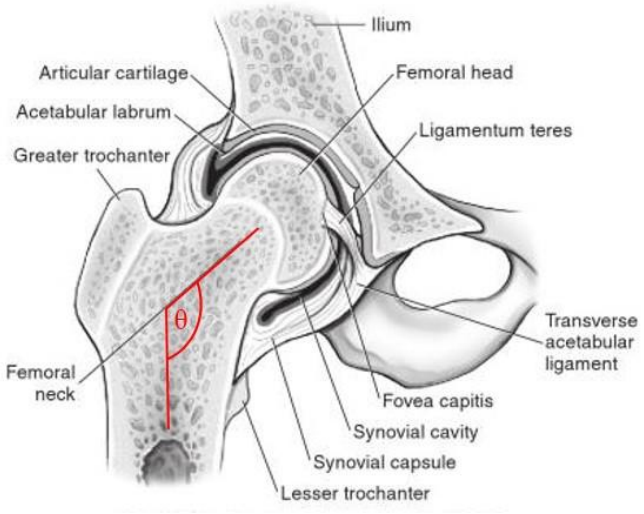

Figure 2.3: Anterior cross-section view of the right hip joint (picture adapted from Kelley et al., 2013 [9]).

The second bone of the hip is the acetabulum, which is a cavity on the lateral side of the pelvis that forms a deep socket for the femoral head. The shape of the acetabulum helps to stabilize the femoral head in the pelvis and to prevent dislocation. Like the femoral head, near the center of the acetabulum there is a dent called a fossa through which the ligamentum teres is attached.

2.2.2 Cartilage and Synovial Fluid

Articular cartilage covers the femoral head and the acetabular surfaces except for the fovea and the fossa areas. The synovial fluid has a very low viscosity and acts as a lubricant in the joint to reduce the friction between contacting cartilages of the bones [10]. The presence of the cartilage and the synovial fluid allows the femoral head and the acetabulum to articulate in a smooth motion to overcome the weight bearing and to protect the bone surfaces from wear.

2.2.3 Ligaments and Muscles

Ligaments connect bones together in the joint and help maintain congruency. There are two anterior ligaments (iliofemoral and pubofemoral) and one posterior ligament (ischiofemoral) that attach the femur to the pelvis. Together, they form the joint capsule that stabilizes the joint to minimize dislocation and contains the synovial fluid in the joint. The muscles surrounding the hip and femur are some of the strongest muscles in the body [11], and they provide further stability to the joint [12]. These muscles vary in shape and size to accommodate for the different hip motions.

2.3 General Bone Composition and Femur Strength

The bone strength is essential to protect the body organs and to assist the body to produce motion. Therefore, bones are subjected to numerous loads and stresses in our daily dynamic activities. Bones in nature have a degree of elasticity that allows them to bend in order to absorb energy and to avoid fracture [10].

Bones consist of organic and inorganic substances. Collagen (fibrils) and non-collagenous proteins are the major organic substances of bones [13], while calcium phosphate, also known as hydroxyapatite, and some other minerals such as potassium and magnesium represent the inorganic substances of bones [13]. Together, collagens and minerals form the bone matrix composite with an anisotropic structure. Collagens and minerals contribute to the bone stiffness and toughness. High amounts of collagen increase the toughness of the bone and make it less susceptible to fracture under load, while high quantities of mineral increase the stiffness but reduce the ductility of the bone [14].

The femur is the longest bone in the skeleton [15]. Like other long bones, the femur consists of two types of bones, cortical and cancellous bone, as seen in Figure 2.4. The cortical

(compact) bone forms the outer hard surface of the overall bone, and is recognized by its low porosity. The strength and modulus values of the cortical bone depend on the loading direction. As can be seen from Table 2.1, in average adults, cortical bone has better mechanical properties when subjected to longitudinal stresses than to transverse stresses. It also withstands greater stresses in compression than in tension regardless of the load direction. From Table 2.2, it can be seen that cortical bone absorbs more energy in the longitudinal direction than in the transverse direction. Its properties vary from one person to another depending on, amongst other factors, bone porosity and mineral content [16].

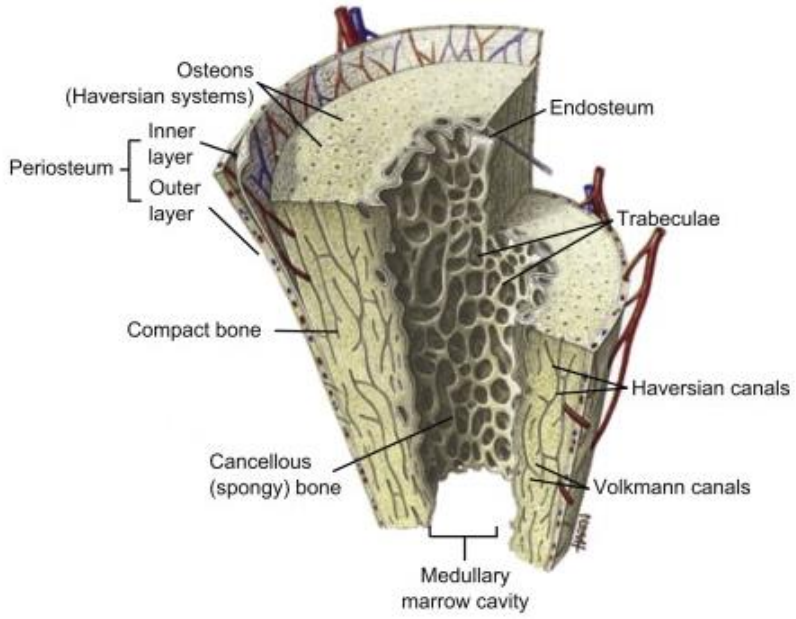

Figure 2.4: Dissection of a long bone showing the cortical and the cancellous bones [17].

Table 2.1: Ultimate stresses of human femur cortical bone [18].

Load direction	Load type	Failure stress (MPa)
Longitudinal	Tension	135
	Compression	205
Transverse	Tension	53
	Compression	131
Shear		71

Table 2.2: Elastic properties of human femur cortical bone [18].

Property	Value
Longitudinal modulus (GPa)	17. 0
Transverse modulus (GPa)	11.5
Longitudinal Poisson's ratio	0.46
Transverse Poisson's ratio	0.58
Shear modulus (GPa)	3.28

Unlike cortical bone, cancellous bone, also known as trabecular bone, has a high degree of porosity (spongy structure). Cancellous bone fills the inner cavity of the femur, as seen in Figure 2.4. Although determining the mechanical properties of cancellous bone is difficult due to the small size of trabeculae and the high porosity, studies have shown that cancellous bone has lower modulus of elasticity and ultimate stresses compared to cortical bone [19]. Furthermore, studies have shown that cancellous bone has higher modulus of elasticity and ultimate stress in compression than in tension, similar to cortical bone [19].

2.4 Hip Diseases

There is a variety of hip-related diseases and injuries. Those range from natural hip morphological disorders to fracture of the hip bones due to high loads or trauma, such as a car accident, as well as illnesses that occur as a result of the deterioration and wearing of the hip joint. According to the Canadian Institute for Health Information, the leading cause for hip replacements is degenerative arthritis [2]. Hip arthritis occurs as a result of the degeneration of the articular cartilage between the femoral head and the acetabulum [20], exposing the contact surfaces, and resulting to direct contact between the bones. This can lead to spurs [20], and bone deformation that cause pain and stiff joint. Figure 2.5 illustrates a hip suffering from arthritis.

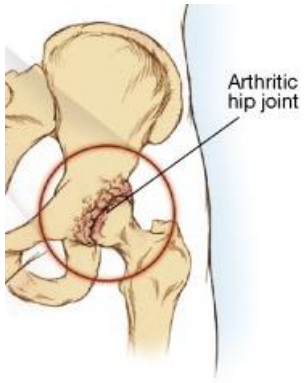

Figure 2.5: Hip arthritis disease [21].

The second common bone-related illness is osteoporosis. In this case, the bone structure becomes more fragile due to the deterioration of the bone (bone loss), as seen in Figure 2.6a, especially the cancellous bone around the femoral neck area, as seen in Figure 2.6b. Osteoporosis is also more common in elderly people, as the bone loss rate increases with aging [16].

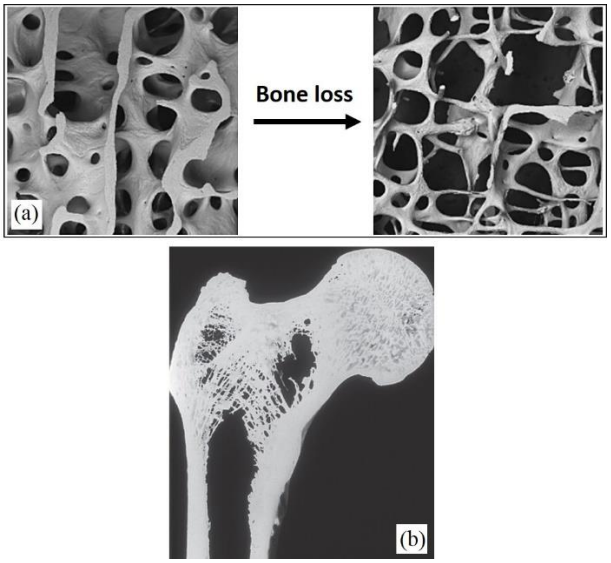

Figure 2.6: Illustrating images of osteoporosis: (a) Bone loss (deterioration) of cancellous bone matrix as a result of aging [22]; (b) A femur suffering from osteoporosis with a great amount of cancellous bone loss [23].

2.5 Total Hip Replacements (THR) Design

THR were introduced to surgically replace a hip joint that suffers from a disease or an injury when physical therapy and medication cannot improve the condition of the unhealthy joint. The purpose of THR is to replace the damage hip bones with an artificial implant that reliefs the hip pain and restores the function of the hip joint to carry the daily activities. The designs of THR have evolved greatly during the past few decades, guided by the development of new manufacturing techniques and follow-up studies of past designs. Although THR is more recognized to be intended for elderly patients, the demand for THR in younger and more active patients is on a steep rise. Therefore, the need for long lasting and reliable THR implants is increasingly becoming crucial.

Hip implant designs include the stem-type devices and the hip resurfacings. Although the THR terminology in the literature sometimes also refers to hip resurfacings, it will be

exclusively used in reference to the stem-type devices for the purpose of this thesis. In a THR, as seen in Figure 2.7, an acetabular cup (socket) is implanted in the pelvis to provide an articulating surface for the femoral head. The femoral head (ball) mates to a neck attached to a stem that is imbedded into the femur. There are two major methods to fix the THR components: the cemented and the cementless fixation. Different materials (polymers, metal alloys, and ceramics) are used to manufacture THR components. These materials are qualified to be implanted in the human body based on their biocompatibility, wear and corrosion resistance, relative stiffness to the bone, and mechanical properties that will allow them to withstand great amounts of stresses and torsional forces. With the variety of implant materials available, it is common to have a combination of materials for a single THR.

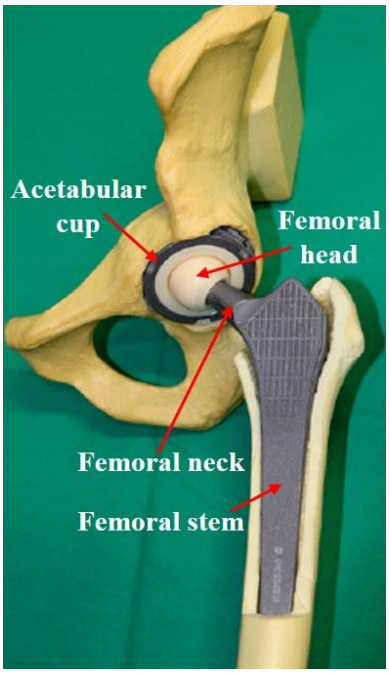

Figure 2.7: An illustration model of THR featuring a cementless fixated femoral stem and ceramic-on-ceramic bearing surface (picture adapted from Knahr, 2012 [24]).

Due to the large variety of patients' anatomy around the world, THR designs vary in terms of material selection, size, shape, version, range of motion, and neck angle (inclination) in order to satisfy the various needs. For each individual patient, a satisfactory THR depends not only on the THR design and material properties, but also on other factors such as the bone quality, surgeon skills, and surgical instrumentation used during the surgery. The differences in the available designs and trends of THR are discussed below.

2.5.1 Implant Fixation

As previously mentioned, there are two fixation methods in THR, cemented and cementless fixation. For cemented fixation, a bone cement is used as an intermediate layer between the implant and the bone. On the other hand, a cementless fixation depends on the bone ingrowth/ongrowth onto the implant surface; some aiding tools can be used, such as screws and spikes [25]. Regardless of the chosen method, the host bone requires some reaming and machining with medical tools to prepare it for the acetabular cup and femoral stem. The stability of the reconstructed hip is crucial. Therefore, poor fixation may lead to component loosening or dislocation, which can jeopardize the survivorship of the implant.

2.5.1.1 Cemented Fixation

For cemented fixation, a bone cement is utilized to stabilize and fix the implant component in place. The commercial bone cement used in orthopedics is polymethylmethacrylate (PMMA) that consists of two substances, a powdery substance of methylmethacrylate with an activator, and liquid monomers of methylmethacrylate with an initiator [26]. The concept of cemented fixation is to transfer and distribute the stresses more evenly from the stiff implant to the less stiff bone through the cement mantle, which has a modulus of elasticity of 1.1 - 4.1 GPa [26]. Bone cement does not adhere on the implant or the

bone. Its fixation relies on the osseointegration of the cancellous bone with the cement mantle on one side and on the mechanical interlocking with the acetabular cup/stem on the other side [27]. Cemented fixation is most appropriate for elderly patients who have poor bone quality or patients who suffer from osteoporosis [27].

Cemented fixation used to be the more conventional way in THR. However, one disadvantage of cemented fixation is that fixation is required at two interfaces, the implant-cement and the cement-bone interfaces. As a result, the implant is more vulnerable to loosening, especially when wear debris get in one of the bonding interfaces and weaken it. Also, bone cement cures in an exothermic reaction [27], which leads to heat release and could damage the tissue around the component and cause tissue necrosis [27].

2.5.1.2 Cementless Fixation

Cementless fixation is the most recent of the two fixation methods. The concept of cementless fixation is to replace the two bonding interfaces in cemented fixation with a single biological fixation between the implant surface and the bone. Therefore, bone osseointegration is the leading factor in cementless fixation. Cementless fixation is preferred for younger and healthier patients [27], whose bone quality is capable of creating the bone-implant interlock through bone remolding. Two types of cementless fixation surface coatings are used to facilitate fixation: bone ingrowth and bone ongrowth coatings. Bone ingrowth coatings are porous to allow the bone to grow into the pores of the coating (Figure 2.8), while bone ongrowth coatings have irregular texture that enhances bone growth on the surface (Figure 2.9).

The major drawback of cementless fixation is the mismatch in stiffness between metallic components and the bone. As a result, lower loads are transferred to the bone around

the implant, which can lead to bone resorption. This phenomenon is known as stress shielding and is associated with thigh pain, and in some cases, implant loosening [28].

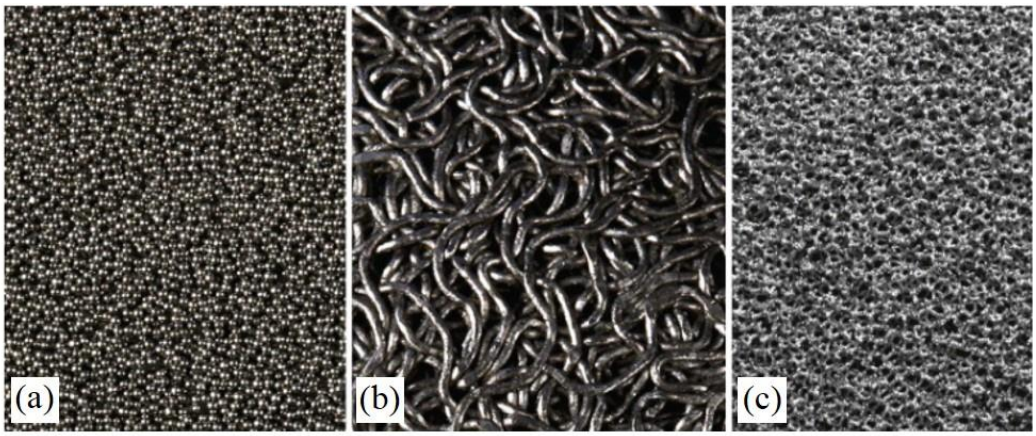

Figure 2.8: Ingrowth porous coatings: (a) Sintered beads; (b) Fiber mesh by diffusion binding; (c) Highly porous tantalum [25].

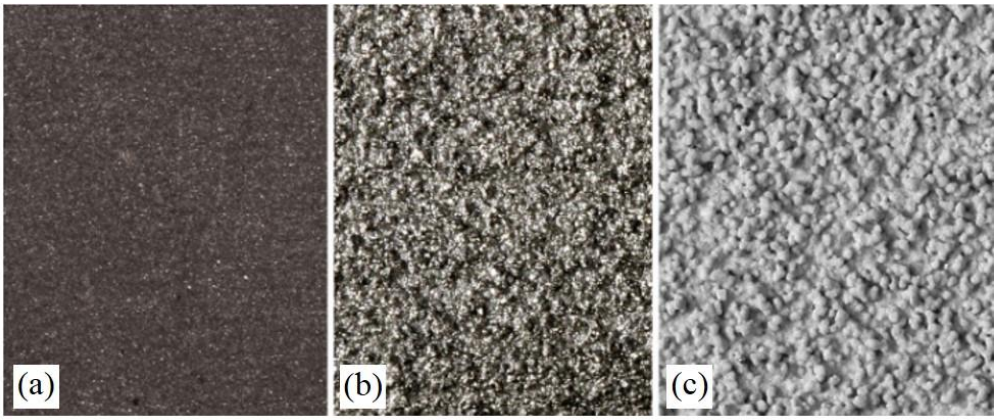

Figure 2.9: Ongrowth surface coatings: (a) irregular surface by grit blasting; (b) Titanium-textured surfaces by plasma spraying; (c) Hydroxyapatite-textured surfaces by plasma spraying [25].

2.5.1.3 Hybrid Fixation

A combination of the two fixation methods is sometimes used in a single THR, whereby a cementless fixation is used for the acetabular cup and a cemented fixation is used for the stem [29].

2.5.2 Acetabular Cup and Bearing Surfaces

The acetabular cup has a hemispherical or sub-spherical shape. It provides a smooth articulating surface for the femoral head while sustaining load bearing. The major concern of the acetabular cup from a mechanical point of view is the load-bearing capacity and resistance to wear as the hip joint is under continuous loading during routine daily activities.

The most common articulating load-bearing surface is metal-on-polyethylene (MoP) consisting of a metallic femoral head and a polyethylene cup. In early designs, the high wear rate of the conventional polyethylene was continuously raising concerns. Therefore, hard-on-hard articulating surfaces with low friction coefficients were developed, such as metal-on-metal (MoM), and ceramic-on-ceramic (CoC) bearing surfaces [25]. The currently employed metal alloys and ceramics have the desirable mechanical properties to withstand load bearing while producing smooth articulation in order to reduce the cup wear rate. However, some follow-up studies showed that MoM, in some cases, had the disadvantage of releasing metal particles and ions that could lead to adverse tissue reactions [24]. In modern acetabular cup designs, the cup is made of two components: the outer component is made of a metallic shell, and the inner component (liner) is made of polyethylene, metal alloys or ceramic, as shown in Figure 2.10.

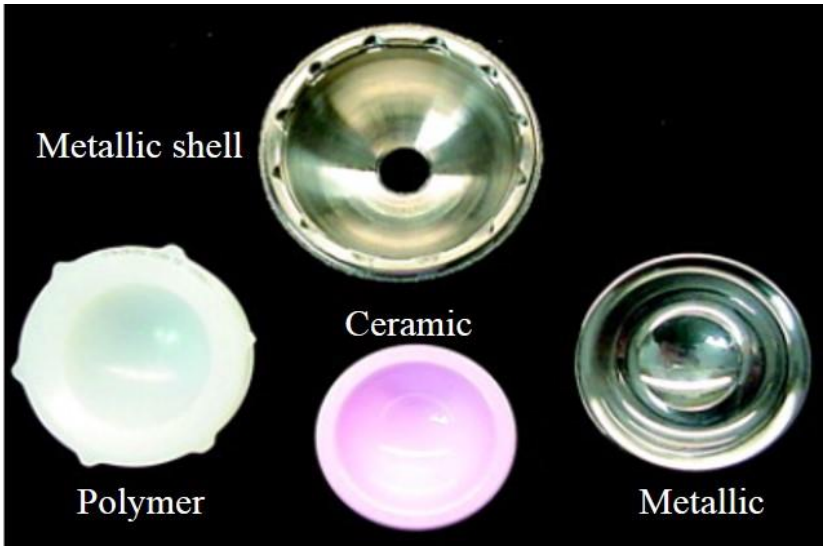

Figure 2.10: A metallic shell backing with three options of liners (picture adapted from Brown et al., 2009 [30]).

2.5.3 Femoral Head

The femoral head is a ball-shaped component that replaces the head of the femur bone. The femoral head is attached to the neck by a Morse taper. Similar to the acetabular cup, the head is required to withstand load-bearing with excellent wear resistance and smooth surface finish. Artificial femoral heads are made of metal alloys, mainly CoCrMo alloys, or ceramics. Femoral heads exist in different sizes, ranging from approximately 22 to 60 mm in diameter [31]. Larger head sizes have the advantage of increasing the range of motion of the reconstructed hip joint and the jump distance that is required to dislocate the head from the acetabular cup [32]. However, employing a large head can increase the wear damage of the liner in addition to requiring the use of a thin bearing liner. As a result, higher loads are more likely to damage the bearing liner and cause it to fracture [32].

2.5.4 Femoral Stem and Femoral Neck

Femoral stems are embedded in the femur to provide fixation and stability for the THR as well as to provide an anchor point for the femoral head. Stems are designed in different shapes and sizes to adapt to the hip anatomy and to achieve good stability when implanted in the femur. Straight stems are produced in many shapes, such as tapered, rectangular and cylindrical. In contrast, anatomic stems are curved in shape (curved anteriorly) to match the anatomic structure of the femur. Therefore, anatomic stems are manufactured for right and left hip joint separately. Some stems are designed with a proximal collar to maximize the force transfer to the bone around the femoral neck area and to enhance the stem stability [33]. Stems models vary a lot. To better illustrate the differences in stem designs, they are compared below based on the following aspects: modularity and methods of fixation.

2.5.4.1 Modularity of Femoral Components

Similar to acetabular cups, there are two types of systems, the most common traditional modular head system and the modular neck system. For the modular head system, the femoral stem and the femoral neck are manufactured as one component, as seen in Figure 2.11. The advantage of this system is that it is simple and less expensive to produce than modular neck system, and there is fewer risks of relative micromotion between the femoral components since there is only one attachment interface (i.e., head-stem interface). However, from a revision point of view, the whole stem has to be replaced in case of femoral neck fracture or if the head-stem interface suffered advanced corrosion, even if the stem is well fixed.

On the other hand, the modular neck system, which is considered as one of the latest innovations in THR [27], consists of three components, a modular stem and a modular neck to which the head is attached, which makes this system more costly due to the design complexity.

The concept of the modular neck design, as seen in Figure 2.12, is to provide a wider range of neck length, offset, and version to adjust the range of motion of the reconstructed hip [25]. This wide range of configurations makes the modular neck systems a good choice for complex anatomy surgeries. Modular neck systems also overcome the limitation of the modular head systems when it comes to revision, as only the damaged neck can be replaced. However, the modular neck design requires two attachment interfaces, head-neck and neck-stem interfaces. The introduction of the neck-stem interface makes the femoral component more vulnerable to mechanical damage such as fretting and corrosion due to relative micromotion between the stem and the neck, and the accumulation of body fluids in the neck-stem interface.

Figure 2.11: Modular head design [34].

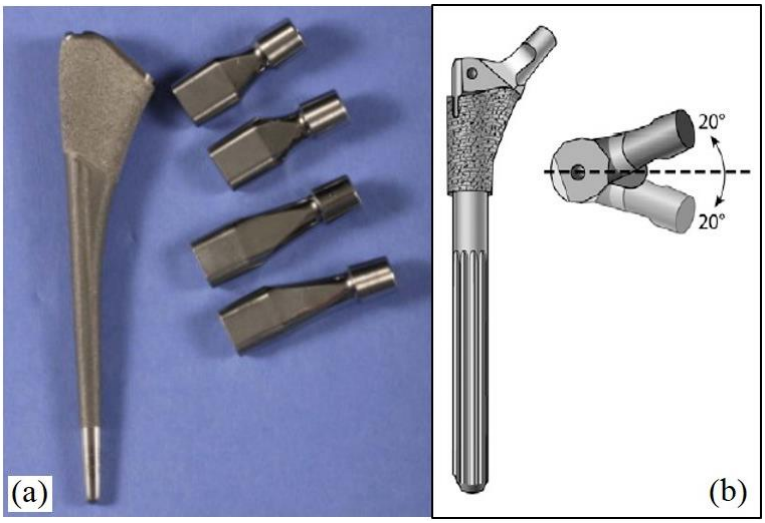

Figure 2.12: Modular neck design: (a) Modular necks with different lengths and angles of inclination [25]; (b) Different version alignments of modular necks [33].

2.5.4.2 Methods of Fixation of Femoral Stems

Stems are fixed by cemented or cementless fixation. Cemented stems were first introduced by Sir John Charnley in 1960s [26]. Cemented stems are designed with wider medial and lateral surfaces to enhance the compression forces from the stem on the cement mantle for a better locking mechanism. Their surface finish can be matt (rough) or polished (smooth). Some stems are designed with grooves to improve the stem-cement bonding and the overall stability of the stem.

Cementless stems, which were introduced in the 1970s [33], have only one bonding interface: the stem-bone interface. To allow osseointegration, the stems are manufactured with bone ingrowth/ongrowth coatings. The primary fixation location of cementless stems differs between manufacturers [27]. Some stems are coated at the proximal end of the stem, while other stems have fully coated surface to allow for fixation along the femur cavity. This variety

in surface coatings is developed in an effort to achieve the best possible stability of the reconstructed hip.

2.5.5 Morse Tapers

Morse tapers are used to provide a mechanical interlock between the head-neck and neck-stem (in modular neck systems) interfaces. Therefore, each THR has at least one Morse taper junction. The use of Morse tapers allows combining two different materials in one THR. The common shapes of tapers in THR are curricular and trapezoidal, as shown Figure 2.13. They are machined in different sizes ranging from 8/10 to 14/16 [31]. The numbers identify the roughly proximal and distal diameter (width) in mm [31]. Morse taper junctions are of a crucial factor in the survivorship of the femoral components of the reconstructed hip. Under loading, micromotion between the attached components can destroy the component surfaces and make them vulnerable to fretting and corrosion damage.

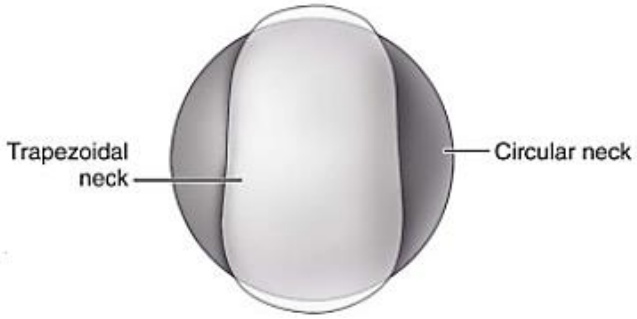

Figure 2.13: A sketch showing the difference in shape of Morse tapers used in THR [25].

2.6 Implant Materials

Materials utilized for orthopedic purposes are selected based on their biocompatibility, tribological performance and mechanical properties. Due to the nature of the body environment that contains a diversity of potential corrosive agents such as body fluids and

organic particles, biomaterials need to resist corrosion and wear damage. Another aspect in material selection is mechanical strength. The implanted materials are under constant load cycles throughout daily activities. Therefore, they have to sustain a great amount of loads without failing under fatigue and as such, ductile materials are preferred to avoid catastrophic failure (i.e., brittle fracture), which can limit the function of the implant and require immediate revision. Another important aspect affecting the material selection in THR is the stiffness. Too stiff materials can cause stress shielding and pain in the femur [25]. The biocompatibility principle and the mechanical properties of the currently employed materials in THR (polymers, metal alloys, and ceramics) are listed and discussed below.

Biocompatibility is essential as the implanted components are required to last for a long period of time. Biocompatibility is defined as the ability of a material to perform its purpose adequately with an appropriate host response [35]. Therefore, the main consideration of determining the biocompatibility of a material is how safely the material will perform without causing any harm to the body, either locally or systematically while maintaining its mechanical properties [35]. On the other hand, there are some bioactive materials used in THR, such as hydroxyapatite, that are intended to react positively with the host bone to provide osseointegration [27]. It is important to consider the fact that the biocompatibility of a given material is different from one application to the other due to the differences in part design and body environment (i.e., host bone or organ).

2.6.1 Polymers

Besides the use of PMMA as a bone cement, polyethylene is used in THR for bearing surface in the acetabular cup. Polymers are generally used for their desirable chemically inert characteristic along with their high toughness, ductile fracture, and reasonable resistance to

abrasion wear [27]. In addition, they are simple and inexpensive to produce. For the bearing surface, the cup liner can be made of ultrahigh molecular weight polyethylene (UHMWPE). In order to improve the fatigue strength and oxidative degradation, the UHMWPE can be sterilized with plasma gas or stabilized with irradiation in an inert atmosphere during manufacturing [27].

Despite the surface modifications and wide use of UHMWPE, it is known to be prone to wear damage and to the release of wear particles. Therefore, highly cross-linked polyethylene (HXLPE), which has an improved wear resistance, has been introduced to replace the UHMWPE [25]. The HXLPE consists of a highly crossed molecular structure, which increases the wear resistance of the polymer. *In vitro* simulation of HXLPE showed a reduction of 80 - 90 % in wear damage [25].

2.6.2 Metal Alloys

Metal alloys are the most used materials in implants generally due to the variety of available metals and the ability to enhance their mechanical properties by metal alloying. Stainless steel, titanium and cobalt chromium alloys are employed in THR due to their high tensile strength, ductility, corrosion and wear resistance, and their passivation property. Metals are often used to fabricate femoral and acetabular components. With the proper surface finish, low friction components are produced for load-bearing and articulation purposes. Metallic components can be cast, forged or wrought [27].

2.6.2.1 Stainless Steel Alloys

Stainless steel alloys are widely used in surgical tools due to their corrosion resistance and fracture strength [27]. The corrosion resistance of stainless steels can be increased by chromium addition, while nickel addition contributes to increasing the strength and hardness

of the alloy [13]. Stainless steels have the advantage over titanium and cobalt chromium alloys in their high ductility [27]. However, stainless steel component fractures in early femoral designs, their lower biocompatibility and corrosion resistance compared to titanium and cobalt chromium alloys, as well as their susceptibility to pitting and crevice corrosion limited their use in THR [27]. Consequently, they have been widely replaced by titanium and cobalt chromium alloys.

2.6.2.2 Titanium Alloys

Titanium alloys (specifically Ti6Al4V) are the most preferred materials for THR components because of their superior biocompatibility [25]. Because of the presence of the titanium oxide layer, the titanium alloys are known for their high corrosion resistance. In addition, they have the lowest modulus of elasticity among metallic alloys, as seen in Table 2.3. This makes them favourable candidates for cementless components as their stiffness is closest to that of the bone, which minimizes stress shielding, reduces thigh pain, and improves the stresses transferred from the implant to the hosting bone. On the other hand, the wear resistance of titanium alloys is lower than that of cobalt chromium alloys. In order to improve titanium wear resistance, the produced components can be treated with ion implantation and TiN ceramic coating [27].

Table 2.3: Typical mechanical properties of THR materials [27].

Material	ASTM designation	Modulus of elasticity (GPa)	Ultimate tensile strength (MPa)	Tensile yield strength (MPa)	Hardness (GPa)
Polymers					
Unirradiated UHMWPE	ASTM F648	0.85	46–58	22	—
Irradiated UHMWPE	—	0.94	43–55	24	—
Highly cross-linked UHMWPE	ASTM F2565	0.74	43–51	19–21	—
Ceramics					
Al_2O_3	ASTM F603	366	500	—	20–30
ZrO_2	—	201	800	—	15
Al_2O_3/ZrO_2 composite	—	350	1390	—	17.2
Metals					
Stainless steel	ASTM F138	190	930	241–820	1.3–1.8
CoCrMo	ASTM F75	210–250	655–1275	207–950	5.5
Ti–6Al–4V	ASTM 136	116	965–1100	897–1034	3
Zr–2.5Nb (oxidized surface)	—	98	—	—	Bulk: 3 Surface: 12.1

2.6.2.3 Cobalt Chromium Molybdenum Alloys

The most common cobalt-based alloy that is currently used in THR is the cobalt chromium molybdenum (CoCrMo). The main use of CoCrMo alloys is in cemented stems and femoral heads. The presence of chromium and molybdenum increases the corrosion resistance (through the formation of a chromium oxide layer) and the strength, respectively [27]. In general, cobalt-based alloys have higher ultimate tensile strength than titanium alloys, as seen in Table 2.3. This makes them perform better in resisting fatigue fracture. However, the high modulus of elasticity of CoCrMo alloy makes it much stiffer than bone. Therefore, cemented fixation is favorable for CoCrMo alloy stem, whereby the bone cement acts as an intermediate layer to transfer the stresses from the component to the host bone.

2.6.3 Ceramics

The primary use for ceramics in THR is bearing surface components (i.e., acetabular liners and femoral heads). Ceramics that are used in THR are alumina (Al_2O_3) and alumina/zirconia composites known as zirconia toughened-alumina (ZTA). The ZTA ceramic composite has a combination of properties of the two ceramics. As seen in Table 2.3, ZTA has an improved ultimate tensile strength while maintaining reasonable modulus of elasticity and hardness. Ceramic components are manufactured using powder metallurgy by hot isostatic pressing and sintering. The advantages of employing ceramics as THR materials are their biocompatibility and corrosion resistance [26]. Also, their higher hardness compared to metal alloys increases their wear resistance against scratching and reduces particle release [27]. They also have a low friction coefficient and good lubrication properties that make them superior for articulating components.

The limitation of ceramics in THR is that they have very high modulus of elasticity compared to the cortical bone, which makes them unlikely candidates for femoral stem components. Moreover, their brittle behaviour compared to metal alloys, make them susceptible to sudden fracture. Another disadvantage of ceramics is that they require special care when being oriented during surgery to avoid damaging the parts during assembly [25].

2.7 Failure Mechanisms

2.7.1 Fatigue

Fatigue fracture can occur in all types of materials but more significantly with metals. It is estimated that 90% of metallic failures are due to fatigue [36]. A fatigue failure occurs when a component is subjected to a cyclic loading or stress, even though the load is lower than the component tensile strength [34]. The failure develops in three stages, starting with crack

nucleation (crack initiation), followed by crack propagation in a slow pace as the component is being subjected to cyclic loading, and finally sudden fracture that takes place when the remaining load-bearing cross-sectional area can no longer sustain the applied stress. An example of fatigue failure is shown in Figure 2.14.

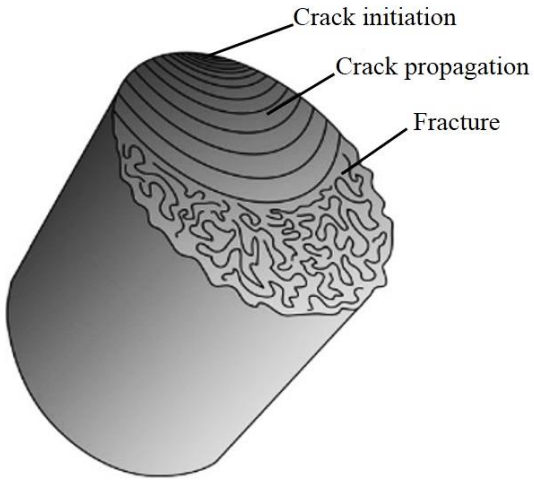

Figure 2.14: Typical fatigue failure of ductile metals [37].

There are many factors to consider to increase the fatigue life of a component, such as selecting a material with high tensile strength for the intended application, eliminating surface defects from machining processes as much as possible, avoiding stress concentrations (notch), and considering the environmental impact, such as corrosion, on the component [36,38].

Although materials used in THR are ductile, there are many factors that can influence the fatigue life of hip implant components. First, the weight and physical activities of the patient can influence the magnitude of stresses on the THR [37]. Other parameters, such as fretting and corrosion, can decrease the fatigue strength of the metallic components. Also, unlike general components in mechanical applications, there is no chance to inspect the

implanted THR. Therefore, extensive *in vitro* testing is necessary to ensure a reliable THR component design against fatigue.

2.7.2 Wear

Wear is the process of material removal off a surface due to interaction (relative motion) with another surface [34], leading to a decrease in the durability and longevity of the component. Wear is influenced by dynamic and environmental parameters [39]. Although wear is inevitable, the knowledge of the intended application of a component is required for proper engineering design and material selection. The wear resistance can also be increased by improving other tribological properties of the material/application, such as lowering the surface friction and applying adequate lubrication.

The significance of wear damage is that it can affect other material properties and induce other mechanical failures, such as corrosion and fatigue. In THR, wear can be crucial in two aspects: firstly, a degradation of material surface and geometry of articulating components, resulting in a reduced life-time of the THR and wear particle release that can cause adverse tissue reactions; and secondly, fretting and corrosion damage of the mating interfaces of modular components. There are many wear modes that occur in materials, and it is common that a combination of multiple wear modes occurs [34]. For the purpose of the present study, the most prominent wear modes and mechanisms in THR are explained below.

2.7.2.1 Abrasive Wear

Abrasive wear is the material removal from one surface as two components slide in relative motion. Abrasive wear can occur by two mechanisms: two-body and third-body wear mechanisms. In the two-body wear mechanism, shown in Figure 2.15a, surface asperities from the harder surface damage the softer surface [27]. In the third-body wear mode, shown in

Figure 2.15b, hard particles, for example wear particles between the two surfaces, can cause wear damage along the sliding surfaces [27]. Abrasive wear results in many types of surface damages, such as wedge formation, plowing, and cutting through the surface [38].

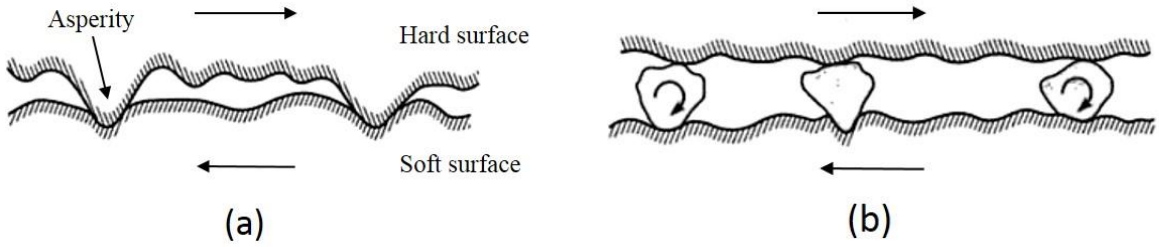

Figure 2.15: Schematics of abrasive wear mechanisms (picture adapted from Bhushan,1999 [40]): (a) Two-body; (b) Third-body.

2.7.2.2 Adhesive Wear

Adhesive wear occurs when two mated surfaces slide against each other with poor lubrications and higher friction between them. Upon loading, the two surfaces are joined together due to micro-welding (cold-welding) or other adhesion mechanisms [27]. With further relative motion, fragments from one of the surfaces are then pulled-out and bonded with the counter surface [37], as shown in Figure 2.16, leading to an alteration of the surface geometry and shape.

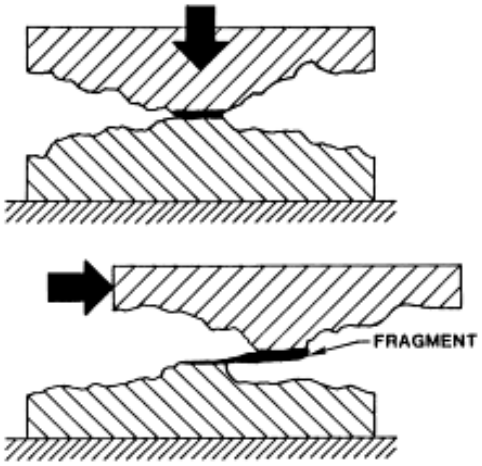

Figure 2.16: A schematic illustration of the adhesion wear process (picture adapted from Fitch, 1992 [41]).

2.7.2.3 Corrosive Wear

Corrosive wear occurs when a material is employed in a corrosive environment. Corrosive particles form on the surface by chemical reactions and are subsequently removed by wear [39], as shown in Figure 2.17, exposing the surface to further corrosion attack and pitting [37]. The rates of oxide product formation and oxide layer removal determine the severity of the corrosive wear. For example, titanium is vulnerable to corrosive wear as damaged oxide layer is regenerated due to the inherent passivity of titanium. Repeated material removal and re-passivation can cause a substantial loss of the bulk material, which makes titanium a poor choice as a bearing surface [37].

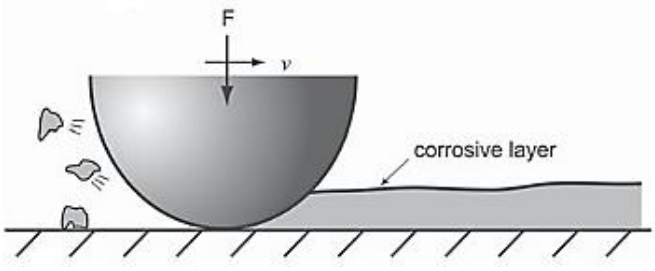

Figure 2.17: Corrosive/oxide layer removal due to corrosive wear [37].

2.7.2.4 Fretting Wear

Fretting wear or fretting occurs when two surfaces in contact are subjected to cyclic loading. However, unlike all previously mentioned wear modes, the surfaces are not in relative macromotion. Fretting is rather initiated by vibrations between the surfaces due to mechanical loading and micromotion ranging between 20 - 200 μm [37]. Fretting is common in modular THR component taper interfaces (i.e., head-neck and neck-stem). Furthermore, fretting debris can induce abrasive wear, thus, increasing the wear damage [37]. Fretting can also be associated with corrosion and fatigue failures. Fretting corrosion occurs when the oxide layer is damaged by fretting, exposing the surface to corrosion attack. Moreover, fretting can initiate micro-cracks into a component, and with repeated loading cycles, a fatigue fracture can occur.

2.7.3 Corrosion

Corrosion can be defined as deteriorative loss of material properties as a result of chemical or electrochemical reactions with the surrounding environment [42]. Corrosion damage has a major economic impact in the materials industry, requiring the development of corrosion prevention methods and replacement of corroded parts [36]. In general, corrosion itself does not lead to catastrophic failure; however, it can reduce the useful life of a component.

The corrosion of metals is an electrochemical reaction by which electrons travel from one area to another in the same component, or to another component [36]. There are four elements that are required for an electrochemical reaction/cell to occur: an anode, a cathode, an electronic path, and an electrolyte (ionic path) [42]. The anode is the area at which corrosion occurs, liberating electrons in the following oxidation reaction:

$$M \longrightarrow M^{n+} + ne^{-}$$

The cathode, on the other hand, is the area that consumes the electrons in the following reduction reaction:

$$M^{n+} + ne^- \longrightarrow M$$

To complete the electrochemical process, the electronic path (i.e., metal/component) allows the electrons to migrate from the anode to the cathode [42]. Lastly, the electrolyte, which is an electrically conductive solution, allows the positively charged ions to travel from the anode to the cathode [42].

In order to rank metals based on their natural tendency to corrode (i.e., chemical reactivity), the electromotive force (emf) series (shown in Table 2.4), was developed [36]. Metals are ranked based on their electrode potential with comparison to hydrogen (reference element). Inert metals that have higher electrode potential are listed at the top of the table, while active metals that have lower electrode potential are listed at the bottom of the table.

Table 2.4: The electromotive force (emf) series [36].

	Electrode Reaction	*Standard Electrode Potential, V^0(V)*
	$Au^{3+} + 3e^- \longrightarrow Au$	+1.420
↑	$O_2 + 4H^+ + 4e^- \longrightarrow 2H_2O$	+1.229
	$Pt^{2+} + 2e^- \longrightarrow Pt$	~+1.2
	$Ag^+ + e^- \longrightarrow Ag$	+0.800
Increasingly inert (cathodic)	$Fe^{3+} + e^- \longrightarrow Fe^{2+}$	+0.771
	$O_2 + 2H_2O + 4e^- \longrightarrow 4(OH^-)$	+0.401
	$Cu^{2+} + 2e^- \longrightarrow Cu$	+0.340
	$2H^+ + 2e^- \longrightarrow H_2$	0.000
	$Pb^{2+} + 2e^- \longrightarrow Pb$	−0.126
	$Sn^{2+} + 2e^- \longrightarrow Sn$	−0.136
	$Ni^{2+} + 2e^- \longrightarrow Ni$	−0.250
	$Co^{2+} + 2e^- \longrightarrow Co$	−0.277
	$Cd^{2+} + 2e^- \longrightarrow Cd$	−0.403
	$Fe^{2+} + 2e^- \longrightarrow Fe$	−0.440
Increasingly active (anodic)	$Cr^{3+} + 3e^- \longrightarrow Cr$	−0.744
	$Zn^{2+} + 2e^- \longrightarrow Zn$	−0.763
	$Al^{3+} + 3e^- \longrightarrow Al$	−1.662
	$Mg^{2+} + 2e^- \longrightarrow Mg$	−2.363
	$Na^+ + e^- \longrightarrow Na$	−2.714
↓	$K^+ + e^- \longrightarrow K$	−2.924

Even with corrosion-resistant metals, there are many factors that influence the occurrence and acceleration rate of a corrosion attack, such as the acidity of the medium (i.e., pH level), the oxidation/reduction characteristics of the environment, and elevated temperatures [42]. The corrosion resistance of metallic components can be increased by applying protective coatings and by metallic alloying. Similar to wear, corrosion can occur in many different forms. Some of the major corrosion forms are explained below.

2.7.3.1 Uniform Corrosion

Uniform corrosion is the most recognized form of corrosion because it affects most of the exposed surface of a component and it can be detected easily. It occurs due to the formation and movement of multiple anodes and cathodes at the same time along the component surface [42]. It can affect large surface areas uniformly, especially when components are exposed to atmospheric environment. Because of the bulk nature of the uniform corrosion, it is easy to predict and calculate the corrosion rate and modify/replace the corroded parts accordingly.

2.7.3.2 Pitting Corrosion

In contrast to uniform corrosion, pitting is a very localized form of corrosion, where pits are formed on the surface and penetrate inside the component [36], as shown in Figure 2.18. Pitting usually occurs in materials at locations where the component is damaged due to surface defects or variation of surface composition [36]. Pits can also occur at discontinuities of surface coatings [38]. In pitting, the pit becomes the anode and the undamaged surface is the cathode. Pitting can occur as a group of pits or as an individual pit, which is problematic, because the pit can be small in size and hard to be detected. In THR, pitting corrosion can occur on the taper surface of the modular components.

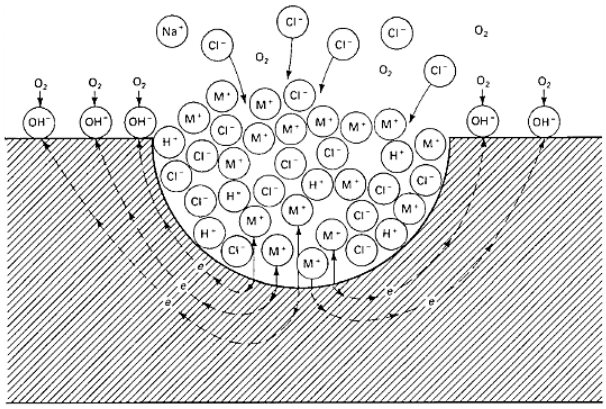

Figure 2.18: Pitting corrosion of a component in aerated sodium chloride solution [42].

2.7.3.3 Crevice Corrosion

This is another form of highly localized corrosion that occurs in narrow spacing (gaps) between metallic parts [42], which makes crevice attack hard to be detected as well, as shown in Figure 2.19. Crevice corrosion occurs when the oxygen concentration of the electrolyte inside the crevice drops substantially below the overall solution concentration outside the crevice [42]. As a result, the crevice acts as the anode, while the adjacent area becomes the cathode [42]. Passive materials are known to be susceptible to crevice corrosion, especially in environments with high concentrations of H^+ and Cl^- ions, which can break through the passive layer [36]. In THR, crevice corrosion can occur at the head-neck and neck-stem interfaces.

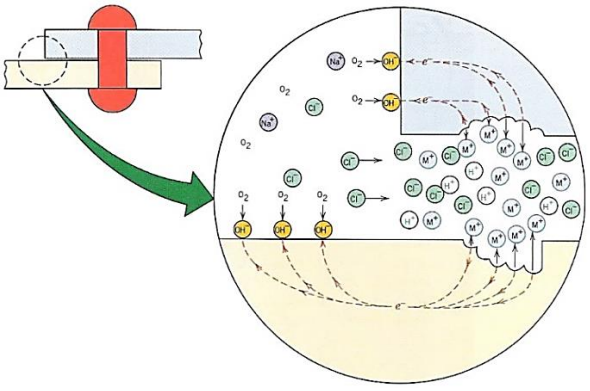

Figure 2.19: An example of crevice corrosion between two surfaces [36].

2.7.3.4 Galvanic Corrosion

This form of corrosion occurs when two dissimilar metals with different electrical potentials are electrically coupled and exposed to the same electrolyte [42]. The leading factor of galvanic corrosion is the tendency of metals to react with other metals in a certain environment. Therefore, in order to rank the relative reactivity of metals with each other, the galvanic series, shown in Table 2.5, was established. From the galvanic series, when two metals are coupled together, the inert (noble) metal becomes the cathode, while the active metal becomes the anode [42]. Although the galvanic series does not provide details about the corrosion rate of metals, it provides designers the required knowledge about employing specific metals in a particular environment.

Table 2.5: The galvanic series of metals and alloys in seawater [36].

	Platinum
	Gold
	Graphite
	Titanium
	Silver
	316 Stainless steel (passive)
	304 Stainless steel (passive)
↑	Inconel (80Ni–13Cr–7Fe) (passive)
	Nickel (passive)
	Monel (70Ni–30Cu)
Increasingly inert (cathodic)	Copper–nickel alloys
	Bronzes (Cu–Sn alloys)
	Copper
	Brasses (Cu–Zn alloys)
	Inconel (active)
	Nickel (active)
	Tin
	Lead
Increasingly active (anodic)	316 Stainless steel (active)
	304 Stainless steel (active)
	Cast iron
↓	Iron and steel
	Aluminum alloys
	Cadmium
	Commercially pure aluminum
	Zinc
	Magnesium and magnesium alloys

A major factor that contributes to the acceleration of the galvanic corrosion is the difference in the electrical potential between the selected metals, as a higher difference will accelerate the corrosion rate [42]. Therefore, selecting two materials with minimal electrical potential difference can reduce the rate of the galvanic corrosion. Another important factor is the anode-to-cathode surface area ratio, as a bigger area of the inert metal compared to the active metal will accelerate the corrosion process, and vice-versa [36].

2.8 Forces on the Hip Implant

During daily activities, the femoral head of a hip implant can be subjected to a resultant force with three force components F_x F_y, and F_z [43], as seen in Figure 2.20. These force component vectors cause load and torsion moments that can affect the stress levels and stability of the hip implant. The force components differ in magnitude due to the different activities exercised by the patient. For example, it is estimated that the force acting on the hip reaches 260 % of the body weight when descending stairs, while it can be as low as 238 % of the body weight during normal walking [43]. Moreover, the force vectors can differ across hip implants due to the variety of hip implant geometry and orientation (e.g., the version angle). Experiments with instrumented implants have shown that the F_z force (Figure 2.20) is the largest contributor to the overall applied force on the hip joint [43] and can result in high a bending moment and stress on the implant.

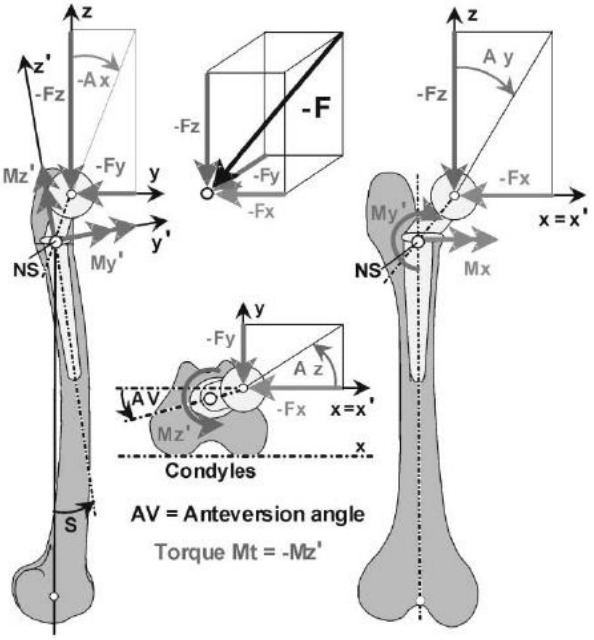

Figure 2.20: A coordinate system of the measured forces on the hip implant [43].

2.9 *In Vivo* Modular Neck Failures and Biological Consequences

According to the Food and Drug Administration (FDA) database, which monitors adverse instances and tracks public recalls of medical products, there have been several recalls for modular neck hip implants from multiple manufacturers in recent years [44]. Reasons for recalls include high rates of modular neck fracture and the associated high risk of subsequent health issues on the patient [44]. Although the actual number of hip implants that have failed due to modular neck fracture is unknown, there have been several reports of fractured modular femoral long necks in the past few years [3,4,45-48]. For example, Dangles et al. reported a case of a neck that failed after 42 months of implantation [3]. In most of the reports, the neck was made of Ti6Al4V alloy [4,45]. On the other hand, Mencière et al. reported a case of a CoCrMo neck that failed after only 22 months of implantation [48]. Abrasion, fretting, and corrosion are also observed on the fractured necks [3,4,48]. Furthermore, these mechanical and electrochemical mechanisms can result in producing particles and releasing ions which

can lead to adverse tissue reactions and implant failure [5,49]. Reports have mentioned that extracting the fractured neck fragment (i.e., neck taper) from the stem pocket was not achievable [4,45-48], and therefore, the well-fixed femoral stems were also revised. Examples of fractured modular Ti6Al4V and CoCrMo necks are shown in Figures 2.21 and 2.22, respectively.

Figure 2.21: *In vivo* fracture of a long Ti6Al4V modular neck with the arrows pointing at the fretting and corrosion damage [4].

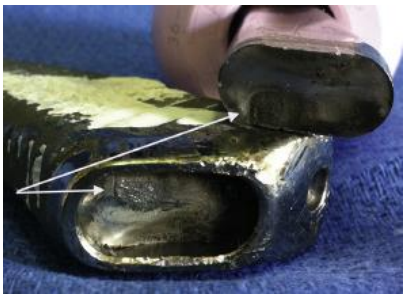

Figure 2.22: Image of an *in vivo* fractured long CoCrMo modular neck showing the fractured neck fragment inside the stem pocket [48].

3 Methodology

3.1 The Investigated THR System

The specimens used in this study were the cementless PROFEMUR® Total Hip Modular Neck System from MicroPort Orthopedics Inc., formerly Wright Medical Technology Inc. CoCrMo femoral heads with a 28 mm diameter as well as size 9 cementless Ti6Al4V femoral stems (139 mm length) coated with plasma spray were used for all implants (Figure 3.1). The modular femoral neck material (made of Ti6Al4V or CoCrMo) was the only variable in the tested specimens. Long and straight (no version) modular femoral necks with 8° varus/valgus orientation and 12/14 taper size (Figure 3.1) were selected as they represented the worst case scenario in terms of increased bending moment upon loading.

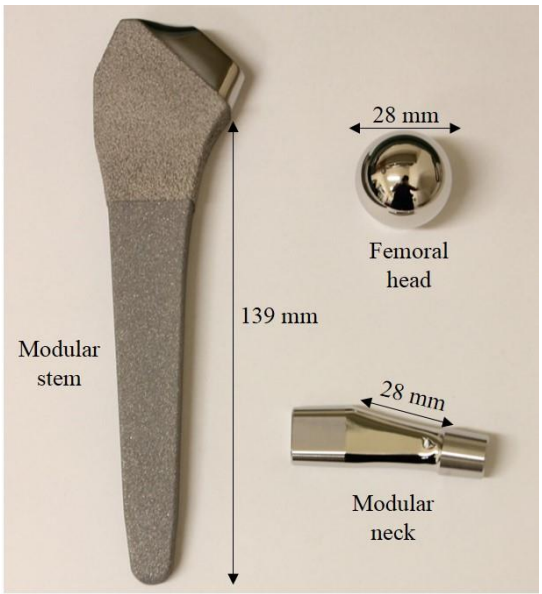

Figure 3.1: The PROFEMUR® Total Hip Modular Neck System investigated in this study.

3.2 Experimental Procedures

Generally, *in vitro* simulations of orthopedic implants require the consideration of many factors that affect the performance and service life of implants, such as the mechanical loading

level and the environmental parameters. Due to the differences in human body physiology between individuals, it is arguably impossible to match all real-life effects on implants in the laboratory setting. As a result, test protocols, such as load level, test duration, and suitable bath solution, were developed to better suit the intended purpose of implant investigations.

In this study, the *in vitro* simulator was designed to induce fatigue, wear, and corrosion damage at the modular neck taper of THR. Also, the necks were cleaned before mechanical tests in an ultrasonic bath (model B3500A-DTH, VWR, Mississauga, ON, Canada), as suggested by ASTM F2009 Standard. This allowed removing any contaminants that could accumulate on the modular necks during shipping, handling, and storage. The cleaning procedure was adopted from the Rush University Medical Center, Department of Orthopedic Surgery, Chicago, IL, USA, with some minor adjustments. The detailed steps of the cleaning procedure performed in this study are found in Appendix A. The testing setup, fixtures design/modifications, and the developed test protocol are described in the following sections of this chapter.

3.2.1 Heating System

The heating system consisted of dual heaters connected in a parallel circuit. The primary aim of using two heaters was to rapidly heat up the test solution at the beginning of the test, and divide the electrical load on both heaters to minimize the likelihood of heaters failure due to overload, especially for the lengthy corrosion tests. Furthermore, using two heaters provided a mean of redundancy in the heating system in case one of the heaters failed.

The initial heating system incorporated heaters of flexible silicone rubber heat sheets. These heaters had an adhesive back surface that allowed them to be fixed onto the inner wall of the solution bath. They were selected due to their chemically inert characteristics and

flexibility of use. However, although they supplied the required power and temperature for the tests, they repeatedly failed at the soldering junction, as seen in Figure 3.2. As a result, a more durable cartridge immersion heater made of corrosion resistant 316 stainless steel was used for the subsequent experiments (Figure 3.3). Sheet metal adaptors made of 304 stainless steel were used to place the heaters inside the tank. The sheet metal adaptors were bent at one end to form a hook around the tank, while the heaters were submersed into the solution at the other extended end of the sheet metals through drilled holes.

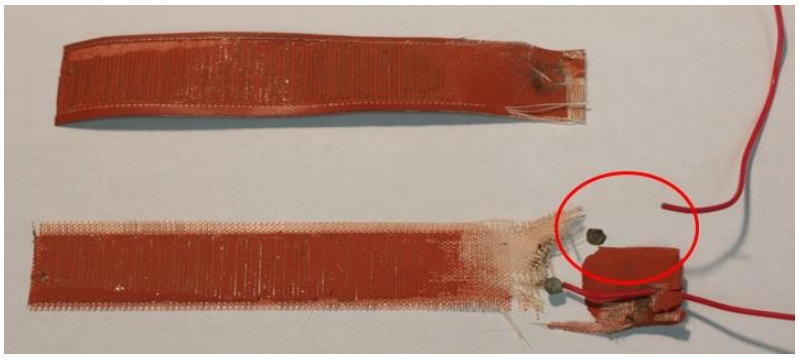

Figure 3.2: Failed flexible silicone rubber heat sheets.

Figure 3.3: 316 Stainless steel cartridge immersion heater.

In order to control the solution temperature, a temperature control circuit was used. The power was provided by a power input, with a temperature controller and a thermocouple connected in a feedback loop to maintain the temperature at 80 ± 1 °C. The temperature controlling system is shown in Figure 3.4.

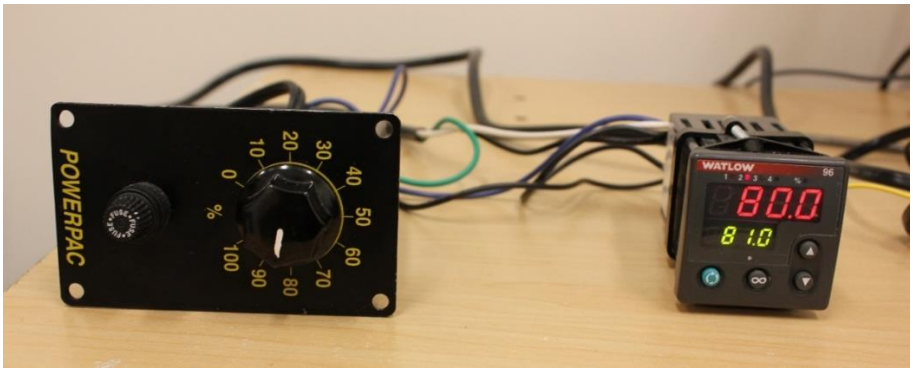

Figure 3.4: Power input and temperature controller.

3.2.2 Test Solution and Environmental Chamber

Initially, a 0.9% saline solution was selected as a test fluid to mimic the human body fluids. However, due to the high test temperature and lengthy duration of the performed tests, the 0.9% saline solution pH was not stable. Therefore, phosphate buffered saline (PBS) with a pH of 7.4 ± 0.1 was selected as the alternative test fluid. The advantage of using a buffered solution was to maintain a constant pH of the solution preventing it from becoming acidic or alkaline, thereby affecting the corrosion rate of the tests. Moreover, PBS has a pH similar to the blood pH of 7.35 - 7.45 [50].

Because the test solution was heated to 80 °C, the evaporation rate was expected to be high and fluid replenishing would have been required to keep the neck-stem interface and the heaters submersed in the test solution. However, there was the concern of increasing the salt concentration if the solution was replenished with PBS. In order to confirm the stability of the PBS if it was replenished with distilled water instead, two side experiments were conducted. In each experiment, the solution tank that only contained the heaters and PBS (no THR components) was set at 80 °C for five days (the duration of a fatigue test), and replenished with roughly 80 - 100 mL of one of the considered fluids every day. Samples were taken daily

to measure the pH. Results showed that the pH of the bath solution remained within the range of 7.4 ± 0.1 in both experiments (Appendix B). Therefore, distilled water was selected as the replenishing fluid to avoid increasing unwanted salt concentration in the test solution. The PBS solution used in this study consisted of the substances shown in Table 3.1. The provided formula is to prepare 5.0 L of PBS. The PBS was prepared with an Orion^{TM} Ag/AgCl combination pH semi-micro electrode (Thermo Scientific, Waltham, MA, USA) and SympHony^{TM} electrochemistry meter (model SB21, VWR, Mississauga, ON, Canada). A detailed procedure for preparing the PBS is included in Appendix C.

Table 3.1: The formulation to prepare 5.0 L of phosphate buffered saline [51].

Substance	Formula	Molecular weight (mM)	Mass (g)
Potassium Phosphate Monobasic	KH_2PO_4	1.1	0.72
Sodium Chloride	NaCl	154.0	45.0
Sodium Phosphate Dibasic	Na_2HPO_4	5.6	3.98
Millipore Water	5.0 (L)		

For the actual mechanical tests, in order to monitor the PBS solution pH, samples were collected at the start of the test, and then every other day until the end of the test. The pH of all the samples collected during the mechanical tests were then measured with the same pH electrode and pH meter that were used to prepare the PBS.

To minimize the heat loss from the fixtures to the surroundings, the bath and the stem holder were insulated with polyurethane sleeves. Furthermore, a low-density polyethylene (LDPE) sheet was placed on top of the tank, while a waterproof adhesive sealer was wrapped around it to form an environmental test chamber, as shown in Figure 3.5. The environmental test chamber also sealed the load transfer adaptor and the heaters. The use of the chamber

minimized the evaporation rate to 80 - 100 mL or less per 24 hours, which was a significant improvement for the testing and eliminated the use of a drip system to compensate for the fluid loss. Nevertheless, distilled water was added manually as required to maintain the fluid level at approximately 1.6 L. To ensure stable testing, the fixtures were clamped on the load frame, as seen in Figure 3.5.

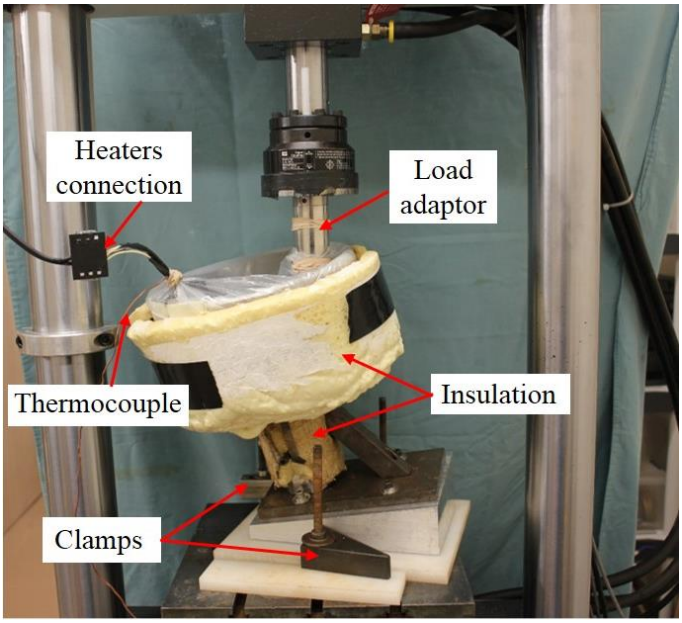

Figure 3.5: Environmental test chamber used for mechanical tests.

3.2.3 Testing Setup

The testing was conducted in accordance with the ISO 7206-4-2002 Standard for implant alignment. The prescribed offset angles α and β, and the embedding depth (D_a) of the stem are summarized in Figure 3.6. The values of these parameters depend on the distance from the centre of the femoral head to the distal tip of the stem of an assembled implant, which is denoted in Figure 3.6 as axis CT. Once the length CT was measured, the values of the offset angles and the embedding medium depth were determined as shown in Table 3.2.

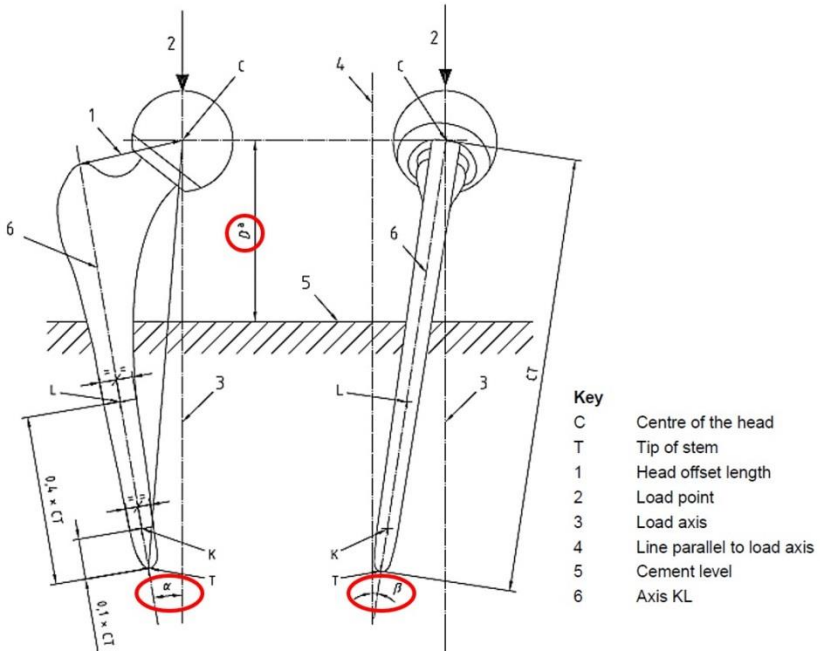

Figure 3.6: Test setup for a straight implant (no version) under mechanical tests [52].

Table 3.2: Implant mounting and alignment parameters for mechanical tests. α and β: offset angles of the tested implants; CT: distance from the centre of the femoral head to the distal tip of the stem; D_a: embedding depth of the femoral stem.

	α ± 1 (°)	**β ± 1 (°)**	**CT (mm)**	**D_a ± 2 (mm)**
ISO 7206-4-2002 Requirements [52]	10	9	Up to and including 200	0.4 CT
	0	4	More than 200	CT - 100
Present study	10 ± 1	9 ± 1	185	74 ± 2

Ideally, bone cement (PMMA) would be used for *in vitro* testing to closely replicate the boundary conditions of *in vivo* THR. However, the bone cement could have softened due to the elevated test temperature of 80 °C, which could induce implant loosening and migration under loading, especially when the implant is subjected to high fatigue loads. Therefore, a steel-reinforced epoxy (J-B WELD, Sulphur Springs, TX, USA) was selected for the embedding medium of the stems. This epoxy can sustain a temperature up to 315 °C according to the manufacturer guidelines.

The first revision of the utilized test fixture was adopted from the previous study by Nganbe et al. [53], as shown in Figure 3.7. The existing fixture featured a tank that was used as a solution bath so that the neck-stem interface could be submerged in the test solution. The tank was attached to a specimen holder (potting cup) that was used to pot and fix the stem in PMMA. The brace provided support to the fixture against bending when subjected to the test loads. The adaptor was used as a base for the fixture, while the adaptor table fixed the fixture onto the testing machine.

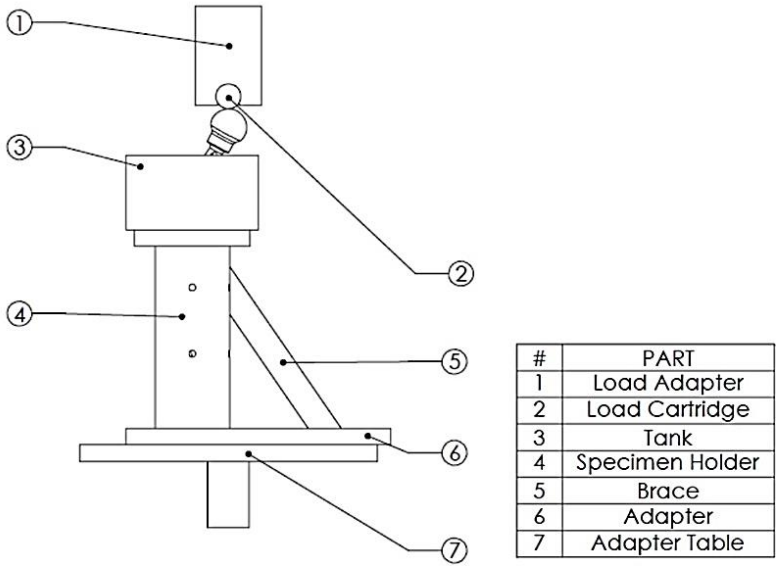

Figure 3.7: Previous mechanical testing fixture [54].

However, due to changes in the testing parameters between the previous and the current studies, such as the use of a more corrosive environment, most of the fixture parts were modified or redesigned to sustain the current testing parameters.

First, the tank was redesigned to accommodate for the heaters and to allow for the submersion of the neck-stem interface with a solution volume of approximately 1.6 L. The tank, along with the fasteners and washers that were used to attach the tank to the specimen

holder, were made of 316 stainless steel. Originally, the tank had a concave bottom that did not allow it to fit on the specimen holder. Therefore, the bottom of the tank was bored out and a 316 stainless steel disk was welded and flattened to allow for firm attachment to the specimen holder. Moreover, corrosion resistant compressible polytetrafluoroethylene (PTFE) gaskets were used to minimize the solution leakage from the tank. In order to sustain a uniform pressure on the gasket inside the tank, a 316 stainless steel O-ring was utilized, as seen in Figure 3.8.

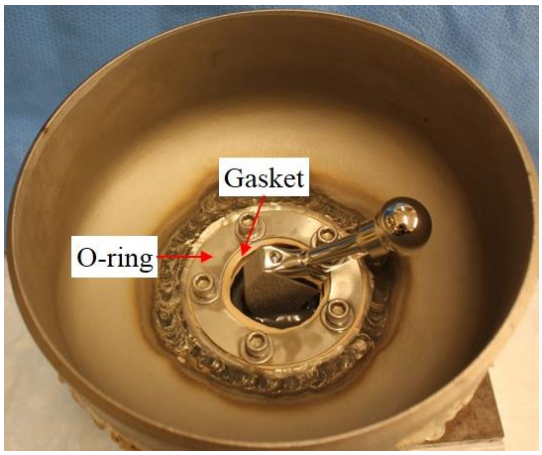

Figure 3.8: An overview of the tank with an assembled implant.

Second, as the existing aluminum specimen holders were severely corroded after being used for a few tests, new parts of the same design were machined of 316 stainless steel to withstand the corrosive test environment. Figure 3.9 displays the old and new specimen holders after the mechanical tests.

Figure 3.9: The effect of the corrosive testing environment at the top of the inner edge of the aluminum specimen holder.

Third, the previous load transfer adaptor was designed from two components (steel adaptor and stainless steel cartridge). Due to this multi-component design and materials selection, it was noticed during pilot tests that the load adaptor was not stable at high test loads, and corrosion products were forming on the components even though the load adaptor was coated with synthetic rubber in an effort to protect it against corrosion. Therefore, a one-piece load transfer adaptor made of 316 stainless steel was designed and machined to protect it from corrosion as it was exposed to the corrosive steam of the test solution. The previous and redesigned load adaptors are shown in Figure 3.10.

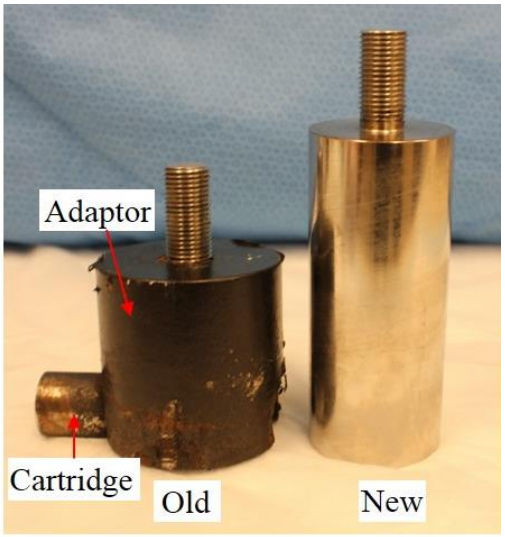

Figure 3.10: Load transfer adaptors.

Fourth, a new aluminum block with 9°/10° offset surface angles was machined and used as an adaptor surface for the fixture. The addition of the offset block to the test fixture reduced the potential for errors that could arise from manually aligning each specimen for the mechanical tests. The machined block is shown in Figure 3.11.

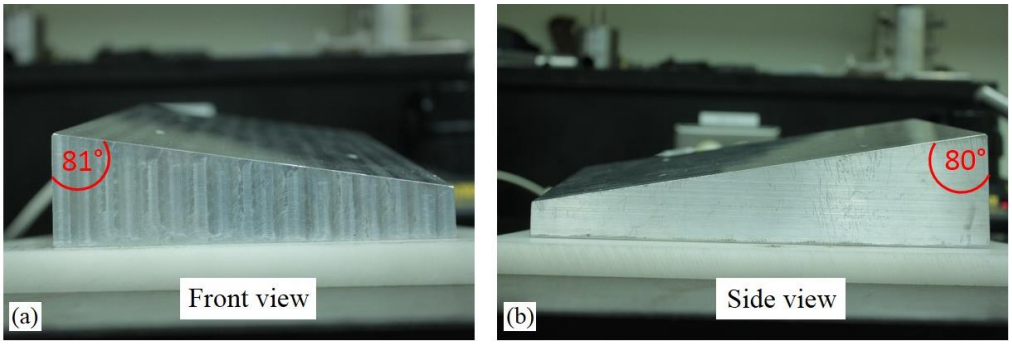

Figure 3.11: A 9°/10° offset angles block for implant orientation: (a) Front view; (b) Side view.

Lastly, the adaptor table was replaced with a polyvinylidene fluoride (PVDF) polymer base, with a melting point of 170 °C [55], in order to thermally and chemically decouple the fixture from the load frame. The PVDF base was also used as the drop tower base (section

3.2.4). An overview of the modified mechanical testing fixture is shown in Figure 3.12. The mechanical drawings of the new fixture parts are included in Appendix D.

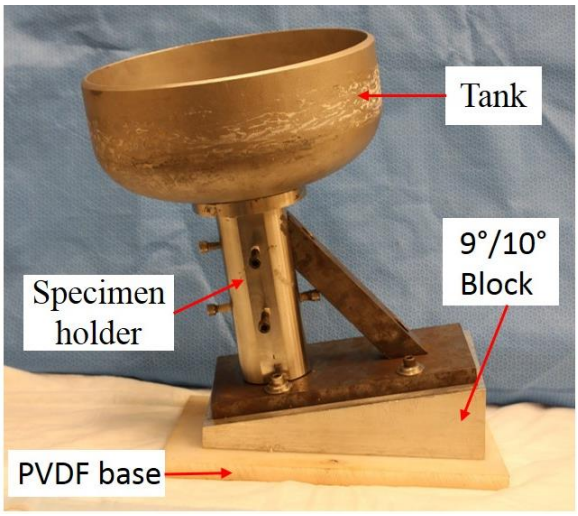

Figure 3.12: New fixture components.

3.2.4 Implant Assembly Method

Hand and impact assembly methods were investigated. The hand assembly represented the worst case scenario since no significant force was applied on the modular components to maximize the taper interlock. Hand assembly of THR can occur *in vivo* when the incision size is small, preventing the surgeon to efficiently use a surgical hammer to assemble the modular parts. In the hand assembly process, the neck was hand-pressed into the stem junction, followed by hand-pressing of the femoral head onto the modular neck.

The impact assembly technique was developed to represent the assembly method corresponding to the hammer blows applied by the surgeon during assembling, according to manufacturer's recommendations. To perform the impact assembly, a custom drop tower was designed and constructed to standardize the impact assembly force, as suggested by the ASTM F2009 Standard.

The challenge with the drop tower design was to design a dropping mechanism that allowed dropping a polymeric impactor in a controlled and reproducible manner. One of the attempted techniques was to carry the polymeric impactor by strings as shown in Figure 3.13a. However, the design proved to be ineffective due to the completely uncontrolled motion of the impactor upon release. Therefore, to stabilize the dropping procedure (i.e., impactor release), the carrying strings were replaced with an anodized aluminum shaft to form a hammer, which was constrained and guided by a linear ball bearing (Figure 3.13b). This modification ensured controlled, repeatable and stable dropping of the impactor during implant assembly.

The mass of the drop tower hammer (including the polymeric impactor) was 1.4 kg, and the impactor was released from a height of 20.32 cm (8 in). The mass and the height parameters were adopted from a previous study on Morse tapers strength in THR by Pennock et al. [56]. In their study, the authors showed that applying multiple blows of the same force slightly increased the taper interlock strength, and the first two blows contributed the most to the overall strength of the taper interlock [56]. Therefore, the impact assembly process in the present study was carried out by applying two blows on the modular neck to assemble the neck-stem interface, followed by two other blows on the femoral head to assemble the head-neck interface. In this study, all the hand and impact assemblies were performed in a dry environment and ambient temperature. The mechanical drawings of the drop tower parts are found in Appendix D.

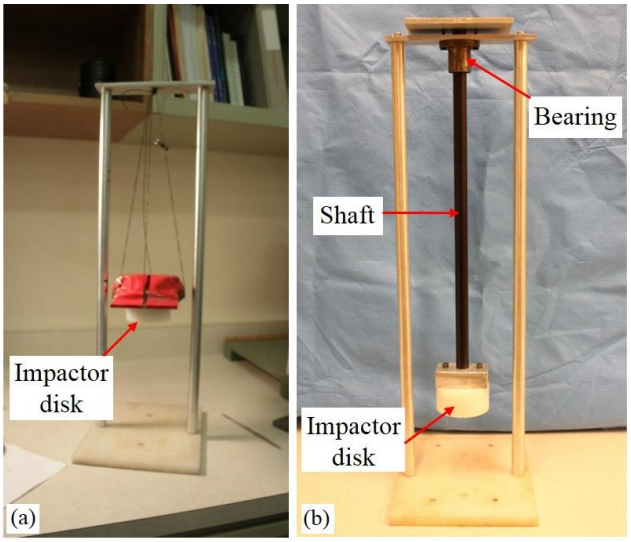

Figure 3.13: Custom designs of the drop tower for impact assembly: (a) Early design with unconstrained free fall; (b) Final design with linear bearing allowing for controlled and reproducible impaction.

3.3 Fatigue and Corrosion Tests Protocol

The tests were divided into two main categories: fatigue and corrosion, as summarized in Figure 3.14. Within each category, the tests were sub-divided into four groups to allow for direct comparison in terms of neck material and assembly method, each with a sample size of three (N = 3). For all tests, a cyclic loading frequency of 10 Hz was used based on ISO 7206-4-2002 recommended cyclic loading frequency between 4 - 30 Hz for metallic specimens. Twelve (12) hours of loading and 12 hours of resting cycles were used to increase the effects of corrosion damage on the specimens and to better simulate the *in vivo* loading/resting periods of the implant in the patient's body.

Fatigue tests consisted of two stages: the settling stage and the endurance performance stage. For the settling stage, the implant was subjected to a maximum compression load of 2.3 kN for 150,000 cycles at 10 Hz. This stage simulates the lower *in vivo* loads during

rehabilitation in the first few months following a THR surgery. For the endurance performance (fatigue life) stage, an initial maximum compressive load of 6.0 kN for 1 million cycles was selected for the pilot study. The 6.0 kN corresponded to 45% of the Ti6Al4V modular neck ultimate compressive strength that had been determined by quasi-static loading by Nganbe et al. [57]. However, no signs of plastic deformation or crack initiation were observed. Therefore, in order to achieve fracture within a reasonable amount of time, the applied load was increased from 6.0 to 8.0 kN. However, the increased loads caused severe vibrations in the loading frame and fixtures, even when the cyclic frequency was lowered from 10 to 5 Hz. As a final adjustment, a maximum compression load of 7.0 kN at 10 Hz was selected with an increased number of cycles to 1.3 million cycles, which corresponded to an additional 12/12 hours loading/resting cycle.

Unlike fatigue tests, the aim of corrosion tests was primarily to study the effects of wear and corrosion on the neck-stem taper interface. Therefore, corrosion tests were conducted with a lower cyclic loading, but for more cycles and a longer test duration than the fatigue tests. For corrosion tests, the maximum compression load was 2.3 kN for a test duration of 5.0 million cycles. The load magnitude and number of cycles were adopted from ISO 7206-8-1995 and ASTM 2068 Standards.

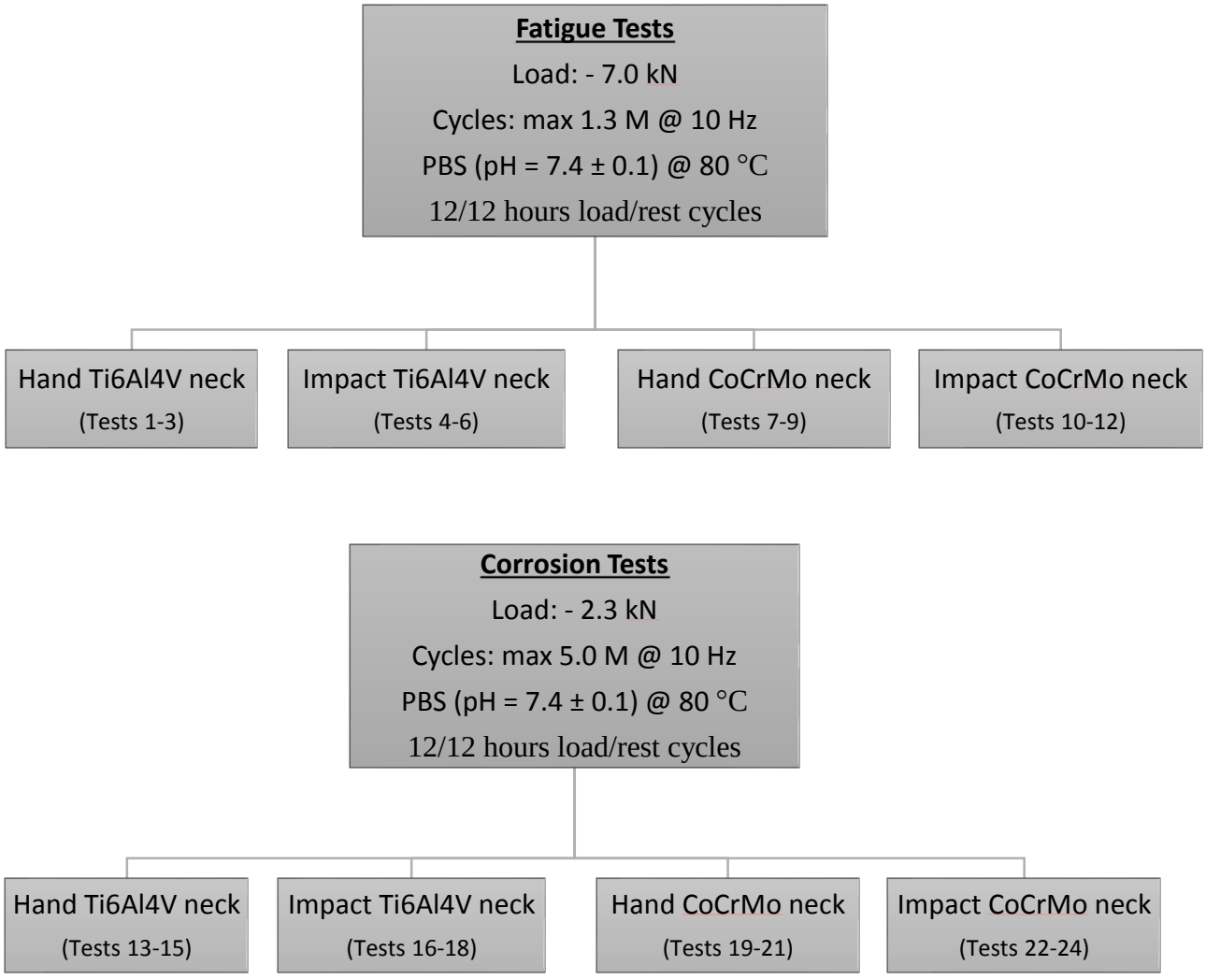

Figure 3.14: Fatigue and corrosion tests protocol.

The cyclic mechanical loading was applied using a MTS 858 Mini Bionix® II testing machine (MTS Systems Corporation, Eden Prairie, MN, USA) shown in Figure 3.15. In accordance with ISO 7206-4-2002, a test is completed when one of the following events occurs: (1) the head deflection reaches 5.0 mm; (2) the specimen fractures; or (3) the total number of cycles is reached (test run-out).

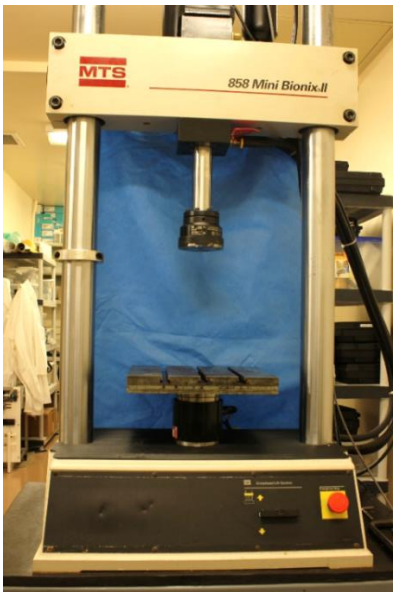

Figure 3.15: MTS 858 Mini Bionix® II testing machine.

3.4 Modular Neck Distraction and Post-Test Assessments

Neck distraction experiment was performed following both fatigue and corrosion tests. This allowed measuring the distraction force required to separate the neck from the stem. A clinical standard distraction tool (MicroPort Orthopedics Inc., formerly Wright Medical Technology Inc., Arlington, TN, USA) and a newly designed adaptor were used for this purpose. The adaptor allowed attaching the clinical distraction tool to the load frame. The system allowed achieving a firmer grip on the neck during distraction and minimizing slipping. An angled block was used to position the sample and align the neck axis parallel to the tensile distraction force (Figure 3.16a). The existing and current distraction tools are seen in Figure 3.16b. The distraction process was performed using the same load frame used for mechanical tests, as shown in Figure 3.17. The mechanical drawing of the distraction tool adaptor is found in Appendix D.

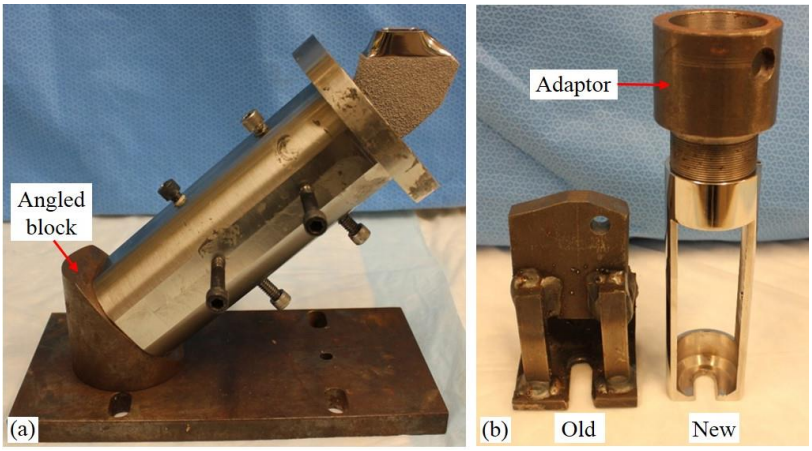

Figure 3.16: Neck distraction setup fixtures**:** (a) An angled block for implant positioning during neck distraction; (b) Distraction tools used to separate the modular neck from the stem.

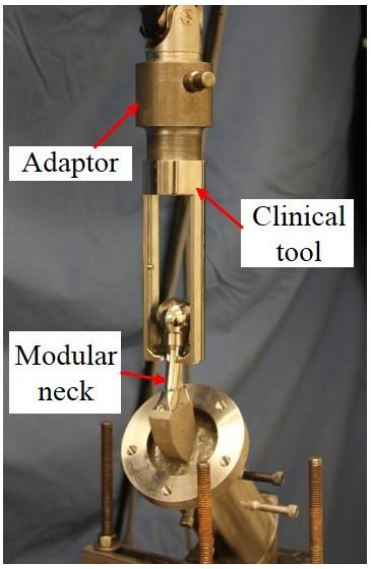

Figure 3.17: Neck distraction process.

Upon neck distraction, the trapped fluid inside the stem pocket was collected using a pipette to measure the fluid volume in order to determine the effects of the assembly method and the neck material on the sealing of the neck-stem interface. Moreover, due to the small volumes of the collected samples (an electrode could not be used), the pocket fluid pH was measured using MColorpHast^{TM} pH-indicator strips (EMD Millipore, Billerica, MA, USA).

The tested necks were also cleaned in an ultrasonic bath (same as before testing cleaning procedure, Appendix A) to remove any residue resulting from mechanical tests and to better expose the taper surfaces for surface analysis, without disturbing or removing the wear-corrosion layers.

Fretting and corrosion were assessed visually using a stereo microscope (Ancansco, Toronto, ON, Canada) and Goldberg scores [58], as shown in Table 3.3. The Goldberg score system is a subjective method that relies on the examiner perspective when assessing the fretting and corrosion damage of modular tapers. Therefore, different examiners can have different results when evaluating the same surfaces. Nevertheless, the method is still widely used and accepted in the orthopedics field since there is no standardized method to evaluate the Morse tapers damage.

Table 3.3: Criteria for fretting and corrosion scores [58].

Severity of fretting and corrosion	Score	Criteria
None	1	• No visible corrosion • No visible signs of fretting
Mild	2	• < 30% of taper surface discolored or dull • Single band or bands of fretting scars involving three or fewer machining lines on the taper surface
Moderate	3	• > 30% of taper surface discolored or dull, or < 10% of taper surface containing black debris, pits, or etch marks • Several bands of fretting scars or single band involving more than three machining lines
Severe	4	• > 10% of taper surface containing black debris, pits, or etch marks • Several bands of fretting scars involving several adjacent machining lines, or flattened areas with nearby fretting scars

For a single neck, the four individual taper surfaces (i.e., anterior, posterior, medial, and lateral), shown in Figure 3.18, were evaluated separately, and then the most representative Goldberg score was selected as the overall score. The conversion of the individual scores into

a single overall score was adopted from Goldberg et al. [58]. This was done to provide a single score for each neck, in terms of fretting damage and corrosion damage, to allow for direct comparison between the neck material, the assembly method, and test type (i.e., fatigue and corrosion tests).

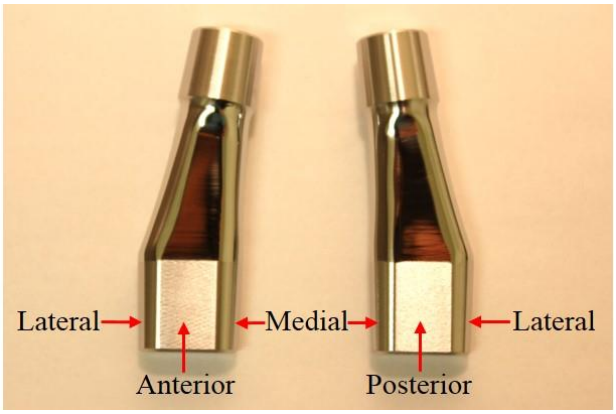

Figure 3.18: View of the four taper surfaces.

3.5 Statistical Analysis

Statistical tests are not presented due to the small sample size. For the purpose of this thesis, it was decided to present the data as individual values and discuss the results as trends.

4 Results

In total, 12 fatigue and 12 corrosion tests were conducted in the study. Results on the pH of the bath and stem pocket solutions, fatigue life, corrosion behaviour, modular necks surface damages, and distraction forces are summarized in the following sections.

4.1 Temperature Stability and pH Change During Mechanical Tests

The stability of the heating system and the solution temperature were monitored and controlled during the tests. The solution temperature increased gradually from room temperature to the fixed test temperature of 80 ± 1 ºC prior to mechanical cycling. The temperature then remained stable during the entire test duration for both fatigue and corrosion tests. The temperature profile of the solution adjacent to the neck-stem interface can be seen in Figure 4.1.

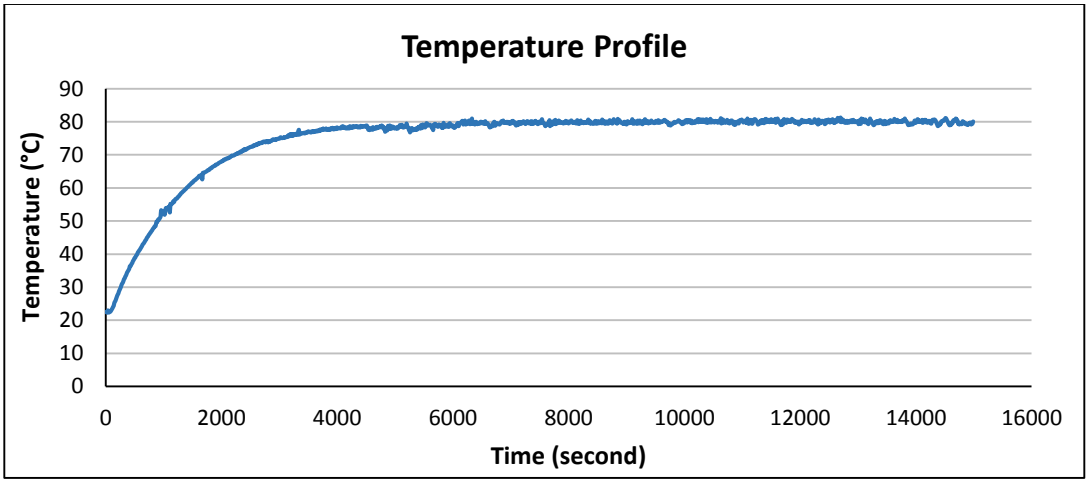

Figure 4.1: Temperature profile around the neck-stem interface area.

For the fatigue tests, the bath solution pH increased slightly from day 1 to day 5 but only by a maximum of 0.2 units in all groups. This slight change in solution pH likely did not substantially affect the results of the fatigue tests.

For the corrosion tests, the solution pH continued to slowly increase as the tests progressed, especially for the hand-assembled implants (up to a maximum pH of 8) after 9 to 11 days of testing (Figure 4.2A and C). One of the impact-assembled Ti6Al4V implants (Test 17) showed a stronger increase (up to 9.1 at day 13), but this increase was likely due to the failure of a heater at the wire junction during the test. The results of pH change over time for the corrosion tests are summarized in Figure 4.2. Detailed pH measurements of the test solution from all the tests (fatigue and corrosion) are provided in Appendix E.

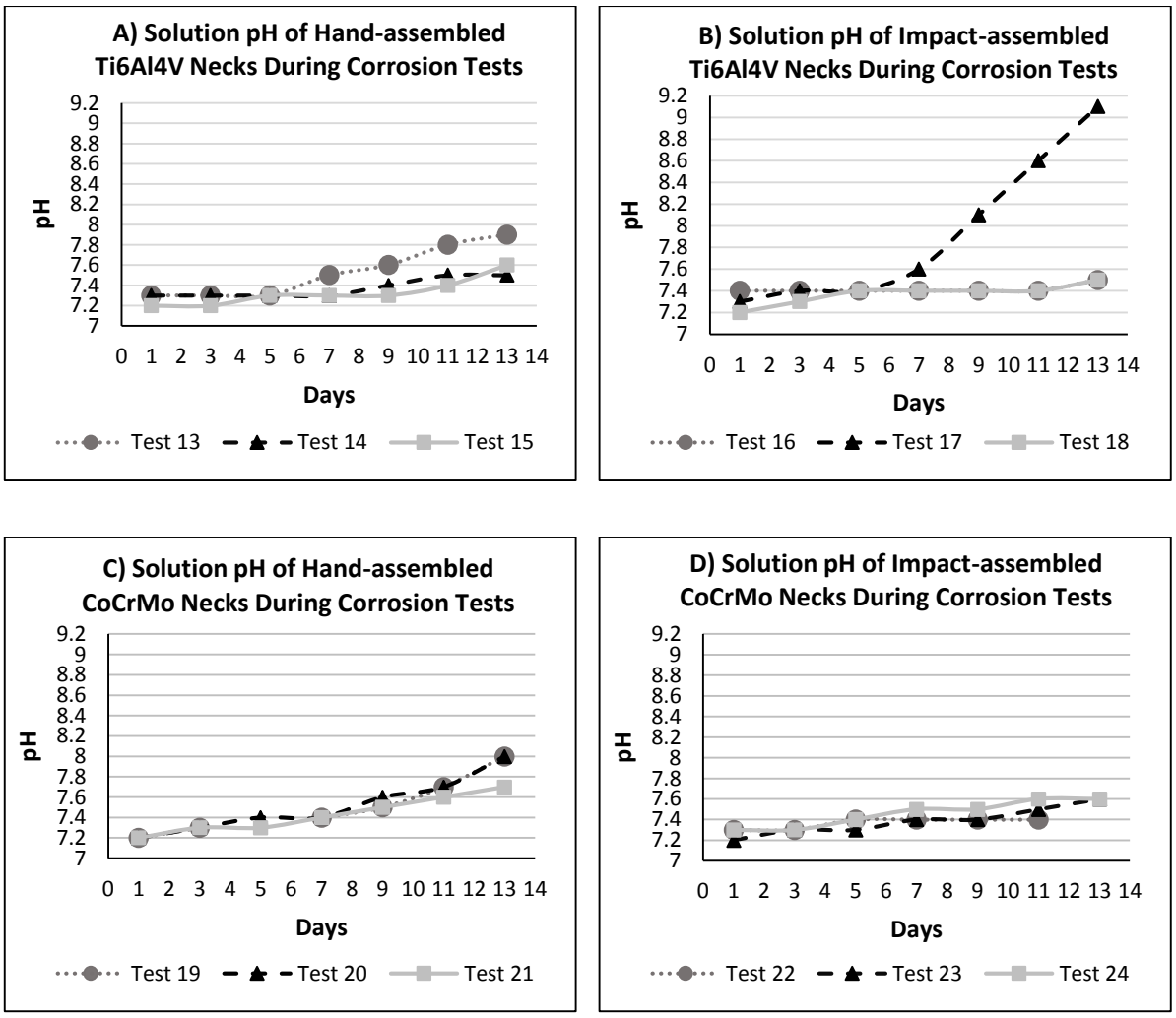

Figure 4.2: pH change of the test solution during corrosion tests of : A) Hand-assembled Ti6Al4V necks; B) Impact-assembled Ti6Al4V necks; C) Hand-assembled CoCrMo necks; D) Impact-assembled CoCrMo necks. Note: the solution pH for day 5 of test 19 and day 13 of test 22 were not measured.

Furthermore, upon neck distraction, the trapped stem pocket fluid volumes were measured and tested for pH. In general, stems tested with hand-assembled CoCrMo necks had more fluid accumulation in the stem pocket compared to hand-assembled Ti6Al4V necks, while impact-assembled Ti6Al4V and CoCrMo necks had relatively similar fluid accumulation volume. Moreover, the impact assembly did not prevent the solution fluid from

getting into the assembled neck-stem junction. Finally, the fluid volume increased with increasing duration of testing. Therefore, more fluid accumulation was observed with the corrosion tests than with the fatigue tests. The measured pocket fluid volumes for fatigue and corrosion tests are shown in Figure 4.3. Detailed stem pocket volumes of all the tests are provided in Appendix F.

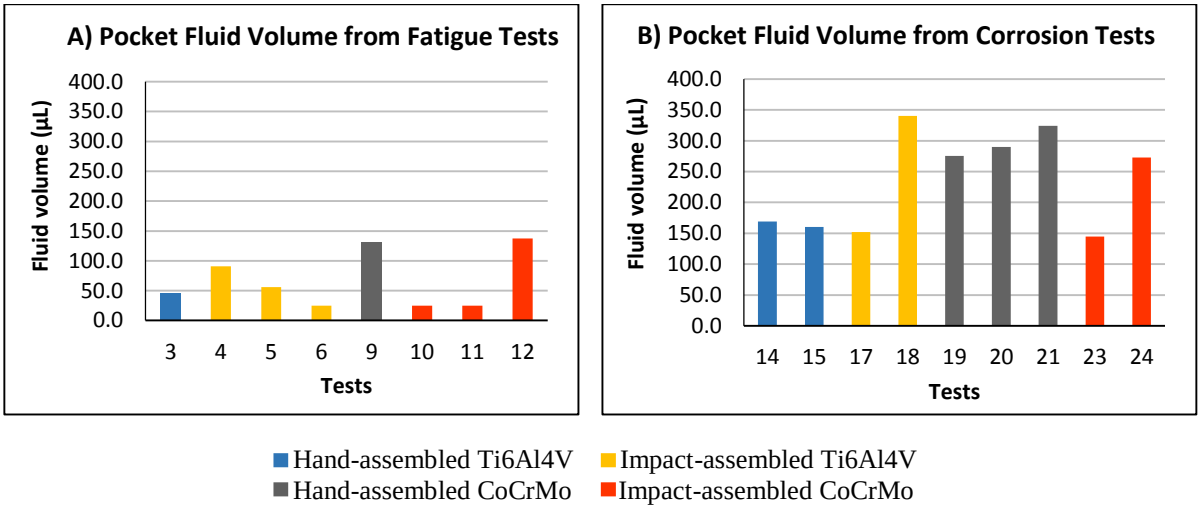

Figure 4.3: Measured stem pocket fluid volume from: A) Fatigue tests; B) Corrosion tests. Note: data for fatigue tests (1, 2, 7, and 8), and corrosion tests (13, 16 and 22) were not measured.

Moreover, overall, corrosion tests resulted in a slightly higher pocket pH than fatigue tests. Ti6Al4V and CoCrMo necks had relatively similar pocket pH except for some tests conducted with Ti6Al4V necks where the pocket fluid pH became extremely acidic, with values between 0.0 and 2.0, while CoCrMo necks resulted in a more consistent pocket fluid pH within the CoCrMo groups.

Of note is that due to the small pocket fluid volumes, the pocket pH was estimated by multiple trials of very small amount (7 µL each). This made it difficult to determine the exact

pH values and therefore, the pH was estimated as a range. The estimated pocket fluid pH for fatigue and corrosion tests are shown in Tables 4.1 and 4.2, respectively.

Table 4.1: Estimated stem pocket fluid pH from fatigue tests (expressed as a range). Note: data for tests 1, 2, 7, and 8 are not available.

Test number	Material	Assembly method	Pocket fluid pH
3	Ti6Al4V	Hand	0.0 - 2.0
4		Impact	0.0 - 2.0
5			6.0 - 7.0
6			5.0 - 5.8
9	CoCrMo	Hand	5.0 - 7.0
10		Impact	5.0 - 5.8
11			5.0 - 7.0
12			5.0 - 7.0

Table 4.2: Estimated stem pocket fluid pH from corrosion tests (expressed as a range). Note: data for tests 13, 16 and 22 are not available.

Test number	Material	Assembly method	Pocket fluid pH
14	Ti6Al4V	Hand	5.0 - 7.0
15			0.0 - 2.0
17		Impact	0.0 - 2.0
18			7.0 - 8.0
19	CoCrMo	Hand	6.0 - 8.0
20			6.0 - 8.0
21			7.0 - 8.0
23		Impact	7.0
24			6.5 - 7.1

4.2 Fatigue Life and Corrosion Behaviour

Of the three tested hand-assembled Ti6Al4V necks, two fractured completely after 1,102,837 and 1,019,282 cycles, respectively, and one exhibited a crack during the prescribed 1.3 million fatigue cycles. The crack location was identical for the three failed necks. It initiated at the distal lateral surface of the modular neck taper, and then propagated diagonally until final fracture at the proximal medial surface of the taper, which was in contact with the stem pocket edge. The fracture location that resulted along the modular neck taper was

consistent with the reported *in vivo* fractures. On the other hand, none of the impact-assembled Ti6Al4V, and none of the hand- and impact-assembled CoCrMo necks showed fatigue damage. The failed necks are shown in Figure 4.4, and the fatigue test results are summarized in Figure 4.5.

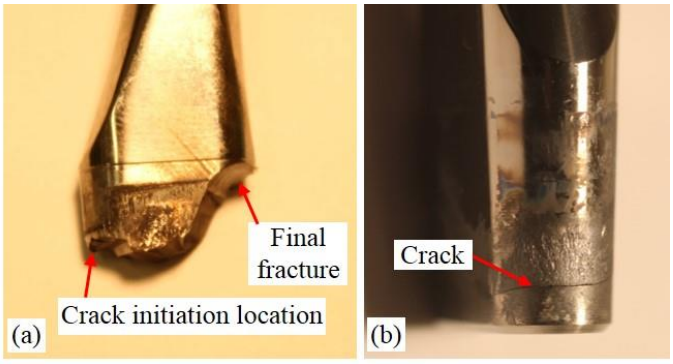

Figure 4.4: Hand-assembled Ti6Al4V necks after fatigue tests under a 7.0 kN maximum compressive load at 10 Hz in PBS at 80 ºC: (a) Complete fracture; (b) Crack initiation.

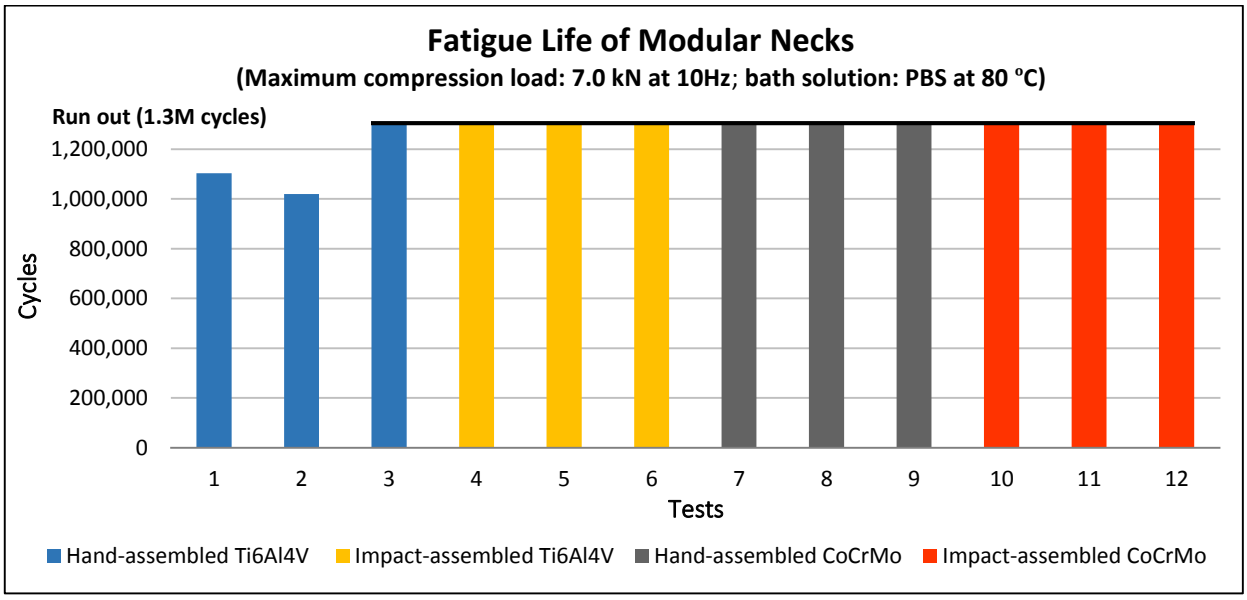

Figure 4.5: *In vitro* fatigue life of Ti6Al4V and CoCrMo long modular necks.

No signs of crack initiation or plastic deformation were observed on the necks following corrosion tests. However, signs of wear-corrosion were observed on the taper surface of the tested Ti6Al4V and CoCrMo necks. Furthermore, some of the necks tested for fatigue (i.e., for a shorter duration but higher load compared to corrosion tests), showed signs of more advanced wear-corrosion. The Ti6Al4V stems showed more advanced corrosion when tested with the CoCrMo necks, as depicted by the presence of black debris especially at the medial and lateral surfaces, which corresponded to the locations of highest local compression loading on the neck taper, as can be seen in Figure 4.6. The overall summary of the fatigue and corrosion tests is provided in Appendix F.

Figure 4.6: Corrosion (black debris) on the medial surface of a Ti6Al4V stem following a corrosion test with a hand-assembled CoCrMo neck.

4.3 Distraction Force Analysis

With regards to the effect of neck material, results showed that the impact-assembled Ti6Al4V necks generally required a higher distraction force than the impact-assembled CoCrMo necks in fatigue and corrosion tests. Overall, the distraction force did not seem to be different between the two alloys when the necks were hand-assembled and tested for corrosion.

No comparison could be made between the hand-assembled necks tested for fatigue due to the fracture of two Ti6Al4V necks.

With regards to the effect of the assembly technique, results showed that, overall, the impact-assembled necks required a higher distraction force than the hand-assembled necks for the same test type (i.e., fatigue or corrosion tests) and neck material.

Furthermore, the distraction forces between the fatigue and corrosion tests were overall similar for the same neck material and assembly method, with possibly the exception of the impact-assembled CoCrMo necks for which the higher load applied during fatigue tests (compared to corrosion tests) may have led to a slight increase in the distraction force. A higher number of samples would be required to verify this trend. The neck distraction forces of all the fatigue and corrosion tests are summarized in Figure 4.7, except for Tests 1 and 2, for which the necks were completely fractured.

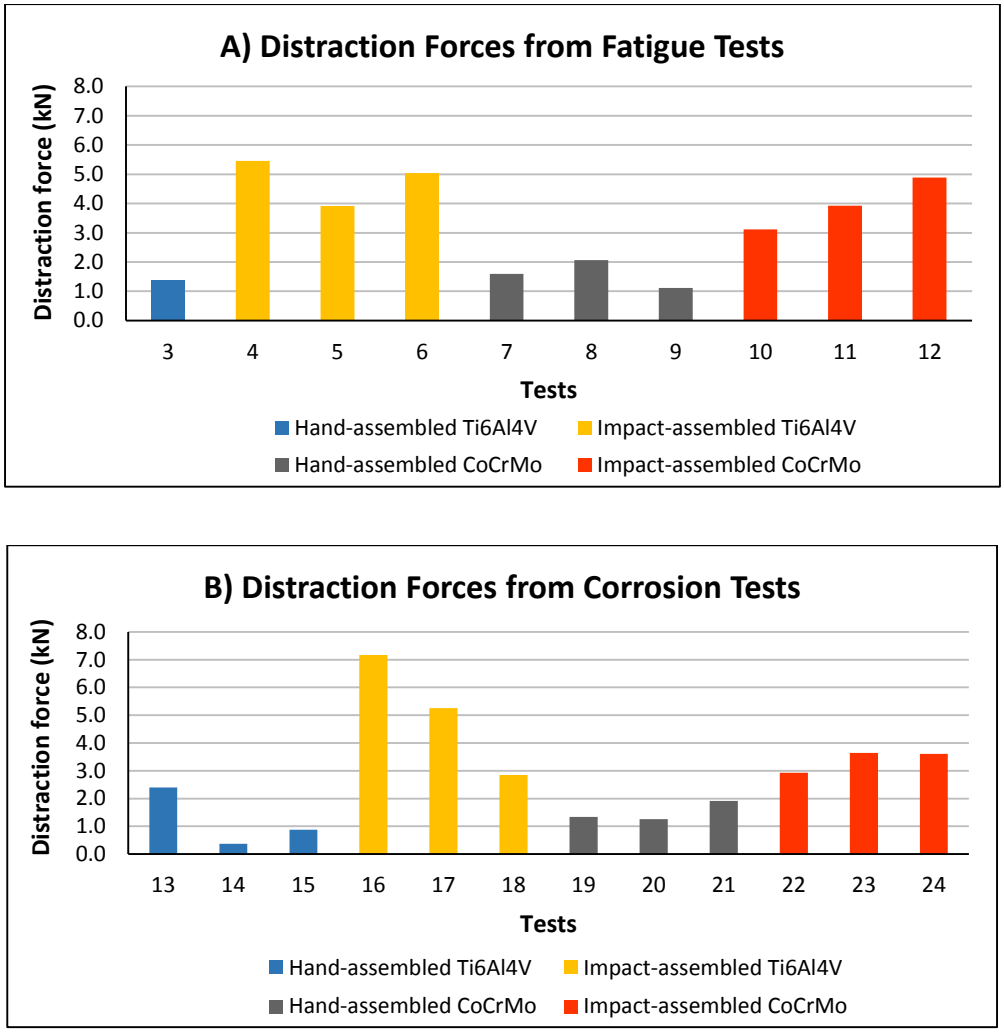

Figure 4.7: Distraction forces of the modular necks from: A) Fatigue tests; B) Corrosion tests. Note: the distraction force was measured for only one hand-assembled Ti6Al4V neck tested for fatigue due to the fracture of the other two necks.

Examples of individual neck distraction tests curves are shown in Figures 4.8 and 4.9 for Ti6Al4V and CoCrMo necks, respectively. As depicted on these figures, the neck distraction tests started with the testing machine, through the distraction tool, aligning and establishing a firm grip on the neck, which took place at near zero load. Thereafter, the distraction force increased until reaching the maximum required force (curve peak point) to pull out the neck and then dropped back to zero, confirming the neck separation from the stem.

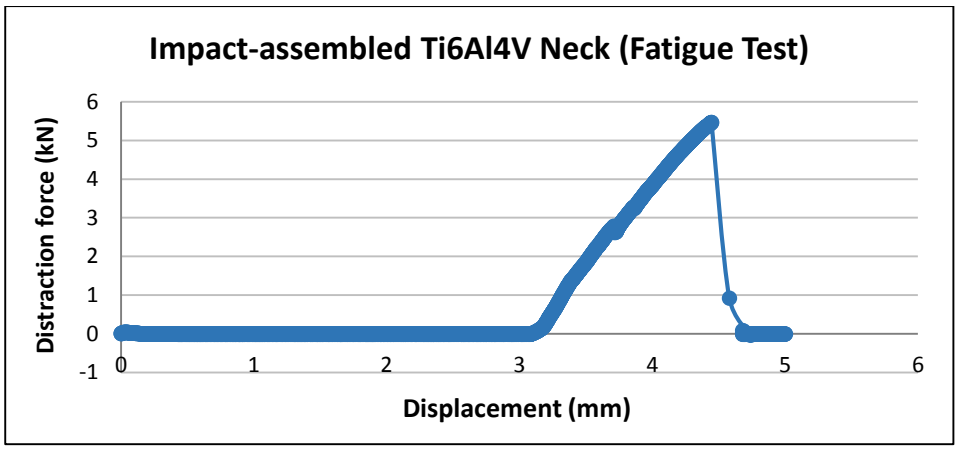

Figure 4.8: Distraction force plot of an impact-assembled Ti6Al4V neck tested for fatigue.

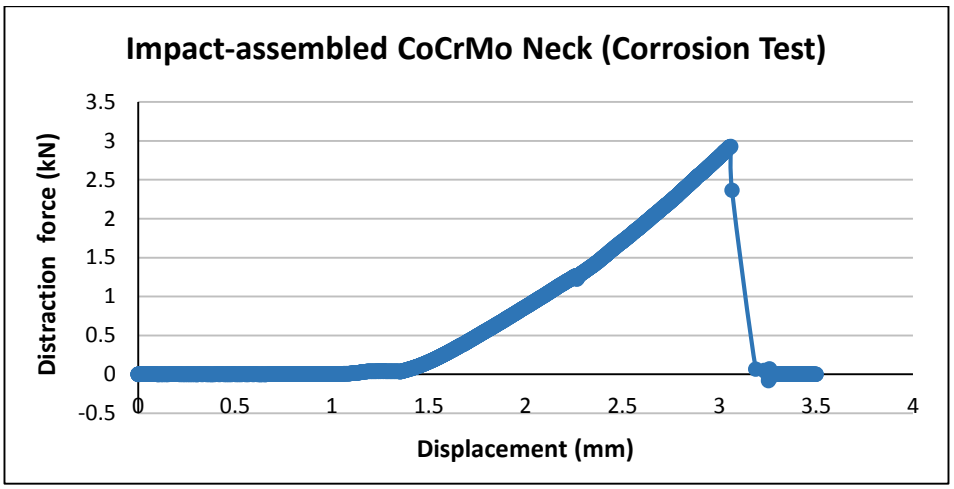

Figure 4.9: Distraction force plot of an impact-assembled CoCrMo neck tested for corrosion.

4.4 Surface Damage of Modular Necks

Different types and levels of wear, fretting and corrosion damage were observed on all tested necks. Overall, wear and corrosion damage occurred simultaneously during fatigue and corrosion tests. Flattened areas and worn-out machining lines on the taper surfaces were observed on some of the necks due to wear and fretting with the stem pocket. Moreover, dull areas and the formation of corrosion products (black debris) on the taper surface were observed as a result of corrosion.

To assess the fretting and corrosion damage, the tested necks were first evaluated based on the observed fretting and corrosion damage on each surface of each neck. The assigned Goldberg fretting and corrosion scores (1: None, 2: Mild, 3: Moderate, and 4: Severe) for each of the neck taper surfaces for all the necks are shown in Figure 4.10. For simplicity and for the purpose of the present study, the fretting and corrosion Goldberg scores were compared and displayed based on the neck material and assembly method, independent from the test type (i.e., fatigue and corrosion tests were grouped).

From the assembly method point of view, the impact-assembled Ti6Al4V necks (Figure 4.10A) had less fretting damage on the anterior and posterior surfaces and more fretting damage on the medial and lateral surfaces than the hand-assembled Ti6Al4V necks. On the other hand, the impact-assembled CoCrMo necks (Figure 4.10B) had less fretting damage than the hand-assembled CoCrMo necks on all four surfaces. Based on the corrosion scores, none of the hand- and impact-assembled Ti6Al4V (Figure 4.10C) suffered severe corrosion damage (score 4), and the observed corrosion was relatively similar for the two assembly methods. On the other hand, the impact-assembled CoCrMo necks (Figure 4.10D) had less severe corrosion on the anterior and medial surfaces, while the posterior and lateral surfaces exhibited similar and increased corrosion damage, respectively, compared to hand-assembled CoCrMo necks.

Overall, the Ti6Al4V necks suffered more severe fretting than CoCrMo necks, while CoCrMo necks resulted in more advanced corrosion damage than Ti6Al4V necks. Overall, increased fretting and corrosion damage were mostly observed on the medial, lateral and anterior surfaces, while the posterior surface had the least damage, as seen in Figure 4.10E.

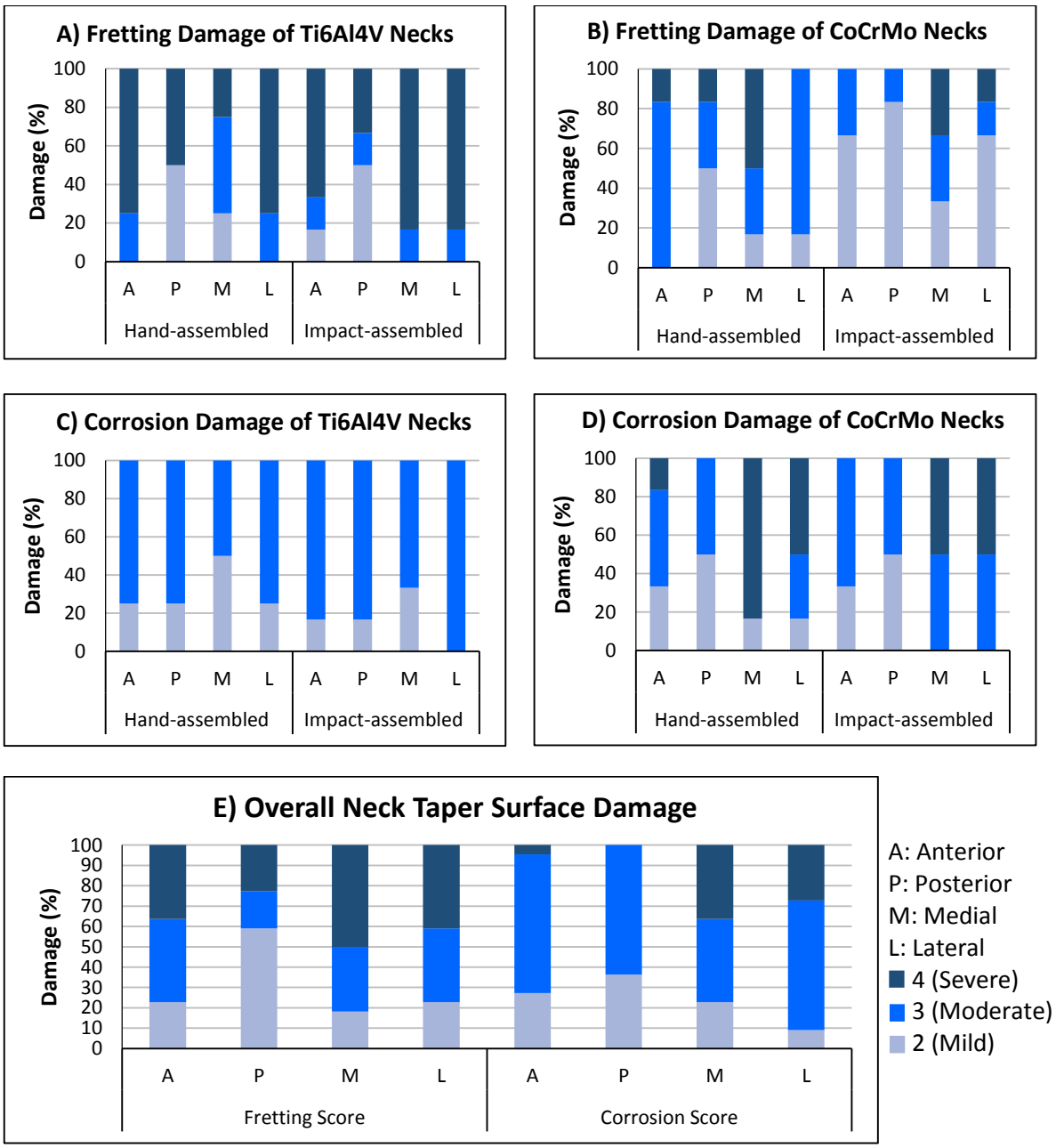

Figure 4.10: Goldberg scores of the individual taper surfaces from fatigue and corrosion tests: A) Fretting damage of Ti6Al4V necks; B) Fretting damage of CoCrMo necks; C) Corrosion damage of Ti6Al4V necks; D) Corrosion damage of CoCrMo necks; E) Overall combined damage for each surface from all the tested necks, including 10 fatigue and 12 corrosion tests. Note: only four hand-assembled Ti6Al4V necks were evaluated due to the fracture of two necks during fatigue tests.

Following the individual surface analysis for each neck, the fretting and corrosion scores of each surface were converted into a single overall score (i.e., most representative). The resulted overall Goldberg fretting and corrosion scores are shown in Figures 4.11 and 4.12, respectively. For this analysis, the test type (fatigue and corrosion) were considered separately.

The overall fretting scores (Figure 4.11) showed that Ti6Al4V necks suffered more severe fretting damage than CoCrMo necks during both fatigue and corrosion tests. Overall, the impact assembly appeared to decrease fretting damage for both neck materials. Finally, fatigue tests caused overall more fretting damage than corrosion tests, likely because of a higher load applied during fatigue tests.

The overall corrosion score results (Figure 4.12) showed more corrosion damage on the CoCrMo necks than the Ti6Al4V necks during both fatigue and corrosion tests. For the Ti6Al4V necks, the impact assembly resulted in less corrosion damage during the corrosion tests than during the fatigue tests. For the CoCrMo necks, the impact assembly did not reduce the corrosion damage compared to the hand-assembly during the fatigue tests. However, the impact-assembled CoCrMo necks exhibited less corrosion damage than the hand-assembled necks after corrosion tests. Examples of some of the advanced wear and fretting damage are shown in Figures 4.13 and 4.14, while examples of advanced corrosion are shown Figures 4.15 and 4.16. The overall fretting and corrosion Goldberg scores of the tested necks are provided in Appendix G.

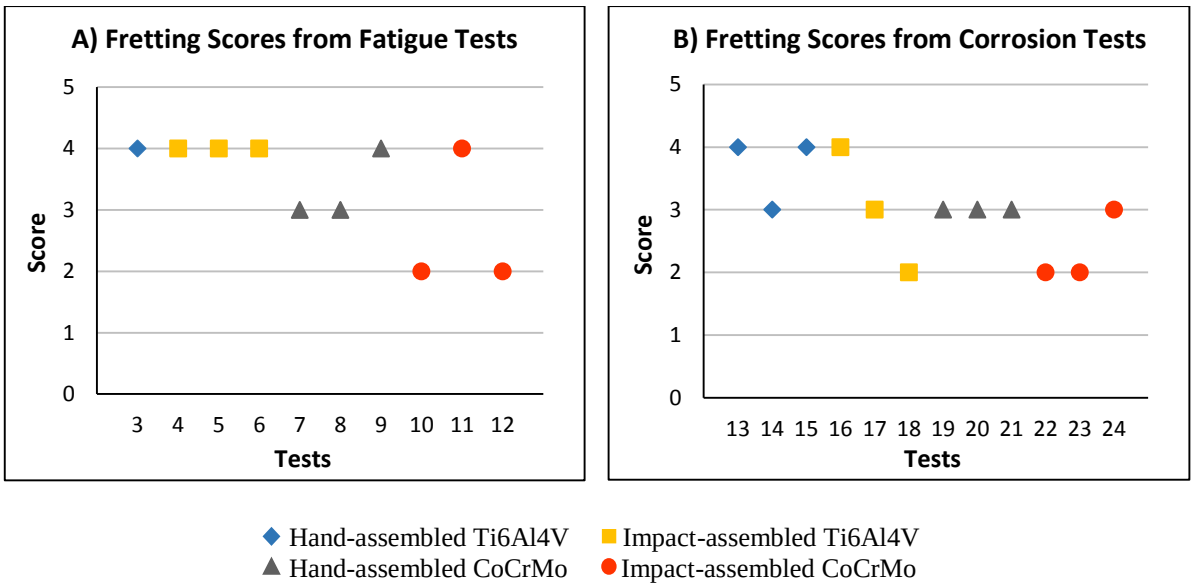

Figure 4.11: Overall Goldberg fretting damage scores of Ti6Al4V and CoCrMo modular necks after: A) fatigue tests; B) corrosion tests. Note: only one hand-assembled Ti6Al4V neck tested for fatigue was evaluated.

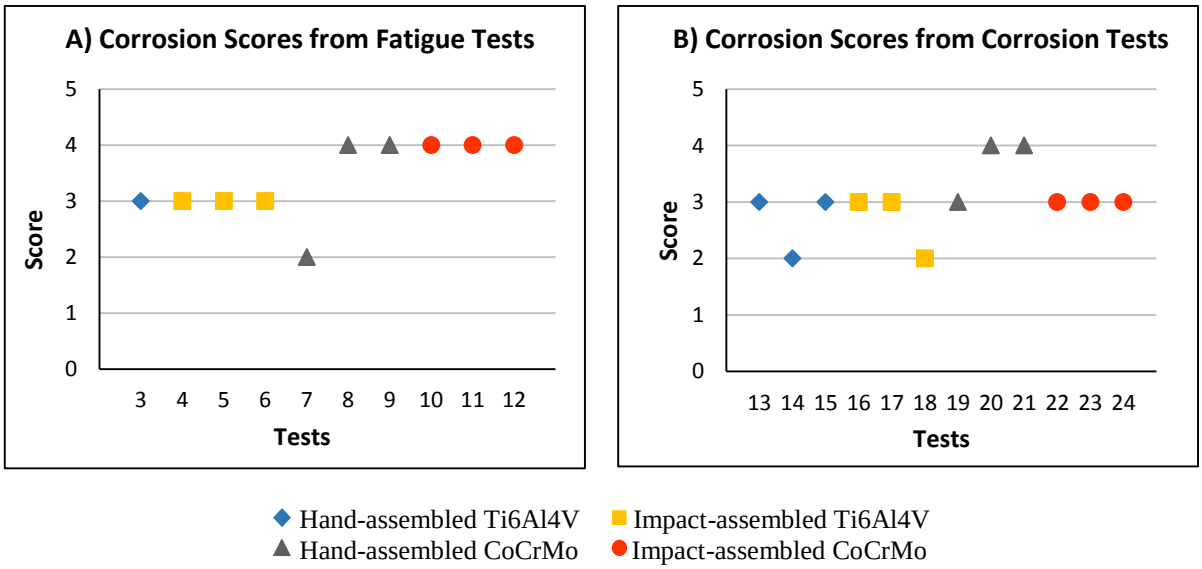

Figure 4.12: Overall Goldberg corrosion damage scores of Ti6Al4V and CoCrMo modular necks after: A) fatigue tests; B) corrosion tests. Note: only one hand-assembled Ti6Al4V neck tested for fatigue was evaluated.

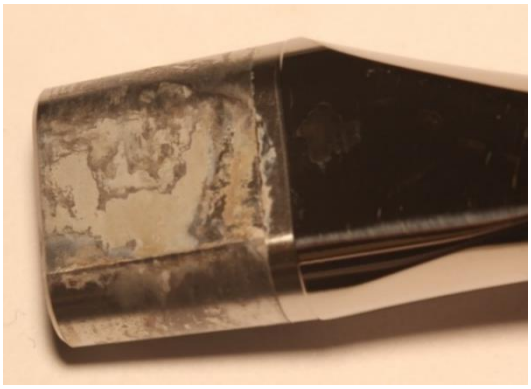

Figure 4.13: Advanced fretting associated with corrosion damage on the anterior surface of a hand-assembled CoCrMo neck following a fatigue test.

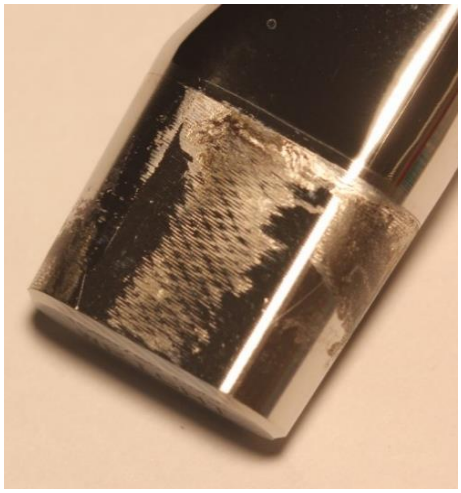

Figure 4.14: Severe wear on the anterior surface of an impact-assembled Ti6Al4V neck following a fatigue test leading to material removal off the neck taper.

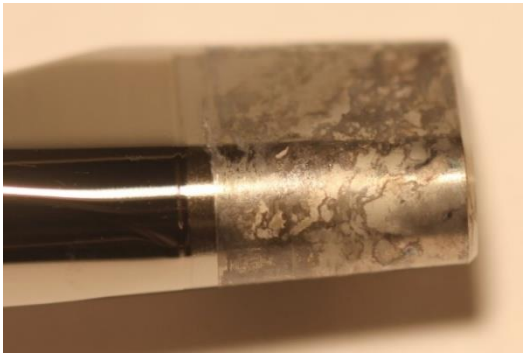

Figure 4.15: Severe wear-corrosion on the medial and posterior surfaces of a hand-assembled Ti6Al4V neck following a corrosion test.

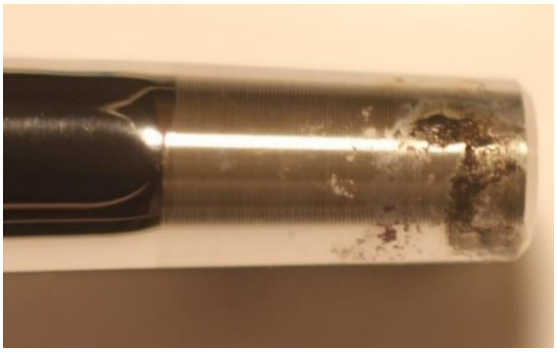

Figure 4.16: The formation of black debris on the lateral surface of a hand-assembled CoCrMo neck following a corrosion test as a result of advanced corrosion.

5 Discussion

5.1 pH of the Bath Solution and Stem Pocket

Buffer solutions consist of an acid and its conjugate base that maintain a constant pH. The buffering capacity is the solution resistance to a pH change when a strong acid or base is added to the solution [59]. For a given solution, the buffering capacity can be increased by increasing the concentration or molarity of the buffer substances [60].

In the present study, PBS was used to limit the fluctuation of the bath pH, which can affect the corrosion rate. At the same time, since crevice corrosion typically leads to a drop in stem pocket pH [61], a PBS with low buffering capacity (6.7 mM sodium potassium phosphate) was selected to allow the detection of expected pH changes in the narrow crevice between the modular components during the mechanical tests. The experimental results showed that the corrosion of some Ti6Al4V necks led to strongly acidic stem pocket pH, which may be attributed to the depletion of oxygen ions as a result of crevice corrosion [62].

With regards to the bath solution, the two factors that influence the buffer solution pH in the present study are the temperature [60] and the test duration. The pH of the bath solution increased slightly during the first 3.0 million cycles or so, and then more substantially thereafter. Consequently, the pH change was more substantial during the longer corrosion tests (5.0 million cycles) and only moderate during the shorter fatigue tests (1.3 million cycles). Furthermore, solution contamination resulting from the potting epoxy or the test fixture could contribute to the pH change. For instance, an unusual final solution pH of 9.1 with one of the impact-assembled Ti6Al4V necks tested for corrosion was recorded in a test during which one of the heaters failed at the wire junction, potentially releasing debris in the test solution. It shall

be noted that the simultaneous occurrence of increased bath pH (to basic values) and reduced stem pocket pH (to acidic values) may suggest that the changes in pH are partially related to a transfer or diffusion of H^+ ions from the overall bath into the neck-stem interface and the stem pocket. Therefore, the use of a PBS with a low buffering capacity, the elevated solution temperature, the potential contaminations, and the relatively long test duration were the primary causes of the observed pH changes.

5.2 Endurance and Wear-Corrosion Resistance of the Ti6Al4V/CoCrMo Necks

Fatigue tests showed that Ti6Al4V necks were more susceptible to fatigue fracture than CoCrMo necks. This result was expected for two main reasons. First, previous experimental and modelling studies showed that CoCrMo necks have a 38% higher load bearing capacity and nearly 1000 times longer fatigue life than Ti6Al4V necks [57]. Second, since the fatigue fracture of the modular neck was recognized to be primarily induced by fretting caused by micromotion between the modular neck and the stem [63], the higher strength, hardness [64] and wear resistance of CoCrMo lead to delayed surface damage, crack initiation and consequently longer fatigue life. In addition, CoCrMo has a better notch sensitivity compared to Ti6Al4V, which can further increase the fatigue resistance [61]. Therefore, CoCrMo is currently considered as a substitute to Ti6Al4V to overcome the premature *in vivo* modular neck fractures observed in recent years.

Moreover, higher fretting scores were observed for Ti6Al4V necks compared to CoCrMo necks. This may be explained by micromotion of the Ti6Al4V necks causing fretting and wear of the interface surfaces. When the oxide (protective) layer is removed, Ti6Al4V and CoCrMo alloys tend to rebuild it due to their re-passivation property. However, too rapid wear is believed to prevent re-passivation leading to wear and corrosion. The lack of re-passivation

can also cause Ti6Al4V-Ti6Al4V interfaces to cold weld [65,66], preventing the modular neck disassembly.

A common type of corrosion that is found in THR is mechanically assisted crevice corrosion, which can affect both Ti6Al4V and CoCrMo alloys by the formation of a corrosion cell due to the presence of body fluids in the narrow taper interface [67,68]. In the present study, the accumulation of PBS inside the stem pocket could have favoured the formation of a crevice corrosion cell. Continuous oxide layer removal and re-passivation can deplete the oxygen at the interface, inhibiting re-passivation and exposing the bare component substrate material to accelerated corrosion, which can result in the release of metal ions and cause adverse tissue reactions [62,69]. This continuous removal of the oxide layer could have affected the Ti6Al4V necks more than the CoCrMo necks, due to the lower hardness of the Ti6Al4V oxide layer, thus, resulting in a potentially stronger crevice corrosion damage. Interestingly, results showed more advanced corrosion on the CoCrMo necks, which may be partially explained by some galvanic corrosion when assembled with the Ti6Al4V stems due to the coupling of dissimilar metals, as reported in the literature [67,70]. Moreover, the mechanical wear and fretting between the CoCrMo neck and the Ti6Al4V stem could have disturbed and damaged the oxide layers of the two components, which could weaken the corrosion resistance between the two components and increase the likelihood of the formation of a galvanic cell between the two dissimilar alloys.

5.3 Effects of Assembly Method

Not many studies have been reported on the effect of assembly force on the mechanical performance of the modular necks in THR. In one study, Pallini et al. measured a higher distraction force with manually-assembled (i.e., manual insertion) necks (27 N) subjected to

low load-bearing activities (100 gait cycles) than with impact-assembled necks (three hammer blows with a magnitude of 1311 ± 43 N) for large stems [71]. On the other hand, small stems required a relatively similar distraction force whether the necks were impact-assembled or manually-assembled and then subjected to low load-bearing activity [71]. Therefore, it was suggested that the impaction of the neck is not necessary if not required to avoid taper contamination [71]. Indeed, contaminated taper interfaces were found to induce more micromotion than clean interfaces [72], which may lead to increased wear-corrosion damage and early fatigue crack initiation.

In the present study, however, the effect of assembly method was clearly demonstrated when comparing the Ti6Al4V necks tested for fatigue. All impact-assembled necks completed fatigue tests without failure, while all hand-assembled necks failed (two fractured and one exhibited a crack). This result showed that impact assembly of the modular necks contributes to achieve a better mechanical interlock between the modular neck and the stem, which reduces the micromotion and fretting, and increases the fatigue life of the Ti6Al4V neck.

On the other hand, impact assembly did not prevent wear-corrosion damage at the neck-stem interface and did not completely seal the neck-stem interface against fluid accumulation. Furthermore, impact-assembled necks, regardless of the material, overall required a higher distraction force compared to hand-assembled necks (Figure 4.7), suggesting larger surface deformations at the neck taper. Although this may result in some difficulties during *in vivo* neck retrievals as higher distraction forces may be required, the improved fatigue life of the impact-assembled necks highlights the importance of proper assembly technique of the modular necks.

5.4 Effects of Test Parameters (Load, Duration, and Corrosive Environment)

In the present study, the overall wear-corrosion damage from fatigue tests conducted under a compression load of 7.0 kN for 1.3 million cycles was more significant than that from corrosion tests conducted under a compression load of 2.3 kN for 5.0 million cycles. This indicates that the level of mechanical load may influence the overall wear-corrosion damage more than the duration of the test despite some studies that have shown an increased surface damage with longer implantation times [64,65]. Overall, the results of the present study corroborate those from Viceconti et al., who showed that necks tested under higher load resulted in larger overall surface damage [73]. This points to the higher risk of implant fracture for patients with higher physical activity level or body weight [63], not only with respect to fatigue fracture, but also with respect to potential micromotion, component wear, ion and particle release, and consequently potential biological reactions.

In addition, corrosion tests revealed more solution accumulation in the stem pocket compared to fatigue tests of the same neck material and assembly method (Figure 4.3). This indicates that the taper junction cannot prevent body fluids or other substances from the surrounding environment to enter the stem pocket, which can influence and favour corrosion at the junction as time progresses.

From a design point of view, the neck section just below the head-neck taper has the smallest cross-sectional area and is therefore expected to be the weakest region with the highest stress concentration. However, the highest bending moment on the neck occurs at its entry point into the stem due to the large lever arm, which, combined with fretting damage, can lead to fatigue fracture at that region, as observed *in vivo* [3,4]. A relatively high cyclic loading

frequency of 10 Hz proved to better reproduce this *in vivo* fracture location, even though a normal gait has a frequency between 1 and 3 Hz [74].

Finally, a bovine serum at 37 ºC was previously used to simulate the corrosive environment for Ti6Al4V and CoCrMo necks. However, no signs of fretting or corrosion were observed on the tested samples [57]. Therefore, although the ISO 7206-6-1992 Standard suggests a testing temperature of 37 °C to mimic the human body temperature, an elevated temperature of 80 ºC was used in the present study to accelerate the corrosion reaction [42]. This higher temperature together with the use of a PBS solution proved to be better at reproducing *in vivo* wear-corrosion damage at the neck-stem interface and allowed to efficiently compare the degree of fretting and corrosion between the different testing groups. Lastly, the addition of a 12 hours resting period after every 12 hours cyclic loading period helped increase the ratio of corrosion-to-wear and corrosion-to-fatigue damage, allowing for better simulation of *in vivo* conditions, where corrosion proceeds even during unloaded phases of the implant.

5.5 Location of Fatigue Fracture and Wear-Corrosion Damage

The location of the wear, corrosion and fatigue fracture initiation can be correlated to the loading mode as illustrated in Figure 5.1a. The bending moment resulting from the test load at the femoral head (point contact) is counter-balanced primarily by localized reaction forces at the neck taper lateral and medial ends, resulting in high reaction forces as indicated by the arrows shown in Figure 5.1a. Therefore, the fatigue crack initiated at the distal lateral end, and then propagated diagonally through the taper until final fracture at the proximal medial end, as seen in the failed Ti6Al4V necks (Figure 5.1b). These locations are also consistent with the regions of the strongest wear-corrosion damage observed in the present

study and reported in the literature [73]. Furthermore, the implant loading mode led to higher compression loads on the anterior surface of the modular neck taper, which suffered more wear-corrosion damage than the posterior surface, as depicted by the Goldberg scores on each surface (Figure 4.10E).

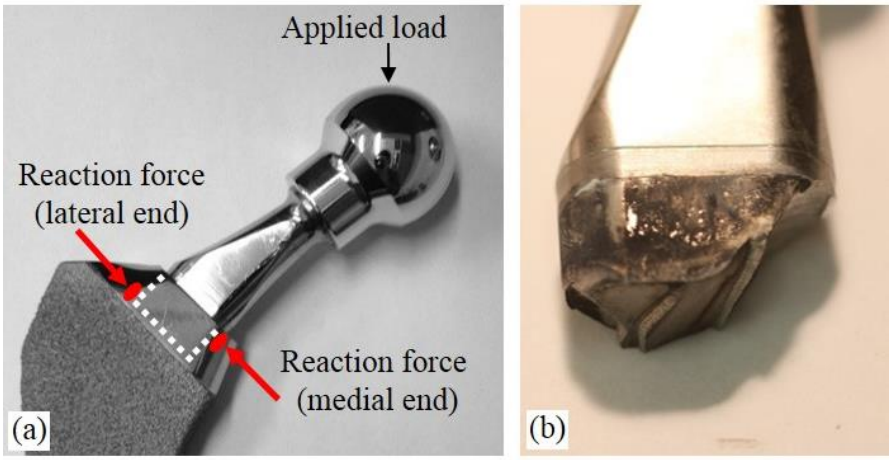

Figure 5.1: An Anterior view of a THR implant depicting: (a) The fatigue load application point and the neck locations with the highest local reaction force (arrows); (b) The diagonal neck fracture path between the two locations with the highest local compressive reaction load.

5.6 *In Vivo* and *In Vitro* Implant Alignment Comparison

From the simplified cantilever beam analysis for the modular neck in Appendix H, upon loading the implant at the femoral head (Figure 5.2), the F_z and F_y force vectors are applied perpendicular to the neck-stem taper interface, which can result in high bending stresses at the neck-stem interface. On the other hand, the F_x force vector is applied parallel to the neck axis, and therefore, may not be as a critical factor in the modular neck fracture as the F_z and F_y force vectors. By analyzing the *in vivo* force vectors for a normal walking activity [43] with an assumed body weight of 100 kg for an average adult, the *in vivo* β angle was found to be about 15° (Appendix H), which is in a close range to the suggested alignment angle of β = 9° in the

ISO 7206-4-2002 Standard. Furthermore, the comparison of the mechanical load used in corrosion tests of 2.3 kN (adopted from ISO 7206-8-1995 and ASTM 2068 Standards), and the measured *in vivo* force on the hip implant by Bergmann et al. [43] (Appendix H), revealed that the *in vivo* and *in vitro* implant alignment resulted in a high F_z force vector magnitude and consequently high bending stress at the neck-stem taper interface compared to the F_y force vector. It is important to note that this is a simplified calculation to compare the alignment angle and the most effective force vector on the neck-stem taper interface between the *in vivo* and *in vitro* implant behaviour for relatively normal activity and load. In reality, the force vector magnitudes can be affected by the type of activity, which may result in different bending moments and stresses on the implant.

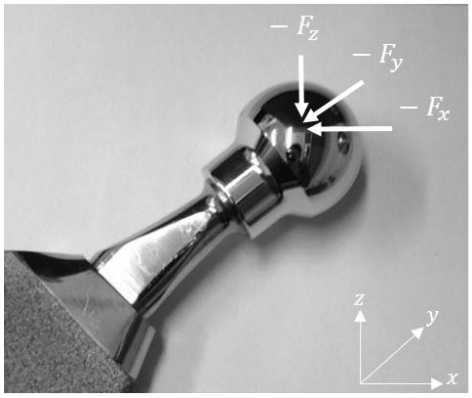

Figure 5.2: A coordinate system of the force vectors on the tested implants.

5.7 Factors Influencing the Distraction Force

Impact assembly causes larger deformations in the neck taper leading to a tighter fit and mechanical interlock between the neck and the stem, which results in a higher distraction force than with hand assembly. Moreover, the taper interlock is tighter with Ti6Al4V necks than with CoCrMo necks. Generally, this leads to higher distraction forces for Ti6Al4V necks and can, together with potential cold welding, prevent component disassembly *in vivo*. Overall, the

impact-assembled Ti6Al4V necks after the corrosion tests required the highest distraction force. These results suggest that the distraction force depends primarily on the neck material and the force applied during assembling of the modular neck (i.e., assembly method).

6 Conclusion

In vivo modular femoral neck fracture and wear-corrosion damage were successfully simulated in the *in vitro* setting. Fatigue tests showed that Ti6Al4V necks are more susceptible to fatigue failure than CoCrMo necks, and the impact assembly contributed to improve the fatigue life of the modular necks compared to the hand assembly. However, the impact assembly did not seal the neck-stem taper interface completely. Also, it resulted in higher distraction forces than with the hand assembly.

The use of 10 Hz cyclic loading frequency and the overall higher fatigue load reproduced a consistent neck fracture location similar to that seen in retrieved *in vivo* implants. Moreover, the use of PBS and an elevated testing temperature of 80 ºC as a simulation environment, along with the addition of the 12 hours loading and 12 hours resting cyclic periods, helped to generate wear-corrosion levels similar to those seen in retrievals and allowed for comparison between the different investigated groups. The higher loads used for the fatigue tests resulted in more fretting and corrosion damage than the longer test duration used for the corrosion tests. However, fluid accumulation in the stem pocket increased with the increase in the number of loading cycles.

In terms of wear and corrosion resistance, regardless of the neck material and assembly method, fretting, wear, and corrosion occurred at the neck-stem taper interface. However, Ti6Al4V necks were more susceptible to fretting and wear, while CoCrMo necks were more susceptible to corrosion. The successful replication of the *in vivo* fatigue, wear, and corrosion behaviour of modular necks used in THR provides a basis for potential future improvements of the implants and of the international testing standards.

7 Limitations and Future Work

Although the *in vitro* simulation achieved the purpose of reproducing the *in vivo* modular neck behaviour in terms of fracture mode and location, wear, and corrosion, the following remarks can be considered for further improvements:

- The small number of samples per group (N = 3) limited the statistical analysis of the results. Larger sample sizes are recommended for future studies as they would provide a better data distribution and strengthen the analysis. Alternatively, subsequent studies could be designed to focus on specific individual factors such as neck material, assembly method, and distraction force, particularly as they relate to wear, corrosion, particles generation, and ions release.
- Future experiments could consider direct measurement of micromotion between the modular components. Also, electrochemical tests could be used to study the potential difference and the corrosion reactions that take place during the *in vitro* simulation, especially for the CoCrMo modular necks.
- As wear particles and ions are among the major concerns with metal components in joint replacements, the analysis of wear particle sizes and levels of released ions are desirable. Comparing such results with *in vivo* data would offer a more complete *in vitro* assessment of the wear and corrosion of the implants.

References

[1] S. R. Knight, R. Aujla, and S. P. Biswas, Total Hip Arthroplasty - over 100 years of operative history, Orthop. Rev., vol. 3, pp. 72–74, 2011.

[2] Canadian Institute for Health Information, Hip and Knee Replacements in Canada: Canadian Joint Replacement Registry 2014 Annual Report, Ottawa, ON, CIHI, 2014.

[3] C. J. Dangles and C. J. Altstetter, Failure of the Modular Neck in a Total Hip Arthroplasty, J. Arthroplasty, vol. 25, no. 7, pp. 1169.e5–1169.e7, 2010.

[4] G. Wright, S. Sporer, R. Urban, and J. Jacobs, Fracture of a Modular Femoral Neck After Total Hip Arthroplasty, J. Bone Joint Surg. Am., vol. 92, pp. 1518–1521, 2010.

[5] H. J. Cooper, R. M. Urban, R. L. Wixson, R. M. Meneghini, and J. J. Jacobs, Adverse Local Tissue Reaction Arising from Corrosion at the Femoral Neck-Body Junction in a Dual-Taper Stem with a Cobalt-Chromium Modular Neck, J. Bone Joint Surg. Am., vol. 95, no. 10, pp. 865–72, 2013.

[6] R. L. Drake, A. W. Vogl, and A. W. M. Mitchell, Gray's Anatomy for Students, 3 rd. Philadelphia, USA: Churchill Livingstone, 2014.

[7] M. Schuenke, E. Schulte, and U. Schumacher, Thieme Atlas of Anatomy: Latin Nomenclature: General Anatomy and Musculoskeletal System. New York, USA: THIEME, 2006.

[8] D. P. Byrne, K. J. Mulhall, and J. F. Baker, Anatomy & Biomechanics of the Hip, Open Sport. Med. J., pp. 51–57, 2010.

[9] L. L. Kelley and C. M. Petersen, Sectional Anatomy for Imaging Professionals, 3rd ed. St. Louis, USA: Mosby, 2013.

[10] A. E. Chapman, Biomechanical Analysis of Fundamental Human Movements. Chapman, Arther E., 2008.

[11] J. A. Marx, R. S. Hockberger, and R. M. Walls, Rosen's Emergency Medicine - Concepts and Clinical Practice, 8th ed. Philadelphia, USA: Saunders, 2014.

[12] E. Kreighbaum and K. M. Barthels, Biomechanics: A Qualitative Approach for Studying Human Movement, 4th ed. USA: Allyn and Bacon, 1996.

[13] P. C. Neligan, Ed., Plastic Surgery: Volume Six: Hand and Upper Limbs, 3rd ed. Saunders, 2013.

[14] C. H. Turner, Bone Strength: Current Concepts, Ann. N. Y. Acad. Sci., vol. 1068, pp. 429–446, 2006.

[15] S. J. Hall, Basic Biomechanics, 5th ed. New York, USA: McGraw-Hill, 2006.

[16] M. Kutz, Standard Handbook of Biomedical Engineering & Design. USA: McGraw-Hill, 2003.

[17] W. M. Haschek, C. G. Rousseaux, and M. A. Wallig, Eds., Haschek and Rousseaux's Handbook of Toxicologic Pathology, 3rd ed. London, UK: Academic Press, 2013.

[18] D. T. Reilly and A. H. Burstein, The Elastic and Ultiamate Properties of Compact Bone Tissue, J. Biomech., vol. 8, pp. 393–405, 1975.

[19] Y. H. An and R. A. Draughn, Eds., Mechanical Testing of Bone and the Bone-Implant Interface. CRC Press, 1999.

[20] M. R. Safran, J. Zachazewski, and D. A. Stone, Instructions for Sports Medicine Patients, 2nd ed. Philadelphia, USA: Saunders, 2012.

[21] S. D. Waldman, Atlas of Common Pain Syndromes, 3rd ed. Philadelphia, USA: Saunders, 2012.

[22] S. Melmed, K. S. Polonsky, P. R. Larsen, and H. M. Kronenberg, Williams Textbook of Endocrinology, 12th ed. Philadelphia, USA: Saunders, 2011.

[23] L. E. Wold, K. K. Unni, F. H. Sim, and M. Sundaram, Atlas of Orthopedic Pathology (Atlas of Surgical Pathology), 3rd ed. Philadelphia, USA: Saunders, 2008.

[24] K. Knahr, Ed., Total Hip Arthroplasty: Wear Behaviour of Different Articulations. Heidelberg, Germany: Springer, 2012.

[25] S. T. Canale and J. H. Beaty, Campbell's Operative Orthopaedics, 12th ed. Philadelphia, USA: Mosby, 2012.

[26] R. K. Sinha, Ed., Hip Replacement: Current Trends and Controversies. New York, USA: Marcel Dekker, Inc., 2002.

[27] A. Saverio, Ed., Wear of Orthopaedic Implants and Artificial Joints. Cambridge, UK: Woodhead Publishing Limited, 2012.

[28] X. Lou, Y. Li, and X. Lin, Effect of Proximal Femoral Osteoporosis on Cementless Hip Arthroplasty: A Short-Term Clinical Analysis, J. Zhejiang Univ. Sci. B, vol. 8, no. 1, pp. 76–80, 2007.

[29] M. Pennington, R. Grieve, J. S. Sekhon, P. Gregg, N. Black, and J. H. van der Meulen, Cemented, Cementless, and Hybrid Prostheses for Total Hip Replacement: Cost Effectiveness Analysis, BMJ, vol. 346, no. February, p. f1026, 2013.

[30] T. E. Brown, Q. Cui, W. M. Mihalko, and K. Saleh, Arthritis and Arthroplasty: The Hip. Philadelphia, USA: Saunders, 2009.

[31] K. Knahr, Ed., Tribology in Total Hip Arthroplasty. Heidelberg, Germany: Springer, 2011.

[32] R. M. R. Dyrkacz, J. M. Brandt, O. A. Ojo, T. R. Turgeon, and U. P. Wyss, The Influence of Head Size on Corrosion and Fretting Behaviour at the Head-Neck Interface of Artificial Hip Joints, J. Arthroplasty, vol. 28, no. 6, pp. 1036–1040, 2013.

[33] H. S. Khanuja, J. J. Vakil, M. S. Goddard, and M. A. Mont, Current Concepts Review: Cementless Femoral Fixation in Total Hip Arthroplasty, J. Bone Joint Surg. Am., vol. 93, pp. 500–509, 2011.

[34] M. Niinomi, Ed., Metals for Biomedical Devices. Cambridge, UK: Woodhead Publishing Limited and CRC Press, 2010.

[35] J. P. Boutrand, Ed., Biocompatibility and Performance of Medical Devices. Cambridge, UK: Woodhead Publishing Limited, 2012.

[36] W. D. J. Callister, Materials Science and Engineering: an Introduction, 7th ed. USA: John Wiley & Sons, Inc, 2007.

[37] L. A. Pruitt and A. M. Chakravartula, Mechanics of Biomaterials: Fundamental Principles for Implant Design. Cambridge, UK: Cambridge University Press, 2011.

[38] F. C. Campbell, Fatigue and Fracture: Understanding the Basics. USA: ASM International, 2012.

[39] B. Bhushan, Ed., Modern Tribology Handbook. CRC Press, 2008.

[40] B. Bhushan, Principles and Applications of Tribology. New York, USA: John Wiley & Sons, Inc., 1999.

[41] E. C. Fitch, Proactive Maintenance for Mechanical Systems. England: Elsevier Science Pblishers Ltd, 1992.

[42] J. R. Davis, Corrosion: Understanding the Basics. USA: ASM International, 2000.

[43] G. Bergmann, G. Deuretzbacher, M. Heller, F. Graichen, a. Rohlmann, J. Strauss, and G. N. Duda, Hip contact forces and gait patterns from routine activities, J. Biomech., vol. 34, no. 7, pp. 859–871, 2001.

[44] U.S. Food and Drug Administration, 2015. Silver Spring, Maryland, USA.

[45] M. B. Ellman and B. R. Levine, Fracture of the Modular Femoral Neck Component in Total Hip Arthroplasty, J. Arthroplasty, vol. 28, no. 1, 2013.

[46] J. G. Skendzel, J. D. Blaha, and A. G. Urquhart, Total Hip Arthroplasty Modular Neck Failure, J. Arthroplasty, vol. 26, no. 2, pp. 338.e1–338.e4, 2011.

[47] N. G. Sotereanos, T. J. Sauber, and T. T. Tupis, Modular Femoral Neck Fracture After Primary Total Hip Arthroplasty, J. Arthroplasty, vol. 28, no. 1, pp. 196.e7–196.e9, 2012.

[48] M. L. Mencière, T. Amouyel, J. Taviaux, M. Bayle, C. Laterza, and P. Mertl, Fracture of the Cobalt-Chromium Modular Femoral Neck Component in Total Hip Arthroplasty, Orthop. Traumatol. Surg. Res., no. 100, pp. 565–568, 2014.

[49] C. Restrepo, D. Ross, S. Restrepo, S. Heller, N. Goyal, R. Moore, and W. J. Hozack, Adverse Clinical Outcomes in a Primary Modular Neck/Stem System, J. Arthroplasty, vol. 29, no. 9, pp. 173–178, 2014.

[50] W. Q. Lindh, M. Pooler, C. D. Tamparo, and B. M. Dahl, Delmar's Clinical Medical Assisting, 4th ed. Delmar Cengage Learning, 2009.

[51] Wisent Inc., Phosphate Buffered Saline Formulation, Product Data Sheet, Quebec, Canada, Catalog no. 311-010.

[52] International Standard, Implants for Surgery - Partial and Total Hip Prostheses: Determination of Endurance Properties of Stemmed Femoral Components, ISO 7206-4, 2002.

[53] M. Nganbe, H. Louati, U. Khan, A. Speirs, and P. E. Beaulé, Retrieval Analysis and In Vitro Assessment of Strength, Durability, and Distraction of a Modular Total Hip Replacement, J. Biomed. Mater. Res. - Part A, vol. 95, pp. 819–827, 2010.

[54] H. Louati, Investigating the Mechanical Properties of a Titanium Based Hip Implant Prosthesis, Bachelor Thesis, University of Ottawa, 2009.

[55] C. A. Harper and E. M. Petrie, Plastics Materials and Processes: A Concise Encyclopedia. Hoboken, USA: John Wiley & Sons, Inc., 2003.

[56] A. T. Pennock, A. H. Schmidt, and C. A. Bourgeault, Morse-Type Tapers: Factors That May Influence Taper Strength During Total Hip Arthroplasty, J. Arthroplasty, vol. 17, no. 6, pp. 773–778, 2002.

[57] M. Nganbe, U. Khan, H. Louati, A. Speirs, and P. E. Beaulé, In vitro Assessment of Strength, Fatigue Durability, and Disassembly of Ti6Al4V and CoCrMo Necks in Modular Total Hip Replacements, J. Biomed. Mater. Res. - Part B Appl. Biomater., vol. 97 B, pp. 132–138, 2011.

[58] J. R. Goldberg, J. L. Gilbert, J. J. Jacobs, T. W. Bauer, W. Paprosky, and S. Leurgans, A Multicenter Retrieval Study of the Taper Interfaces of Modular Hip Prostheses, Clin. Orthop. Relat. Res., no. 401, pp. 149–161, 2002.

[59] V. S. Stoll and J. S. Blanchard, Buffers: Principles and Practice, Methods Enzymol., vol. 182, no. 1966, pp. 24–38, 1990.

[60] C. Mohan, Buffers - A Guide for the Preparation and Use of Buffers in Biological Systems, Darmstadt, Germany, EMD Biosciences Inc., 2003.

[61] T. M. Grupp, T. Weik, W. Bloemer, and H.-P. Knaebel, Modular Titanium Alloy Neck Adapter Failures in Hip Replacement - Failure Mode Analysis and Influence of Implant Material, BMC Musculoskelet. Disord., vol. 11, p. 3, 2010.

[62] S. A. Brown, C. A. Flemming, J. S. Kawalec, H. E. Placko, C. Vassaux, K. Merritt, J. H. Payer, and M. J. Kraay, Fretting Corrosion Accelerates Crevice Corrosion of Modular Hip Tapers, J. Appl. Biomater., vol. 6, no. 1, pp. 19–26, 1995.

[63] S. Y. Jauch, G. Huber, K. Sellenschloh, H. Haschke, M. Baxmann, T. M. Grupp, and M. M. Morlock, Micromotions at the Taper Interface Between Stem and Neck Adapter of a Bimodular Hip Prosthesis During Activities of Daily Living, J. Orthop. Res., vol. 31, no. 8, pp. 1165–1171, 2013.

[64] G. B. Higgs, J. A. Hanzlik, D. W. MacDonald, J. L. Gilbert, C. M. Rimnac, and S. M. Kurtz, "Is Increased Modularity Associated With Increased Fretting and Corrosion Damage in Metal-On-Metal Total Hip Arthroplasty Devices? A Retrieval Study, J. Arthroplasty, vol. 28, no. 8, pp. 2–6, 2013.

[65] A. M. Kop, C. Keogh, and E. Swarts, Proximal Component Modularity in THA - At What Cost? An Implant Retrieval Study, Clin. Orthop. Relat. Res., vol. 470, no. 7, pp. 1885–1894, 2012.

[66] C. R. Fraitzl, L. E. Moya, L. Castellani, T. M. Wright, and R. L. Buly, Corrosion at the Stem-Sleeve Interface of a Modular Titanium Alloy Femoral Component as a Reason for Impaired Disengagement, J. Arthroplasty, vol. 26, no. 1, pp. 113–119.e1, 2011.

[67] H. Krishnan, S. P. Krishnan, G. Blunn, J. A. Skinner, and A. J. Hart, Instructional Review: Hip - Modular Neck Femoral Stems, Bone Jt. J., vol. 95 B, no. 8, pp. 1011–1021, 2013.

[68] J. L. Gilbert, S. Mali, R. M. Urban, C. D. Silverton, and J. J. Jacobs, In vivo oxide-induced stress corrosion cracking of Ti-6Al-4V in a neck-stem modular taper: Emergent behavior in a new mechanism of in vivo corrosion, J. Biomed. Mater. Res. Part B Appl. Biomater., vol. 100B, no. 2, pp. 584–594, 2012.

[69] I. P. S. Gill, J. Webb, K. Sloan, and R. J. Beaver, Corrosion at the Neck-Stem Junction as a Cause of Metal Ion Release and Pseudotumour Formation, J. Bone Jt. Surg. - Br. Vol., vol. 94-B, no. 7, pp. 895–900, 2012.

[70] J. P. Collier, V. A. Surprenant, R. E. Jensen, M. B. Mayor, and H. P. Surprenant, Corrosion Between the Components of Modular Femoral Hip Prostheses, J. Bone Joint Surg. Br., vol. 74, no. 4, pp. 511–517, 1992.

[71] F. Pallini, L. Cristofolini, F. Traina, and A. Toni, Modular Hip Stems: Determination of Disassembly Force of a Neck-Stem Coupling, Artif. Organs, vol. 31, no. 2, pp. 166–170, 2007.

[72] S. Y. Jauch, G. Huber, E. Hoenig, M. Baxmann, T. M. Grupp, and M. M. Morlock, Influence of Material Coupling and Assembly Condition on the Magnitude of Micromotion at the Stem-Neck Interface of a Modular Hip Endoprosthesis, J. Biomech., vol. 44, no. 9, pp. 1747–1751, 2011.

[73] M. K. Harman, M. Baleani, K. Juda, and M. Viceconti, Repeatable Procedure for Evaluating Taper Damage on Femoral Stems With Modular Necks, J. Biomed. Mater. Res. - Part B Appl. Biomater., vol. 99 B, no. 2, pp. 431–439, 2011.

[74] J. R. Goldberg and J. L. Gilbert, In Vitro Corrosion Testing of ModularHip Tapers, J. Biomed. Mater. Res. B. Appl. Biomater., vol. 64, no. 2, pp. 78–93, 2003.

Appendix A - Modular Femoral Neck Cleaning Procedure[1]

- Fill the ultrasonic bath with 5.0 L of distilled water containing 0.02% Benzalkonium Chloride.
- Set the ultrasonic bath solution to room temperature (21 °C).
- Submerse the neck in a beaker filled with acetone and sonicate the neck for 10 minutes.
- Then, replace the acetone with 1.0% Liquinox detergent solution, and sonicate the neck for 10 additional minutes.
- Once the cleaning process is completed, remove the neck from the beaker and rinse it twice; first with distilled water, then with 70% isopropyl alcohol.
- At the end, place the neck on KIMTECH wipes to dry at room temperature.

[1] The cleaning procedure was adopted from the Rush University Medical Center, Department of Orthopedic Surgery, Chicago, IL, USA, with some minor adjustments.

Appendix B - Replenishing Fluid Verification of Bath Solution

Table B.1: Measured pH of PBS (bath solution) with distilled water replenishing.

Day	pH
1	7.2
2	7.3
3	7.3
4	7.4
5	7.4

Table B.2: Measured pH of PBS (bath solution) with PBS replenishing.

Day	pH
1	7.3
2	7.3
3	7.3
4	7.3
5	7.3

Appendix C - PBS Preparation Steps

- Dissolve 45.0 g of NaCl into 4.5 L of distilled water, then mix the solution on a stir plate with the aid of a stir bar.
- Measure and add 3.98 g of Na_2HPO_4 to the solution while it is being mixed.
- Calibrate the pH meter in order to measure the pH of the prepared PBS.
- Dissolve 0.72 g of KH_2PO_4 in a small volume of distilled water (roughly 25 - 30 mL), then use it to titrate the PBS pH to 7.4 ± 0.1.
- Remove the solution off the stir plate to measure the precise volume of the solution with a graduated cylinder, then add the required volume of distilled water to reach a final solution volume of 5.0 L.
- Mix the final 5.0 L of PBS on the stir plate again and verify that the final pH of the 5.0 L PBS is 7.4 ± 0.1.
- Filter the PBS with a 0.2 µm filter in a biological safety cabinet, and fill it into glass autoclave-sterilized bottles to use it later for the mechanical tests.

Appendix D - Mechanical Drawings

Appendix D.1 - Tank (Solution Bath)

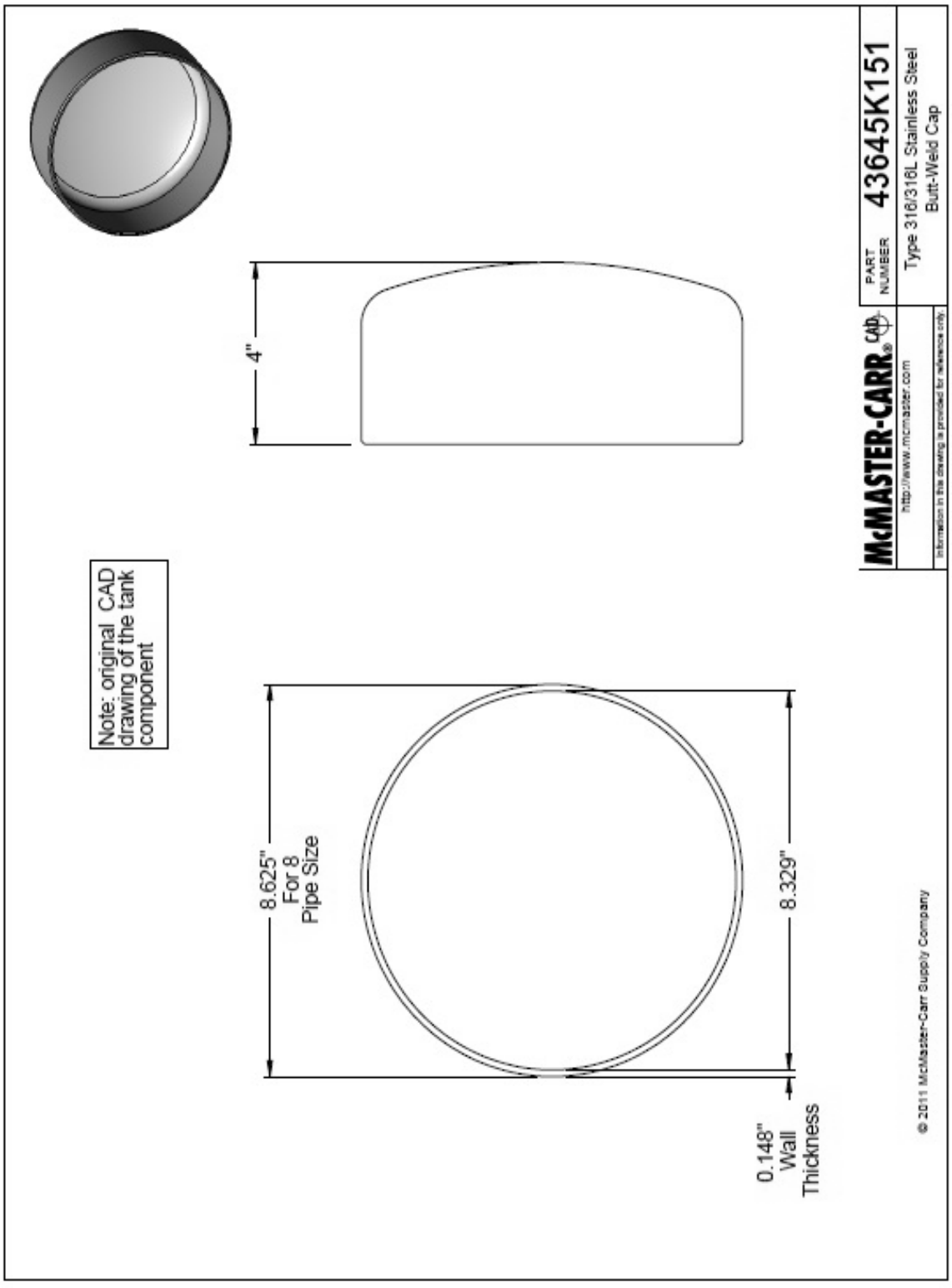

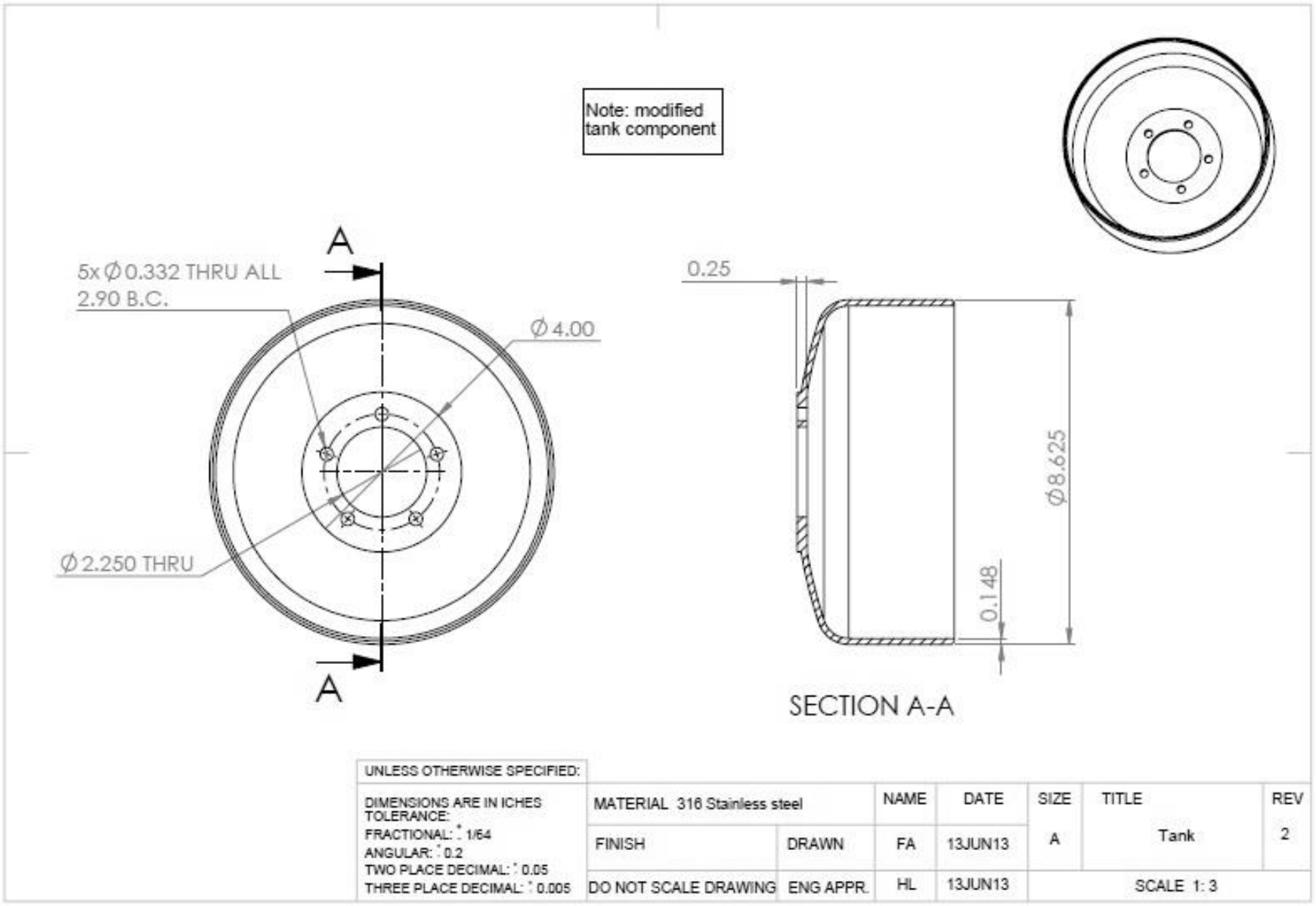
Note: modified tank component
5x Ø 0.332 THRU ALL
2.90 B.C.
Ø 4.00
Ø 2.250 THRU
A
A
0.25
Ø 8.625
0.148
SECTION A-A
UNLESS OTHERWISE SPECIFIED:
DIMENSIONS ARE IN ICHES
TOLERANCE:
FRACTIONAL: ± 1/64
ANGULAR: ± 0.2
TWO PLACE DECIMAL: ± 0.05
THREE PLACE DECIMAL: ± 0.005
MATERIAL 316 Stainless steel
FINISH
DRAWN
DO NOT SCALE DRAWING
ENG APPR.
NAME
DATE
FA
13JUN13
HL
13JUN13
SIZE
A
TITLE
Tank
REV
2
SCALE 1: 3

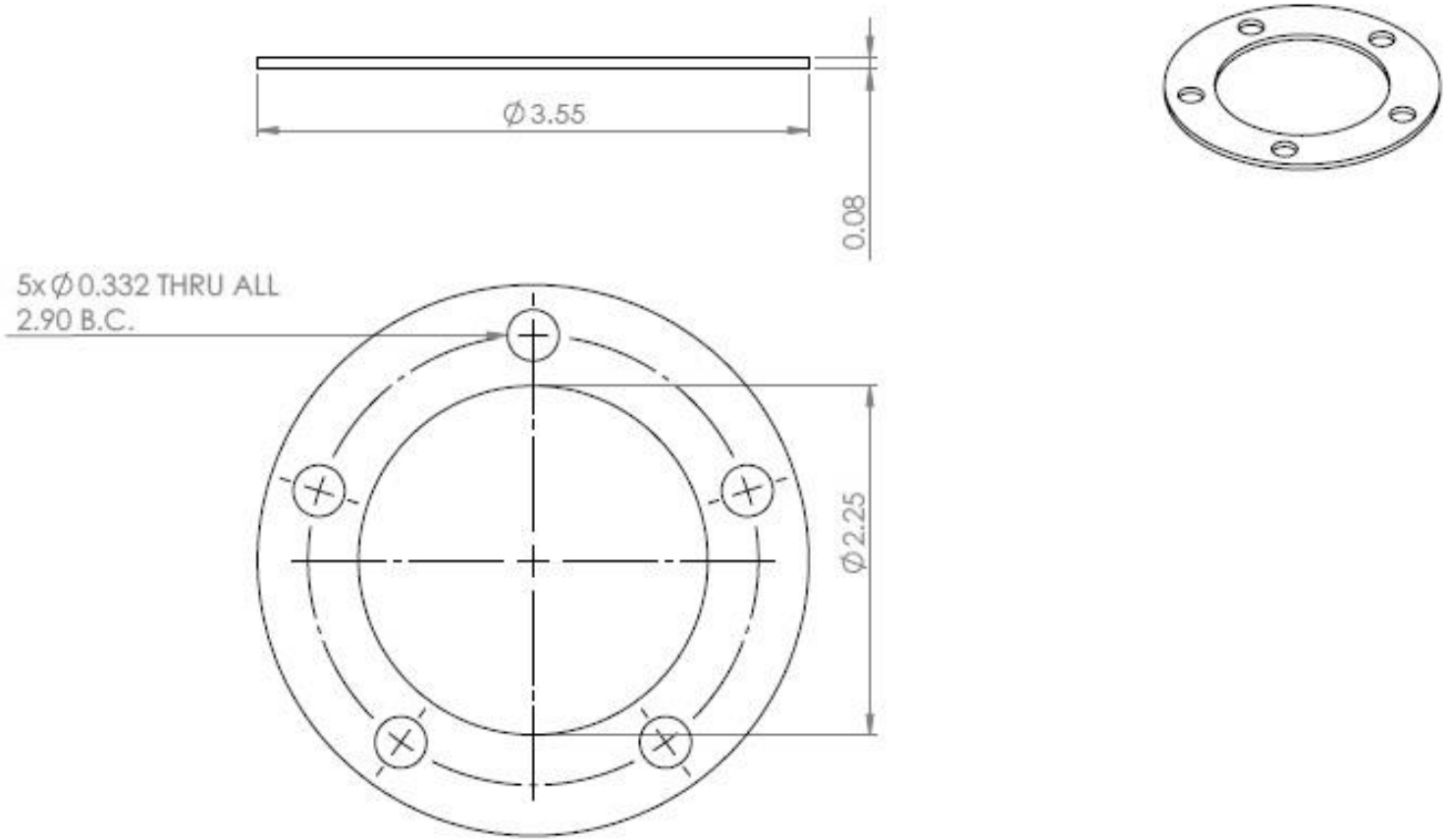

UNLESS OTHERWISE SPECIFIED:							
DIMENSIONS ARE IN ICHES TOLERANCE: FRACTIONAL: ± 1/64 ANGULAR: ± 0.2 TWO PLACE DECIMAL: ± 0.05 THREE PLACE DECIMAL: ± 0.005	MATERIAL 316 Stainless steel		NAME	DATE	SIZE	TITLE	REV
	FINISH	DRAWN	FA	17APR14	A	O-Ring	1
	DO NOT SCALE DRAWING	ENG APPR.	HL	17APR14	SCALE 1:1		

Appendix D.2 - 9º/10º Offset Angles Block

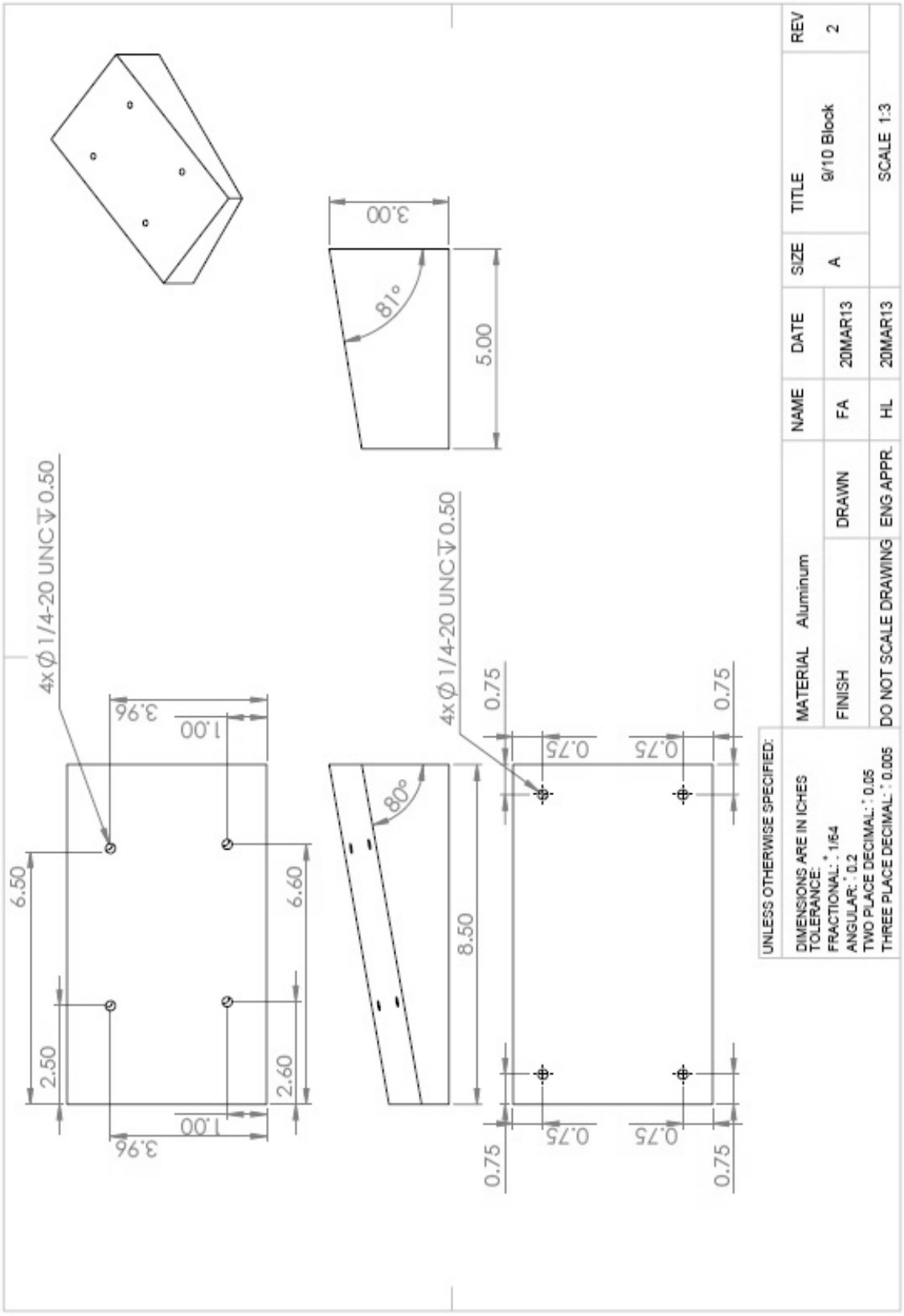

Appendix D.3 - Load Transfer Adaptor

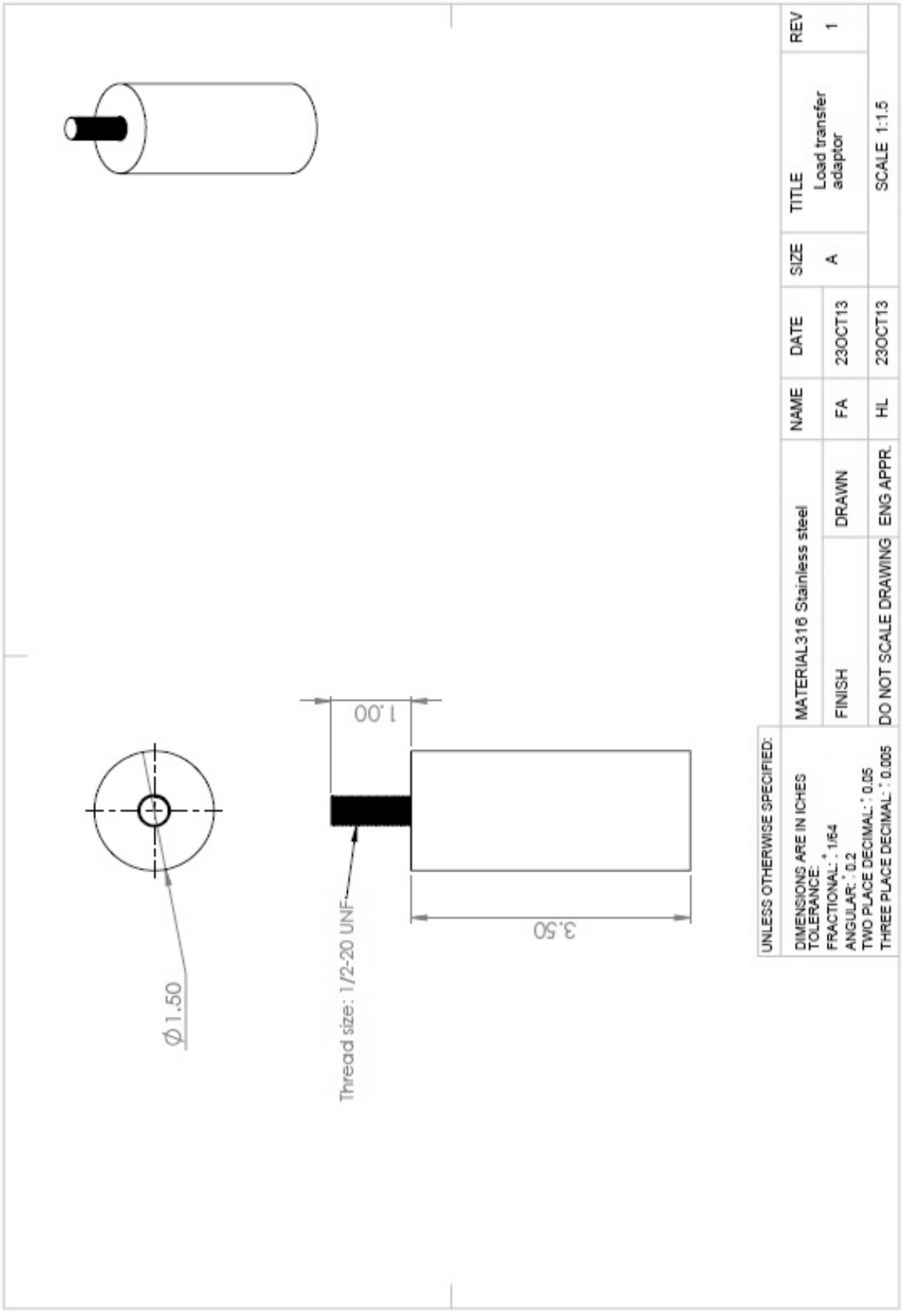

Appendix D.4 - Drop Tower

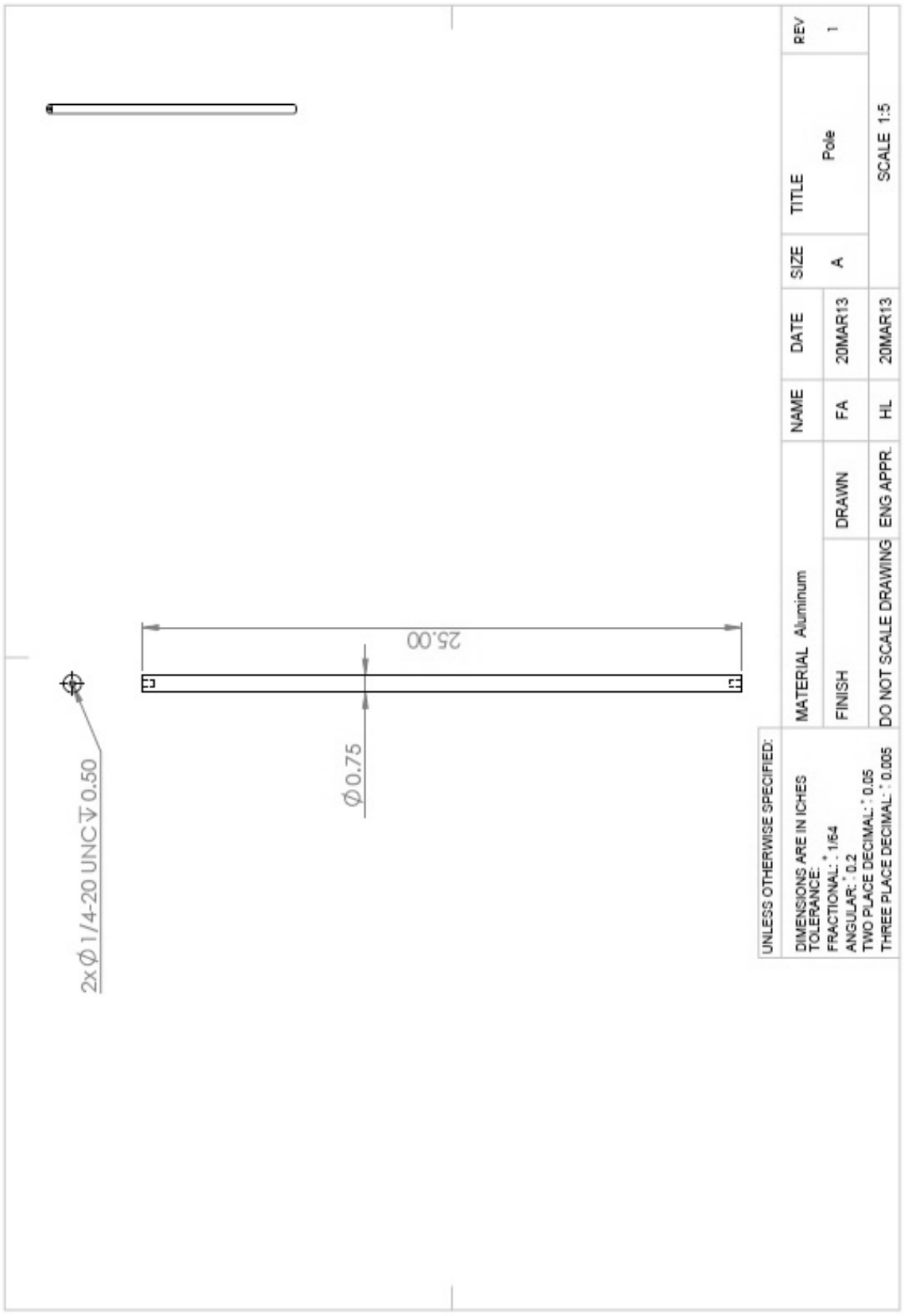

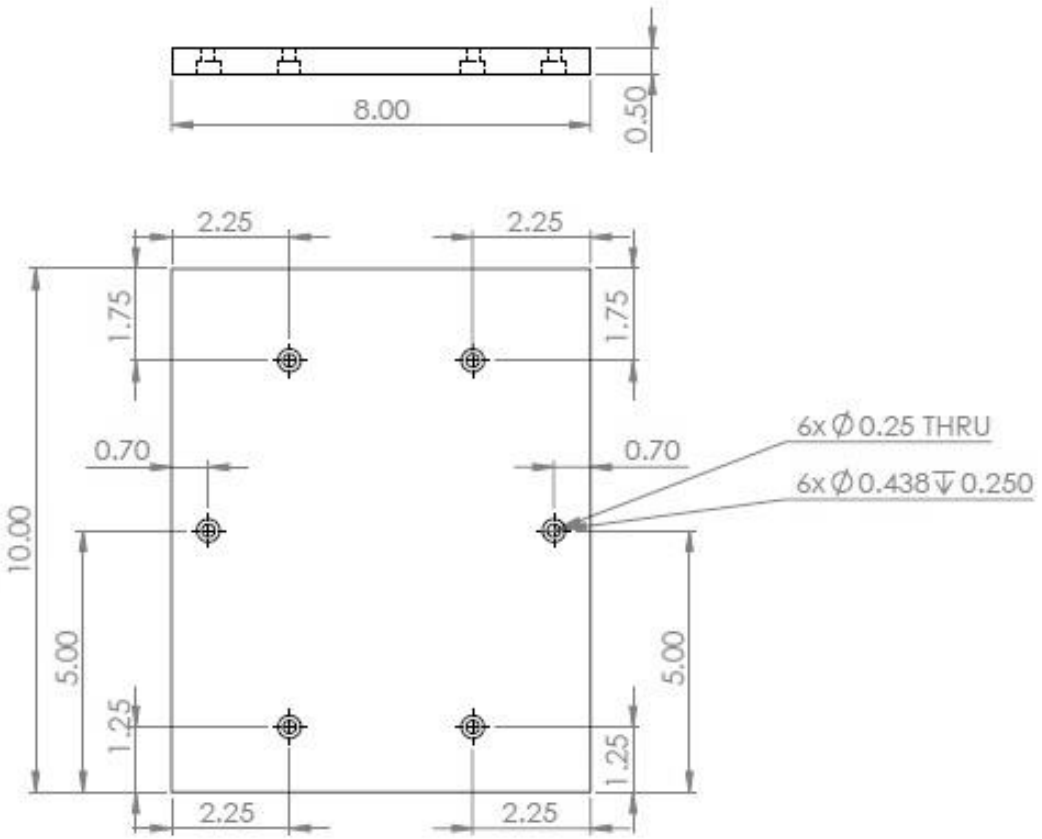

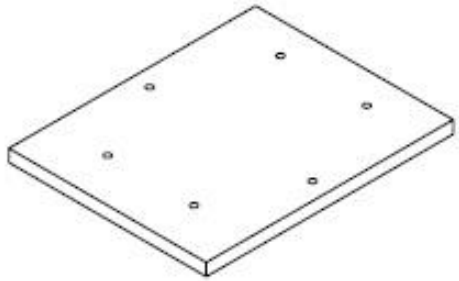

UNLESS OTHERWISE SPECIFIED:							
DIMENSIONS ARE IN ICHES TOLERANCE: FRACTIONAL: ± 1/64 ANGULAR: ± 0.2 TWO PLACE DECIMAL: ± 0.05 THREE PLACE DECIMAL: ± 0.005	MATERIAL PVDF		NAME	DATE	SIZE	TITLE	REV
	FINISH	DRAWN	FA	20MAR13	A	Base	2
	DO NOT SCALE DRAWING	ENG APPR.	HL	20MAR13	SCALE 1:3		

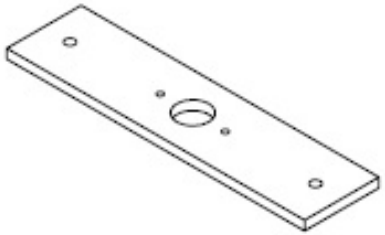

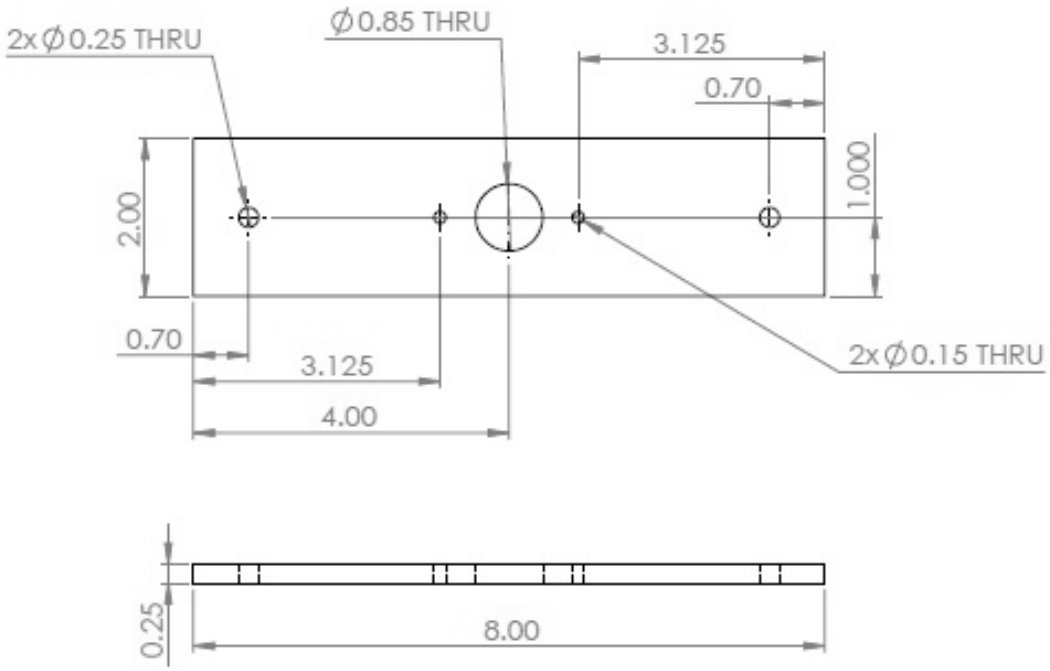

UNLESS OTHERWISE SPECIFIED:							
DIMENSIONS ARE IN ICHES TOLERANCE: FRACTIONAL: ± 1/64 ANGULAR: ± 0.2 TWO PLACE DECIMAL: ± 0.05 THREE PLACE DECIMAL: ± 0.005	MATERIAL Aluminum		NAME	DATE	SIZE	TITLE	REV
	FINISH	DRAWN	FA	12JUN13	A	Plate_1	1
	DO NOT SCALE DRAWING	ENG APPR.	HL	12JUN13	SCALE 1:2		

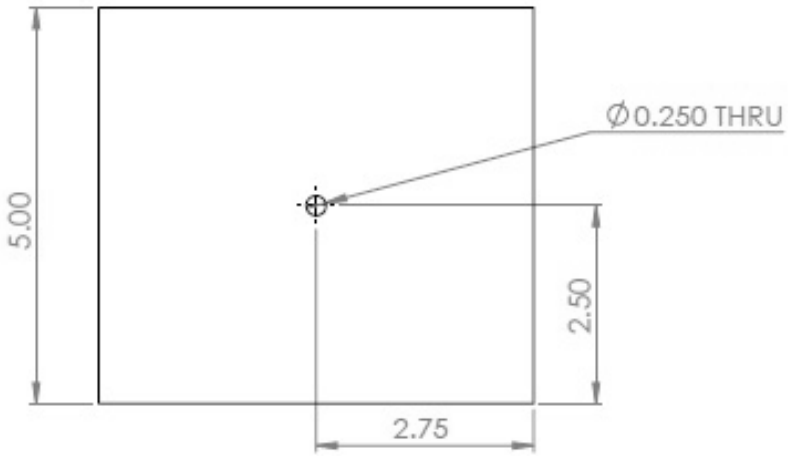

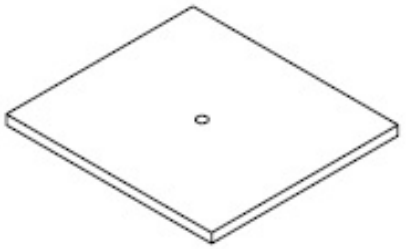

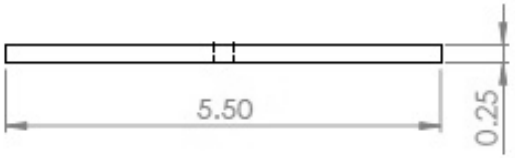

UNLESS OTHERWISE SPECIFIED:							
DIMENSIONS ARE IN ICHES TOLERANCE: FRACTIONAL: ± 1/64 ANGULAR: ± 0.2 TWO PLACE DECIMAL: ± 0.05 THREE PLACE DECIMAL: ± 0.005	MATERIAL Aluminum		NAME	DATE	SIZE	TITLE	REV
	FINISH	DRAWN	FA	26JUN13	A	Plate_2	1
	DO NOT SCALE DRAWING	ENG APPR.	HL	26JUN13	SCALE 1:2		

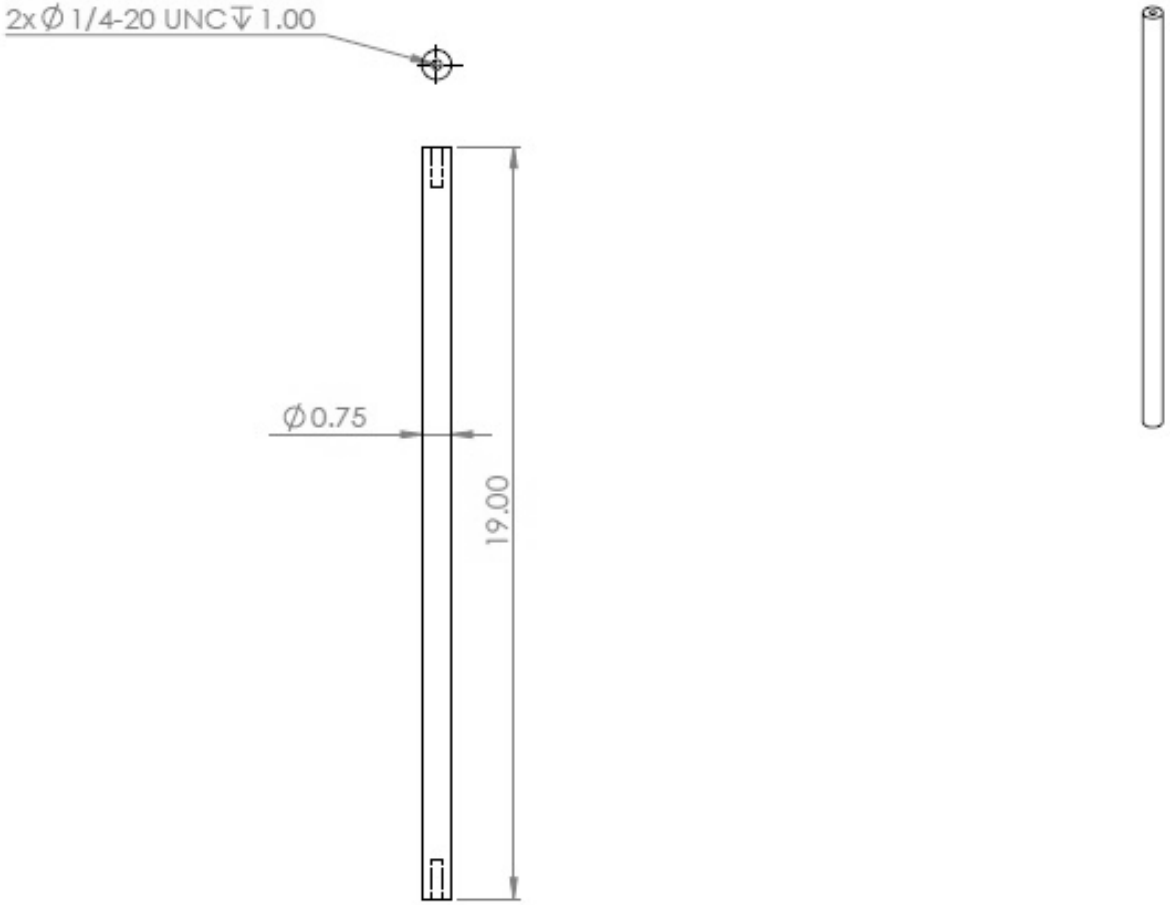

UNLESS OTHERWISE SPECIFIED:							
DIMENSIONS ARE IN ICHES TOLERANCE: FRACTIONAL: ± 1/64 ANGULAR: ± 0.2 TWO PLACE DECIMAL: ± 0.05 THREE PLACE DECIMAL: ± 0.005	MATERIAL Anodized aluminum		NAME	DATE	SIZE	TITLE	REV
	FINISH	DRAWN	FA	02JUL13	A	Hammer shaft	1
	DO NOT SCALE DRAWING	ENG APPR.	HL	02JUL13	SCALE 1:4		

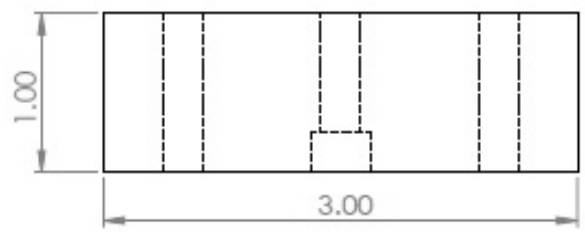

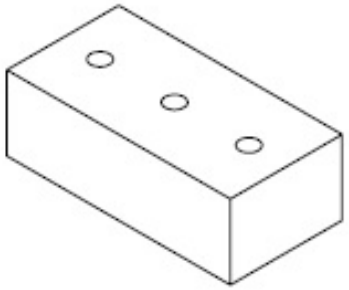

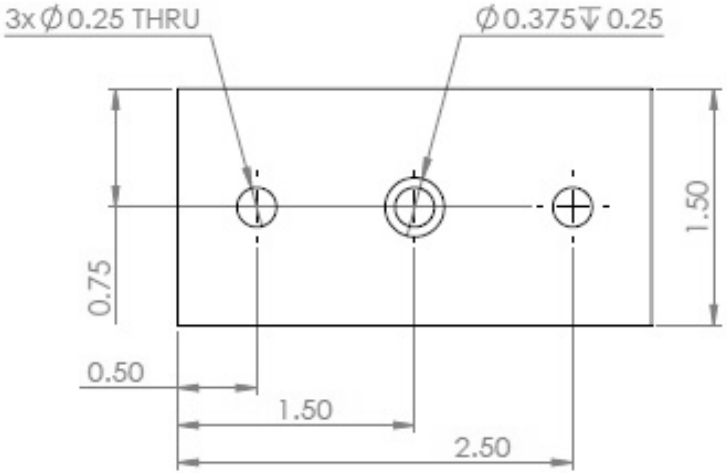

UNLESS OTHERWISE SPECIFIED:							
DIMENSIONS ARE IN ICHES TOLERANCE: FRACTIONAL: ± 1/64 ANGULAR: ± 0.2 TWO PLACE DECIMAL: ± 0.05 THREE PLACE DECIMAL: ± 0.005	MATERIAL Aluminum		NAME	DATE	SIZE	TITLE	REV
	FINISH	DRAWN	FA	02JUL13	A	Hammer adaptor	1
	DO NOT SCALE DRAWING	ENG APPR.	HL	02JUL15	SCALE 1:1		

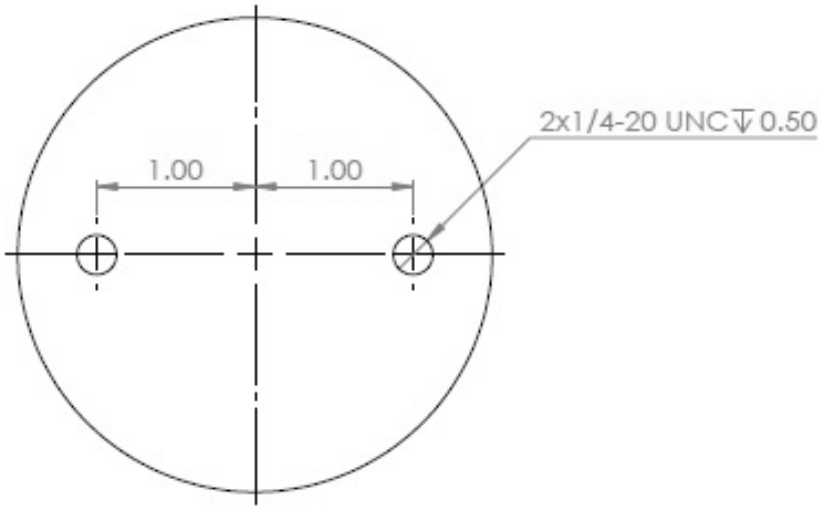

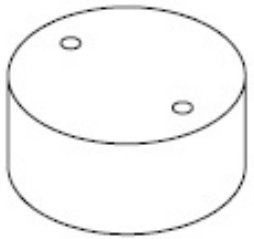

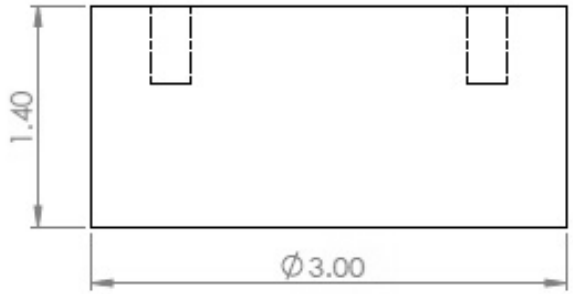

UNLESS OTHERWISE SPECIFIED:							
DIMENSIONS ARE IN ICHES TOLERANCE: FRACTIONAL: ± 1/64 ANGULAR: ± 0.2 TWO PLACE DECIMAL: ± 0.05 THREE PLACE DECIMAL: ± 0.005	MATERIAL Polyethylene		NAME	DATE	SIZE	TITLE	REV
	FINISH	DRAWN	FA	20MAR13	A	Polymeric impactor	1
	DO NOT SCALE DRAWING	ENG APPR.	HL	20MAR13	SCALE 1:1		

Part number	Description	Quantity
1	Base	1
2	Pole	2
3	Polymeric impactor	1
4	Hammer adaptor	1
5	Hammer shaft	1
6	Plate_1	1
7	Plate_2	1

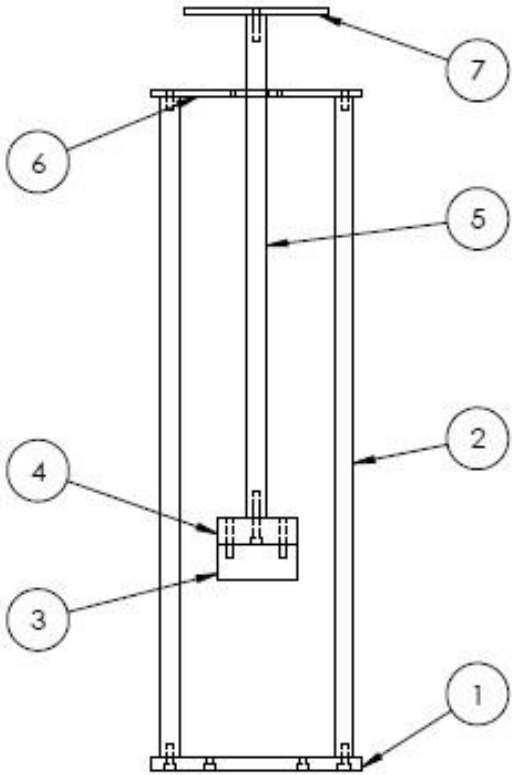

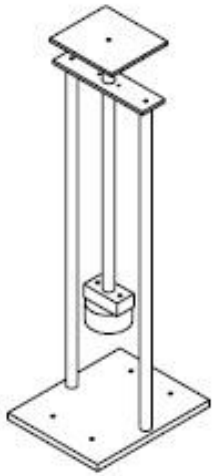

	NAME	DATE	SIZE	TITLE	REV
DRAWN	FA	02JUL13	A	Drop Tower	2
ENG APPR.	HL	02JUL13	SCALE 1:6		

Appendix D.5 - Distraction Tool Adaptor

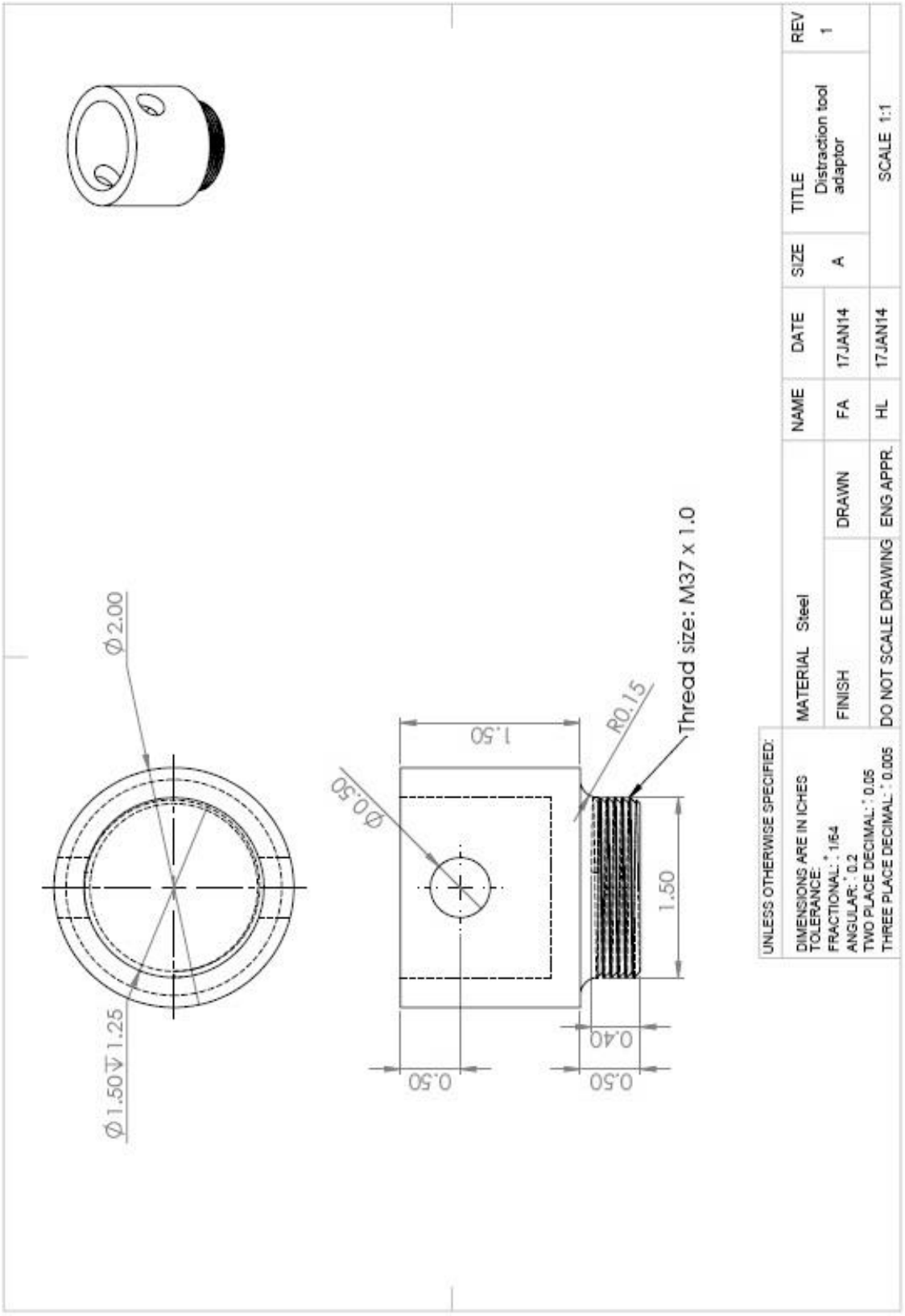

Appendix E - Test Solution pH Measurements

Table E.1: Test solution pH values during fatigue tests. N/A: not applicable (i.e., not measured).

Test number	Material	Assembly method	pH		
			Day 1	Day 3	Day 5
1	Ti6Al4V	Hand	N/A	N/A	N/A
2			7.3	7.4	7.4
3			7.3	7.3	7.4
4		Impact	7.2	7.3	7.3
5			7.3	7.2	7.4
6			7.3	7.4	7.5
7	CoCrMo	Hand	N/A	N/A	N/A
8			7.2	7.3	7.3
9			7.2	7.3	7.4
10		Impact	7.3	7.4	7.4
11			7.2	7.3	7.3
12			7.3	7.3	7.4

Table E.2: Test solution pH values during corrosion tests. N/A: not applicable (i.e., not measured).

Test number	Material	Assembly method	pH						
			Day 1	Day 3	Day 5	Day 7	Day 9	Day 11	Day 13
13	Ti6Al4V	Hand	7.3	7.3	7.3	7.5	7.6	7.8	7.9
14			7.3	7.3	7.3	7.3	7.4	7.5	7.5
15			7.2	7.2	7.3	7.3	7.3	7.4	7.6
16		Impact	7.4	7.4	7.4	7.4	7.4	7.4	7.5
17			7.3	7.4	7.4	7.6	8.1	8.6	9.1
18			7.2	7.3	7.4	7.4	7.4	7.4	7.5
19	CoCrMo	Hand	7.2	7.3	N/A	7.4	7.5	7.7	8.0
20			7.2	7.3	7.4	7.4	7.6	7.7	8.0
21			7.2	7.3	7.3	7.4	7.5	7.6	7.7
22		Impact	7.3	7.3	7.4	7.4	7.4	7.4	N/A
23			7.2	7.3	7.3	7.4	7.4	7.5	7.6
24			7.3	7.3	7.4	7.5	7.5	7.6	7.6

Appendix F - Fatigue and Corrosion Tests Summary

Table F.1: Summary of fatigue tests results. N/A: not applicable (i.e., not measured).

Test number	Material	Assembly Method	Cycles to failure	Distraction force (kN)	Pocket fluid volume (µL)
1	Ti6Al4V	Hand	1,102,837	Neck fractured	N/A
2			1,019,282	Neck fractured	N/A
3			No fracture	1.38	46.0
4		Impact	No fracture	5.46	90.8
5			No fracture	3.91	56.2
6			No fracture	5.04	< 25.0
7	CoCrMo	Hand	No fracture	1.60	N/A
8			No fracture	2.06	N/A
9			No fracture	1.11	132.0
10		Impact	No fracture	3.11	< 25.0
11			No fracture	3.93	< 25.0
12			No fracture	4.89	137.4

Table F.2: Summary of corrosion tests results. N/A: not applicable (i.e., not measured).

Test number	Material	Assembly method	Distraction force (kN)	Pocket fluid volume (µL)
13	Ti6Al4V	Hand	2.40	N/A
14			0.37	169.0
15			0.88	160.1
16		Impact	7.17	N/A
17			5.26	152.2
18			2.85	340.0
19	CoCrMo	Hand	1.34	275.2
20			1.26	289.9
21			1.91	324.3
22		Impact	2.93	N/A
23			3.64	144.8
24			3.61	273.0

Appendix G - Overall Goldberg Fretting and Corrosion Scores

Table G.1: Overall Goldberg fretting and corrosion damage scores of Ti6Al4V and CoCrMo modular necks. N/A: not applicable (i.e., not measured).

Test number	Test	Material	Assembly method	Fretting score	Corrosion score
1	Fatigue	Ti6Al4V	Hand-assembly	N/A	N/A
2				N/A	N/A
3				4	3
4			Impact-assembly	4	3
5				4	3
6				4	3
7		CoCrMo	Hand-assembly	3	2
8				3	4
9				4	4
10			Impact-assembly	2	4
11				4	4
12				2	4
13	Corrosion	Ti6Al4V	Hand-assembly	4	3
14				3	2
15				4	3
16			Impact-assembly	4	3
17				3	3
18				2	2
19		CoCrMo	Hand-assembly	3	3
20				3	4
21				3	4
22			Impact-assembly	2	3
23				2	3
24				3	3

Appendix H - Simplified Calculation of the Bending Stresses on the Hip Implant

Appendix H.1 - *In Vitro* Bending Stresses

The applied forces on the tested implants can be simplified as shown in the coordinate system diagram (Figure 5.2), which are assigned based on the literature [43], then the bending stress for each force vector is calculated, as follows:

$$\sigma = \frac{cM}{I}$$

where,

c : the perpendicular distance from the neutral axis to the farthest point from the neutral axis

M : is the bending moment, calculated as:

$$M = Fd$$

I : is the moment of inertia, calculated as:

$$I = \frac{bh^3}{12}$$

where, d is the neck length, while b and h are the base and height of the cross-sectional area of the neck-stem taper interface, respectively. For simplicity, no support of the stem pocket is considered and the stresses are calculated for the distal end of the neck that was found to be the potential crack initiation location.

Using the suggested load level of 2300 N from ISO 7206-8-1995 and ASTM 2068 Standards for endurance performance, and the implant alignment angle of $\beta = 9°$, the F_z and F_y force vectors (Figure H.1) are determined as follows:

$$F_z = 2300\ cos\ (9) = 2272\ N, \qquad F_y = 2300\ sin\ (9) = 360\ N$$

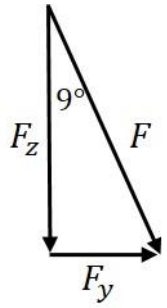

Figure H.1: Force vectors diagram based on the alignment angle of β = 9°.

By assuming a 2-D cantilever beam structure for the neck (Figure H.2) , the bending moment and moment of inertia are calculated as follows:

$$M_z = (2272)(0.055) = 125\ N.m, \qquad M_y = (360)\ (0.055) = 20\ N.m$$

$$I_z = \frac{(0.017)(0.008)^3}{12} = 7.25\ x10^{-10}\ m^4$$

$$I_y = \frac{(0.008)(0.017)^3}{12} = 3.28\ x\ 10^{-9}\ m^4$$

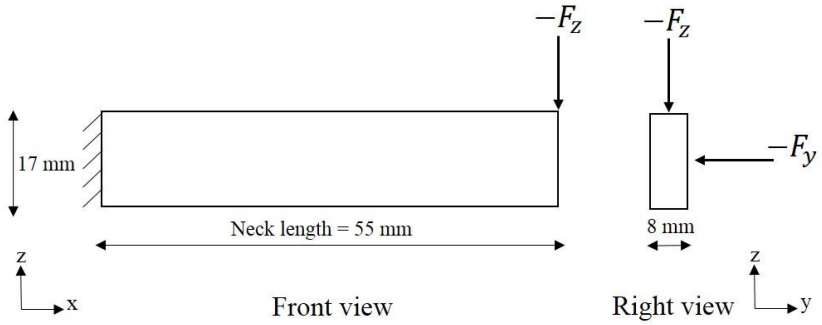

Figure H.2: A 2-D sketch of the modular neck approximated dimensions.

Finally, the bending stresses are:

$$\sigma_z = \frac{(0.004)(125\ )}{7.25\ x10^{-10}} = \ 689\ MPa, \qquad \sigma_y = \frac{(0.0085)(20)}{3.28\ x\ 10^{-9}} = 51\ MPa$$

Appendix H.2 - *In Vivo* Bending Stresses for Normal Walking Activity

Using the approximated value of the experimentally measured force vectors by Bergmann et al. [43] for a normal walking activity with a body weight of 100 kg for an average adult yields:

$$F_{Bz}\ = 2300\ N, \qquad F_{By}\ = 330\ N,$$

Appling these forces on the modular neck used in this study (Figure H.2), the *in vivo* β angle and bending stress are:

$$\beta_B = 15°$$

$$\sigma_{Bz} = 697\ MPa, \qquad \sigma_{By} = 47\ MPa$$